

DEPARTMENT OF PHYSICS, UNIVERSITY OF JYVÄSKYLÄ

**JET TRANSVERSE MOMENTUM DISTRIBUTIONS
MEASURED BY ALICE**

**BY
TOMAS SNELLMAN**

PHD thesis

Supervisors: Jan Rak, Dong Jo Kim

Jyväskylä, Finland
December, 2018

3 Contents

4	1	Introduction	7
5	1.1	Quantum chromodynamics	8
6	1.1.1	Foundation of QCD	8
7	1.1.2	Asymptotic Freedom	9
8	1.2	Heavy ion physics	13
9	1.2.1	History	13
10	1.3	Features of Heavy-Ion Collisions	15
11	1.3.1	Collision Geometry	15
12	1.3.2	Nuclear Geometry	16
13	1.3.3	Hydrodynamical Modelling	19
14	1.4	Flow	22
15	1.4.1	Anisotropic Flow	23
16	1.4.2	High p_T Phenomena	24
17	1.5	Hard processes	25
18	1.5.1	pQCD factorization	25
19	1.5.2	Jet hadronisation	27
20	1.5.3	Jet energy loss	31
21	1.5.4	Monte Carlo Implementations	40
22	1.6	QGP in Small systems	40
23	1.6.1	Collective phenomena	41
24	1.6.2	Absence of jet quenching	42
25	1.6.3	Centrality determination in small systems	43
26	2	Experimental setup and data samples	47
27	3	Experimental Details	48
28	3.1	CERN	48
29	3.2	Large Hadron Collider	50
30	3.2.1	LHC experiments	51
31	3.3	ALICE	51
32	3.3.1	Tracking	52
33	3.3.2	TPC	54
34	3.3.3	TPC upgrade	54
35	3.3.4	Particle identification	56
36	3.3.5	Electromagnetic Calorimeter	57

37	3.3.6	Forward detectors	57
38	3.3.7	Muon spectrometer	58
39	3.3.8	Trigger	59
40	4	Event and track selection	60
41	5	Analysis method	60
42	5.1	Jet Finding	60
43	5.1.1	Anti k_T algorithm	60
44	5.2	j_T	61
45	5.2.1	1 over j_T	61
46	5.3	Unfolding	62
47	5.3.1	Bayesian unfolding	63
48	5.3.2	Toy Monte Carlo	63
49	5.3.3	Pythia Response matrices	64
50	5.3.4	2D response matrices	65
51	5.3.5	Unfolding algorithm	65
52	5.3.6	Effect of number of iterations	65
53	5.3.7	Effect of different prior	66
54	5.3.8	Effect of p_T truncation	66
55	5.3.9	Unfolding closure test	66
56	5.4	Background	68
57	5.4.1	Perpendicular cone background	69
58	5.4.2	Random background	69
59	5.4.3	Auto-correlations	72
60	5.5	Fitting	72
61	6	Systematic uncertainties	73
62	7	TPC Upgrade?	75
63	8	Systematic errors	76
64	8.1	Background subtraction	76
65	8.2	Unfolding	76
66	8.3	Tracking	76
67	8.4	Combining systematics	76
68	9	Results	79
69	9.1	statistics	79
70	9.2	Data	79
71	9.3	Inclusive results	79
72	9.4	Background	80

73	9.5	Comparison between A and C side	80
74	9.6	Subtracted signal	80
75	9.7	Fitting	81
76	9.7.1	Results	81
77	9.8	Comparison to dihadron results	81
78	9.9	Different R parameters	85
79	10	Discussion	88
80	10.1	Discussion	88
81	10.1.1	Dihadron j_T	88
82	11	Summary	92

83 List of Figures

84	1	QCD phase diagram	11
85	2	η/s vs $(T - T_c)/T_c$	12
86	3	The definitions of the Reaction Plane and Participant Plane coordinate systems	15
87	4	Interaction between partons in central and peripheral collisions.	16
88	5	An illustration of the multiplicity distribution in ALICE measurement with centrality classes.	17
89	6	The results of one Glauber Monte Carlo simulation.	20
90	7	Schematic representation of a heavy-ion collision	21
91	8	Charged particle spectra	22
92	9	Illustration of flow in momentum space in central and peripheral collisions.	23
93	10	QCD Leading Order	25
94	11	Hard scattering	25
95	12	Jet showering	26
96	16	Elliptic flow, v_2 from $p_T = 1$ to 60 GeV/ c	35
97	17	Photon spectrum	36
98	18	Measurements of the nuclear modification factor R_{AA} in central heavy-ion collisions	38
99	19	A comparison between observed $R_{AA}(\Delta\phi, p_T)$ and R_{AA} using v_2	39
100	20	Calculations of the initial energy density in small collision systems at RHIC and the resulting hydrodynamic evolution.	41
101	21	Two-particle correlation results in PbPb, pPb, and pp collisions at the LHC [].	42
102	22	RpA in proton-lead collisions	43

109	23	Distribution of the sum of amplitudes in the V0A hodoscopes (Pb-going), as well as the NBD-Glauber fit (explained in the text). Centrality classes are indicated by vertical lines. The inset shows a zoom-in on the most peripheral events. [1]	45
110			
111			
112			
113	24	Top: Scatter plot of number of participating nucleons versus impact parameter; Bottom: Scatter plot of multiplicity versus the number of participating nucleons from the Glauber fit for V0A. The quantities are calculated with a Glauber Monte Carlo of p-Pb (left) and Pb-Pb (right) collisions. [1]	46
114			
115			
116			
117	25	CERN collider complex	49
118			
119	26	ALICE	52
120	27	ITS	53
121	28	TPC	55
122	29	Illustration of \vec{j}_T . The jet fragmentation transverse momentum, \vec{j}_T , is defined as the transverse momentum component of the track momentum, \vec{p}_{track} , with respect to the jet momentum, \vec{p}_{jet}	61
123			
124	30	Results from unfolding in Toy Monte Carlo	64
125			
126	31	Unfolding with different number of iterations	66
127	32	Effect of changing minimum jet p_T used in unfolding from 5 to 10 GeV	67
128			
129	33	Effect of changing minimum jet p_T used in unfolding from 5 to 10 GeV	67
130			
131	35	j_T Response matrices in single jet p_T bins	69
132	36	Pythia closure test results. Fake tracks include also tracks that do exist in the true dataset, but for one reason or another were not given j_T values. j_T is only calculated for tracks that are associated with jets	70
133			
134			
135			
136	38	j_T signal with random background subtraction fits in different jet p_T bins	76
137			
138	39	Differences between perpendicular cone and random background subtraction in the resulting RMS values.	77
139			
140	40	j_T signal with random background subtraction fits in different jet p_T bins	77
141			
142	41	Differences between Bayesian and SVD unfolding in the resulting RMS values	77
143			
144	42	Inclusive j_T with background	80
145			
146	43	j_T background with two different methods	81
147			
148	44	Comparison of inclusive j_T distributions between A and C side for minimum bias and EMCAL triggered data.	82
149	45	j_T signal with background subtracted	83

149	46	Comparison of the effect of background method on j_T signal.	83
150	47	j_T signal fits in different jet p_T bins	84
151	48	RMS values extracted from the fits for the gaussian (narrow) and inverse gamma (wide) components	84
152	49	RMS values extracted from the fits for the gaussian (narrow) and inverse gamma (wide) components	85
153	50	Jet j_T results are compared to results obtained in the dihadron analysis. This is done both in jet p_T and trigger p_T bins by converting between them.	85
154	51	Pythia R parameters j_T	86
155	52	Pythia R parameters RMS	87
156	53	Dihadron j_T results	88
157	54	RMS values of the narrow and wide j_T components in the dihadron correlation analysis. Results from pp collisions at $\sqrt{s} = 7$ TeV (circular symbols) and from p–Pb collisions at $\sqrt{s_{NN}} = 5.02$ TeV (square symbols) are compared to PYTHIA 8 tune 4C simulations at $\sqrt{s} = 7$ TeV (short dashed line) and at $\sqrt{s} = 5.02$ TeV (long dashed line). Different panels correspond to different x_{\parallel} bins with $0.2 < x_{\parallel} < 0.4$ on the left, $0.4 < x_{\parallel} < 0.6$ in the middle, and $0.6 < x_{\parallel} < 1.0$ on the right. The statistical errors are represented by bars and the systematic errors by boxes. [2]	89
158	55	Comparison of results with dihadron j_T results. Dihadron trigger p_T bins are converted to jet p_T bins using observed mean $p_{T,jet}$ values in $p_{T,trigger}$ bins. Dihadron results are for $0.2 < x_{\parallel} < 0.4$	90
159	56	PYTHIA R parameters j_T	91
160	57	Results of calculating j_T with respect to the jet axis or the leading hadron. The assumption is that because the leading hadron is an imperfect estimate of the jet axis, low j_T tracks should on average be shifted to higher j_T	91

178 1 Introduction

179 At sufficiently high energies quarks and gluons are no longer bound to hadrons,
180 but they form a deconfined state known as Quark-Gluon plasma (QGP). The
181 main goal of heavy ion physics is the study of QGP and its properties. One of the
182 experimental observables that is sensitive to the properties of QGP is the azimuthal
183 distribution of particles in the plane perpendicular to the beam direction.

184 When nuclei collide at non-zero impact parameter (non-central collisions), their
185 overlap region is asymmetric. This initial spatial asymmetry is converted via multi-
186 ple collisions into an anisotropic momentum distribution of the produced particles.
187 For low momentum particles ($p_T \lesssim 3$ GeV/c), this anisotropy is understood to
188 result from hydrodynamically driven flow of the QGP [3–7].

189 One way to characterize this anisotropy is with coefficients from a Fourier se-
190 ries parametrization of the azimuthal angle distribution of emitted hadrons. The
191 second order coefficient, v_2 which is also known as elliptic flow, shows clear depen-
192 dence on centrality. The collision geometry is mainly responsible for the elliptic
193 flow. Higher harmonics don't depend that much on centrality. These higher har-
194 monics carry information about the fluctuations in collisions. The event-by-event
195 fluctuations have an increasing importance in measurements and it has been ob-
196 served that measurements of elliptic flow in central collisions and measurements
197 of higher order harmonics are consistent with the assumption that flow in these
198 cases is mainly due to fluctuations [8].

199 At LHC energies $\sqrt{s_{NN}} = 2.76\text{GeV}$ it has been observed that in general there
200 is little difference to flow at RHIC energies. The v_2 coefficient is about 20% greater
201 at LHC than at RHIC, depending on the centrality bin. The particle identified
202 v_2 for kaons and pions follows the same trend. However it was observed that for
203 proton v_2 the quark number scaling does not work [9]. So far there is no agreement
204 of why this scaling breaks down at LHC or why it works so well at RHIC energies.

205 **1.1 Quantum chromodynamics**

206 **1.1.1 Foundation of QCD**

207 There are four known basic interactions in the universe: gravity, electromagnetic,
208 weak and strong interactions. The standard model of particle physics includes
209 three of these excluding the gravitational interaction. The theory of strong inter-
210 actions is known as Quantum Chromodynamics (QCD).

211 The development of QCD began after the introduction of new powerful particle
212 accelerators that were capable of particle physics research in the 1950s. Before this
213 particles were mainly discovered from cosmic rays. Positrons, neutrons and muons
214 were discovered in the 1930s and charged pions were discovered in 1947 []. The
215 neutral pion was discovered in 1950 [10].

216 The Lawrence Berkeley National Laboratory started the Bevalac accelerator in
217 1954, Super Proton Synchrotron (SPS) in CERN began operating in 1959 and the
218 Alternating Gradient Synchrotron at Brookhaven started in 1960. With an energy
219 of 33GeV AGS was the most powerful accelerator of that time. By the beginning
220 of 1960s several new particles had been discovered. These include antiprotons,
221 antineutrons, Δ -particles and the six hyperons (Ξ^0 , Ξ^- , Σ^\pm , Σ^0 and Λ).

222 Facing this number of different particles started the search for symmetries. Al-
223 ready in 1932 Heisenberg [11] had proposed an isospin model to explain similarities
224 between the proton and the neutron. In 1962 Gell-Mann and Ne'eman presented
225 that particles sharing the same quantum numbers (spin, parity) could be organ-
226 ised using the symmetry of SU(3). [12] Heisenberg's Isospin model followed the
227 symmetry of SU(2). Using the SU(3) model known baryons and mesons could be
228 presented as octets. This also lead to the discovery of the Ω^- particle since this
229 was missing from the SU(3) decoupler that included heavier baryons.

230 The most simple representation of SU(3) was a triplet. Inside this triplet
231 particles would have electric charges $2/3$ or $-1/3$. These had not been however
232 detected. In 1964 Gell-Mann [13] and Zweig proposed that baryons and mesons
233 would bound states of these three hypothetical triplet particles that Gell-Mann
234 called quarks. Now we know that these are the u , d and s quarks. This original
235 quark model was violating the Pauli exclusion principle. For example the Ω^-
236 particle is comprised of three s quarks which would have exactly the same quantum
237 states.

238 The first one to present the idea of colour was Greenberg already in 1964 [14].
239 In 1971 Gell-Mann and Frtizsch presented their model, which solved the antisym-
240 metry problem. They added a colour quantum number to quarks, which separated
241 quarks of the same species. In the new colour model the baryonic wave function
242 became

$$(qqq) \rightarrow (q_r q_g q_b - q_g q_r q_b + q_b q_r q_g - q_r q_b q_g + q_g q_b q_r - q_b q_g q_r), \quad (1)$$

243 The colour model was also supported by experimental evidence. The decay
244 rate of a neutral pion with the addition of colours is

$$\Lambda(\pi^0 \rightarrow \gamma\gamma) = \frac{\alpha^2}{2\pi} \frac{N_c^2}{3^2} \frac{m_\pi^3}{f_\pi^2}. \quad (2)$$

245 For $N_c = 3$ this gives 7.75eV and the measured value is (7.86 ± 0.54) eV [15].

246 Another observable that combines the colour information also to the number
247 of quark flavours is The Drell-Ratio R [16]

$$R = \frac{\sigma(e^+ + e^- \rightarrow \text{hadrons})}{\sigma(e^+ + e^- \rightarrow \mu^+ + \mu^-)} = N_c \sum_f Q_f^2. \quad (3)$$

248 This ratio has the numerical value 2 when including the three light quarks u , d
249 and s . When the collision energy reaches the threshold of heavy quark (c and
250 b) production processes this increases to $^{10}/3$ (for $f = u, d, s, c$) and $^{11}/3$ (for $f =$
251 u, d, s, c, b). The threshold of $t\bar{t}$ production, $\sqrt{s} \approx 350$ GeV has not been reached
252 so far by any e^+e^- colliders.

253 The colour model explained why no free quarks had been observed. Only colour
254 neutral states are possible. The simplest ways of producing a colour neutral object
255 are the combination of three quarks, and the combination of a quark-antiquark
256 pair. These are known as baryons and mesons.

257 After the addition of colour the main ingredients of QCD had been established.
258 The final quantum field theory of Quantum Chromodynamics formed quickly be-
259 tween 1972 and 1974. Main part of this was the work Gross, Wilczek, Politzer
260 and George did for non-abelian gauge field theories [17–21]. Gross, Wilczek and
261 Politzer received the Nobel Prize in Physics for their work. The role of gluons was
262 as a colour octet was presented by Fritzsch, Gell-Mann and Leutwyler in 1973 [22].
263 The theory had now 8 massless gluons to mediate the strong interaction.

264 However, these gluons had not been discovered. Indirect evidence of the ex-
265 istence had been seen as it was observed that only about half of the momentum
266 of protons was transported by the quarks [23]. Direct evidence should be seen in
267 electron-electron collisions as a third, gluonic, jet in addition to two quark jets.
268 Three jet events were first seen in 1979 at the PETRA accelerator at DESY [24–26].

269 1.1.2 Asymptotic Freedom

270 In Quantum Electrodynamics (QED) The electric charge is screened. In the
271 vicinity of a charge, the vacuum becomes polarized. Virtual charged particle-
272 antiparticle pairs around the charge are arranged so that opposing charges face

each other. Since the pairs also include an equal amount opposite charge compared to the original charge the average charge seen by an observer at a distance is smaller. When the distance to the charge increases the effective charge decreases until the coupling constant of QED reaches the fine-structure constant $\alpha = \frac{1}{137}$.

Contrary to QED QCD is a non-abelian theory. In other words the generators of the symmetry group of QCD, SU(3), do not commute. This has the practical consequence that gluons interact also with other gluons, whereas in QED the neutral carrier particles, photons, only interact with charged particles. There is screening also in QCD because of the colour charges, but in addition to that there is antiscreening because of the gluon interactions. In QCD the antiscreening effect is stronger than screening. For larger distances to the colour charge the coupling constant is larger. This explains why no free colour charges can be observed. When the distance between charges increases the interaction strengthens until it is strong enough to produce a new quark-antiquark pair.

On the other hand, at very small distances the coupling constant approaches 0. This is called asymptotic freedom. For large energies and small distances the coupling constant is negligible. In 1975 Collins [27] predicted a state where individual quarks and gluons are no longer confined into bound hadronic states. Instead they form a bulk QCD matter that Edward Shuryak called Quark-Gluon plasma in his 1980 review of QCD and the theory of superdense matter [28]. QGP can be seen as a separate state of matter. A schematic view of a phase diagram for QCD matter is shown in Fig. 1.

In the early universe at the age of 10^{-6} s after the Big Bang the conditions preferred the existence of QGP instead of hadronic matter. Nowadays bulk QCD matter, its properties and its phase transitions between hadronic matter and the quark-gluon plasma (QGP) can be explored in the laboratory, through collisions of heavy atomic nuclei at ultra-relativistic energies. The study of QCD matter at high temperature is of fundamental and broad interest. The phase transition in QCD is the only phase transition in a quantum field theory that can be probed by any present or foreseeable technology.

One important property of the QGP is the shear viscosity to entropy ratio, η/s . It is believed that this ratio has an universal minimum value of $1/4\pi \approx 0.8$, which holds for all substances. This limit would be reached in the strong coupling limit of certain gauge theories [30]. The temperature dependance of the ratio is shown in Fig. 2. The minimum value of η/s is found in the vicinity of the critical temperature, T_c [31]. Finding the η/s values in QGP matter would therefore also provide a way of determining the critical point of QCD matter.

The η/s value for the matter created in Au-Au collisions at RHIC ($\sqrt{s_{NN}}$) has been estimated to be 0.09 ± 0.015 [31], which is very close to the lowest value for a wide class of thermal quantum field theories [30] for all relativistic quantum field

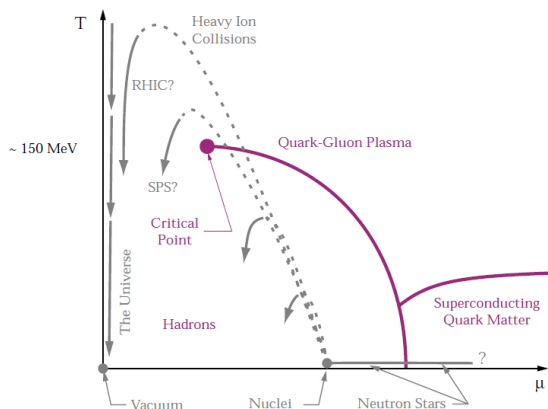


Figure 1: A schematic outline for the phase diagram of QCD matter at ultra-high density and temperature. The quark chemical potential μ that is on the x-axis represents the imbalance between quarks and antiquarks. At zero temperature this corresponds to the number of quarks but at higher temperatures there are also additional pairs of quarks and antiquarks. Along the horizontal axis the temperature is zero, and the density is zero up to the onset transition where it jumps to nuclear density, and then rises with increasing μ . Neutron stars are in this region of the phase diagram, although it is not known whether their cores are dense enough to reach the quark matter phase. Along the vertical axis the temperature rises, taking us through the crossover from a hadronic gas to the quark-gluon plasma. This is the regime explored by high-energy heavy-ion colliders. [29]

313 theories at finite temperature and zero chemical potential. This suggests that the
 314 the matter created goes through a phase where it is close to the critical point of
 315 QCD.

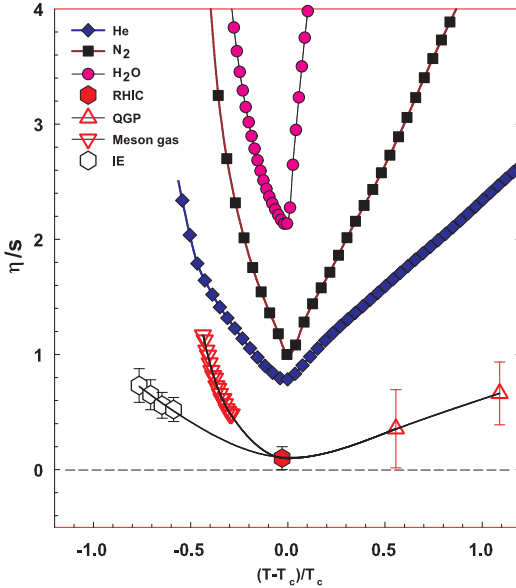


Figure 2: η/s as a function of $(T - T_c)/T_c$ for several substances as indicated. The calculated values for the meson-gas have an associated error of $\sim 50\%$. The lattice QCD value $T_c = 170$ MeV is assumed for nuclear matter. The lines are drawn to guide the eye. [31]

316 1.2 Heavy ion physics

317 The Quark Gluon Plasma (QGP) is experimentally accessible by colliding heavy
318 ions at high energies. Nowadays research of Heavy-Collisions is mainly performed
319 at two particle colliders; the The Relativistic Heavy Ion Collider (RHIC) at BNL
320 in New York, USA and he Large Hadron Collider (LHC) at CERN in Switzer-
321 land. Energy densities at these colliders should be enough to produce QGP and
322 convincing evidence of the creation has been seen at both colliders.

323 The development of heavy ion physics is strongly connected to the development
324 of particle colliders. Experimental study of relativistic heavy ion collisions has been
325 carried out for three decades, beginning with the Bevalac at Lawrence Berkeley
326 National Laboratory (LBNL) [32], and continuing with the AGS at Brookhaven
327 National Laboratory (BNL) [33], CERN SPS [34], RHIC at BNL and LHC at
328 CERN. The first colliders could not produce enough energy to create QGP matter
329 so they could only probe the hadronic state.

330 The collective motion of matter in a heavy-ion collision has been modeled using
331 several models e.g. the Blast wave Model [35] has been used successfully. Another
332 model growing in popularity is the hydrodynamical approach which is further
333 discussed in section 1.3.3.

334 1.2.1 History

335 The first heavy-ion collisions were done at the Bevalac experiment at the Lawrence
336 Berkeley National Laboratory [32] and at the Joint Institute for Nuclear Research
337 in Dubna [36] at energies up to 1GeV per nucleon. In 1986 the Super Proton
338 Synchrotron (SPS) at CERN started to look for QGP signatures in O+Pb col-
339 lisions. The center-of-mass energy per colliding nucleon pair ($\sqrt{s_{NN}}$) was 19.4
340 GeV [34]. These experiments did not find any decisive evidence of the existence
341 of QGP. In 1994 a heavier lead (Pb) beam was introduced for new experiments
342 at $\sqrt{s_{NN}} \approx 17$ GeV. At the same time the Alternating Gradient Synchrotron
343 (AGS) at BNL, Brookhaven collided ions up to ^{32}S with a fixed target at energies
344 up to 28GeV [33]. Although the discovery of a new state of matter was reported
345 at CERN, these experiments provided no conclusive evidence of QGP. Now SPS
346 is used with 400 GeV proton beams for fixed-target experiments, such as the SPS
347 Heavy Ion and Neutrino Experiment (SHINE) [37], which tries to search for the
348 critical point of strongly interacting matter.

349 The Relativistic Heavy Ion Collider (RHIC) at BNL in New York, USA started
350 its operation in 2000. The top center-of-mass energy per nucleon pair at RHIC, 200
351 GeV, was reached in the following years. The results from the experiments at RHIC
352 have provided a lot of convincing evidences that QGP was created [3,4,38,39]. The
353 newest addition to the group of accelerators capable of heavy-ion physics is the

³⁵⁴ Large Hadron Collider (LHC) at CERN, Switzerland. LHC started operating in
³⁵⁵ November 2009 with proton-proton collisions. First Pb-Pb heavy ion runs started
³⁵⁶ in November 2010 with $\sqrt{s_{NN}} = 2.76$ TeV, over ten times higher than at RHIC.
³⁵⁷ Among the six experiments at LHC, the Large Ion Collider Experiment (ALICE)
³⁵⁸ is dedicated to heavy ion physics. Also CMS and ATLAS have active heavy ion
³⁵⁹ programs.

360 **1.3 Features of Heavy-Ion Collisions**

361 **1.3.1 Collision Geometry**

362 In contrast to protons atomic nuclei are objects with considerable transverse size.
363 The properties of a heavy-ion collision depend strongly on the impact parameter
364 b which is the vector connecting the centers of the two colliding nuclei at their
365 closest approach. One illustration of a heavy-ion collision is shown in Fig. 3.

366 Impact parameter defines the reaction plane which is the plane spanned by b
367 and the beam direction. Ψ_{RP} gives the angle between the reaction plane and some
368 reference frame angle. Experimentally the reference frame is fixed by the detector
369 setup. Reaction plane angle cannot be directly measured in high energy nuclear
 collisions, but it can be estimated with the event plane method [40].

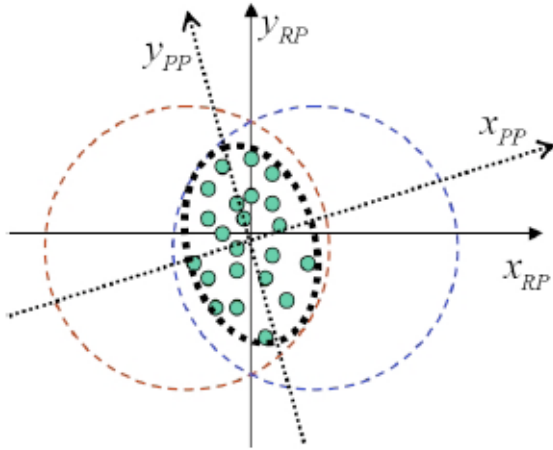


Figure 3: The definitions of the Reaction Plane and Participant Plane coordinate systems [41]. The dashed circles represent the two colliding nuclei and the green dots are partons that take part in the collision. x_{PP} and x_{RP} are the participant and reaction planes. The angle between x_{RP} and x_{PP} is given by Eq. (4). y_{PP} and y_{RP} are lines perpendicular to the participant and reaction planes.

370
371 Participant zone is the area containing the participants. The distribution of
372 nucleons in the nucleus exhibits time-dependent fluctuations. Because the nucleon
373 distribution at the time of the collision defines the participant zone, the axis of
374 the participant zone fluctuates and can deviate from the reaction plane. The angle
375 between the participant plane and the reaction plane is defined by [42]

$$\psi_{PP} = \arctan \frac{-2\sigma_{xy}}{\sigma_y^2 - \sigma_x^2 + \sqrt{(\sigma_y^2 - \sigma_x^2)^2 + 4\sigma_{xy}^2}}, \quad (4)$$

376 where the σ -terms are averaged over the energy density.

$$\sigma_y^2 = \langle y^2 \rangle - \langle y \rangle^2, \sigma_x^2 = \langle x^2 \rangle - \langle x \rangle^2, \sigma_{xy} = \langle xy \rangle - \langle x \rangle \langle y \rangle \quad (5)$$

377 The impact parameter is one way to quantize the centrality of a heavy-ion
 378 collision but it is impossible to measure in a collision. It can be estimated from
 379 observed data using theoretical models, but this is always model-dependent and
 380 to compare results from different experiments one needs an universal definition for
 381 centrality. The difference between central and peripheral collisions is illustrated
 382 in Fig. 4. In a central collision the overlap region is larger than in a peripheral
 383 collision. Larger overlap region translates into a larger number of nucleons partici-
 384 pating in the collision, which in turn leads to a larger number of particles produced
 385 in the event.

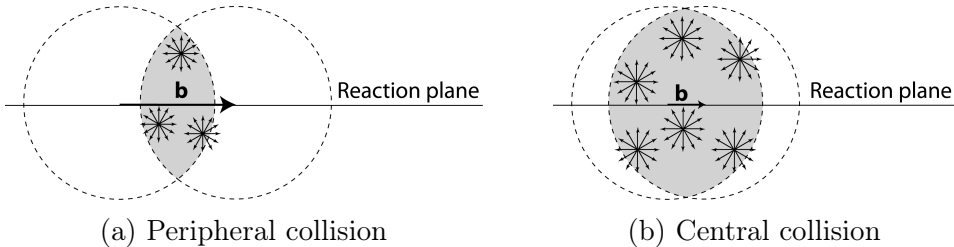


Figure 4: Interaction between partons in central and peripheral collisions. The snowflakes represent elementary parton-parton collisions. When the impact parameter b is large the number of elementary collisions is small. Particle production is small. Smaller impact parameter increases the number of elementary collisions. This increases particle production.

386 Usually centrality is defined by dividing collision events into percentile bins by
 387 the number participants or experimentally by the observed multiplicity. Centrality
 388 bin 0-5% corresponds to the most central collisions with the highest multiplicity
 389 and higher centrality percentages correspond to more peripheral collisions with
 390 lower multiplicities. A multiplicity distribution from ALICE measurements [43]
 391 illustrating the centrality division is shown in Fig. 5. The distribution is fitted
 392 using a phenomenological approach based on a Glauber Monte Carlo [44] plus a
 393 convolution of a model for the particle production and a negative binomial distri-
 394 bution.

395 1.3.2 Nuclear Geometry

396 To model heavy-ion collisions one must first have a description as good as possible
 397 of the colliding objects. Atomic nuclei are complex ensembles of nucleons. The
 398 nuclei used in heavy-ion physics have in the order of 200 nucleons. Mostly used

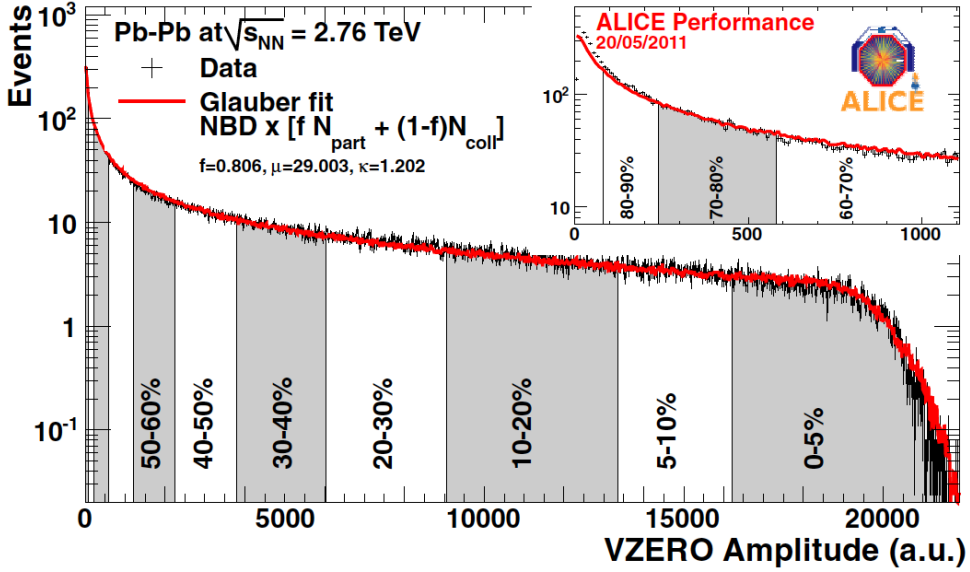


Figure 5: An illustration of the multiplicity distribution in ALICE measurements. The red line shows the fit of the Glauber calculation to the measurement. The data is divided into centrality bins [43]. The size of the bins corresponds to the indicated percentile.

³⁹⁹ nuclei are ²⁰⁸Pb at LHC and ¹⁹⁷Au at RHIC. The distribution of these nucleons
⁴⁰⁰ within a nucleus is not uniform and is subject to fluctuations in time.

⁴⁰¹ Nuclear geometry in heavy-ion collisions is often modelled with the Glauber
⁴⁰² Model. The model was originally developed to address the problem of high energy
⁴⁰³ scattering with composite particles. Glauber presented his first collection of papers
⁴⁰⁴ and unpublished work in his 1958 lectures [45]. In the 1970's Glauber's work
⁴⁰⁵ started to have utility in describing total cross sections. Maximon and Czyz applied
⁴⁰⁶ it to proton-nucleus and nucleus-nucleus collisions in 1969 [46].

⁴⁰⁷ In 1976 [47] Białas, Bleszyński, and Czyz applied Glauber's approach to
⁴⁰⁸ inelastic nuclear collisions. Their approach introduced the basic functions used in
⁴⁰⁹ modern language including the thickness function and the nuclear overlap function.
⁴¹⁰ Thickness function is the integral of the nuclear density over a line going through
⁴¹¹ the nucleus with minimum distance s from its center

$$T_A(s) = \int_{-\infty}^{\infty} dz \rho(\sqrt{s^2 + z^2}). \quad (6)$$

⁴¹² This function gives the thickness of the nucleus, i.e. the amount material seen by
⁴¹³ a particle passing through it.

⁴¹⁴ Overlap function is an integral of the thickness functions of two colliding nuclei
⁴¹⁵ over the overlap area. This can be seen as the material that takes part in the
⁴¹⁶ collision. It is given as a function of the impact parameter b

$$T_{AB}(b) = \int ds^2 T_A(\bar{s}) T_B(\bar{s} - \bar{b}) \quad (7)$$

⁴¹⁷ The average overlap function, $\langle T_{AA} \rangle$, in an A-A collisions is given by [48]

$$\langle T_{AA} \rangle = \frac{\int T_{AA}(b) db}{\int (1 - e^{-\sigma_{pp}^{inel} T_{AA}(b)}) db}. \quad (8)$$

⁴¹⁸ Using $\langle T_{AA} \rangle$ one can calculate the mean number of binary collisions

$$\langle N_{coll} \rangle = \sigma_{pp}^{inel} \langle T_{AA} \rangle, \quad (9)$$

⁴¹⁹ where the total inelastic cross-section, σ_{pp}^{inel} , gives the probability of two nucleons
⁴²⁰ interacting. The number of binary collisions is related to the hard processes in a
⁴²¹ heavy-ion collision. Each binary collision has equal probability for direct produc-
⁴²² tion of high-momentum partons. Thus the number of high momentum particles is
⁴²³ proportional to $\langle N_{coll} \rangle$.

⁴²⁴ Soft production on the other hand is related to the number of participants.
⁴²⁵ It is assumed that in the binary interactions participants get excited and further
⁴²⁶ interactions are not affected by previous interactions because the time scales are
⁴²⁷ too short for any reaction to happen in the nucleons. After the interactions ex-
⁴²⁸ cited nucleons are transformed into soft particle production. Production does not
⁴²⁹ depend on the number of interactions a nucleon has gone through. The average
⁴³⁰ number of participants, $\langle N_{part} \rangle$ can also be calculated from the Glauber model

$$\begin{aligned} \langle N_{part}^{AB}(b) \rangle &= \int ds^2 T_A(\bar{s}) \left[1 - \left[1 - \sigma_{NN} \frac{T_B(\bar{s} - \bar{b})}{B} \right]^B \right] \\ &+ \int ds^2 T_B(\bar{s}) \left[1 - \left[1 - \sigma_{NN} \frac{T_A(\bar{s} - \bar{b})}{A} \right]^A \right]. \end{aligned} \quad (10)$$

⁴³¹ Glauber calculations require some knowledge of the properties of the nuclei.
⁴³² One requirement is the nucleon density distribution, which can be experimen-
⁴³³ tally determined by studying the nuclear charge distribution in low-energy elec-
⁴³⁴ tron scattering experiments [44]. The nucleon density is usually parametrized by
⁴³⁵ a Woods-Saxon distribution

$$\rho(r) = \frac{\rho_0}{1 + \exp\left(\frac{r-R}{a}\right)}, \quad (11)$$

where ρ_0 is the nucleon density in center of the nucleus, R is the nuclear radius and a parametrizes the depth of the skin. The density stays relatively constant as a function of r until around R where it drops to almost 0 within a distance given by a .

Another observable required in the calculations is the total inelastic nucleon-nucleon cross-section $\sigma_{\text{inel}}^{\text{NN}}$. This can be measured in proton-proton collisions at different energies.

There are two often used approaches to Glauber calculations. The optical approximation is one way to get simple analytical expressions for the nucleus-nucleus interaction cross-section, the number of interacting nucleons and the number of nucleon-nucleon collisions. In the optical Glauber it is assumed that during the crossing of the nuclei the nucleons move independently and they will be essentially undeflected.

With the increase of computational power at hand the Glauber Monte Carlo (GMC) approach has emerged as a method to get a more realistic description of the collisions. In GMC the nucleons are distributed randomly in three-dimensional coordinate system according to the nuclear density distributions. Also nuclear parameters, like the radius R can be sampled from a distribution. A heavy-ion collision is then treated as a series of independent nucleon-nucleon collisions, where in the simplest model nucleons interact if their distance in the plane orthogonal to the beam axis, d , satisfies

$$d < \sqrt{\sigma_{\text{inel}}^{\text{NN}}} \quad (12)$$

The average number of participants and binary collisions can then be determined by simulating many nucleus-nucleus collisions. The results of one GMC Pb-Pb event with impact parameter $b = 9.8\text{fm}$ is shown in Fig. 6

1.3.3 Hydrodynamical Modelling

The relativistic version of hydrodynamics has been used to model the deconfined phase of a heavy-ion collision with success. Heavy-ion collisions produce many hadrons going into all directions. It is expected that tools from statistical physics would be applicable to this complexity [49]. The power of relativistic hydrodynamics lies in its simplicity and generality. Hydrodynamics only requires that there is local thermal equilibrium in the system. In order to reach thermal equilibrium the system must be strongly coupled so that the mean free path is shorter than the length scales of interest [50].

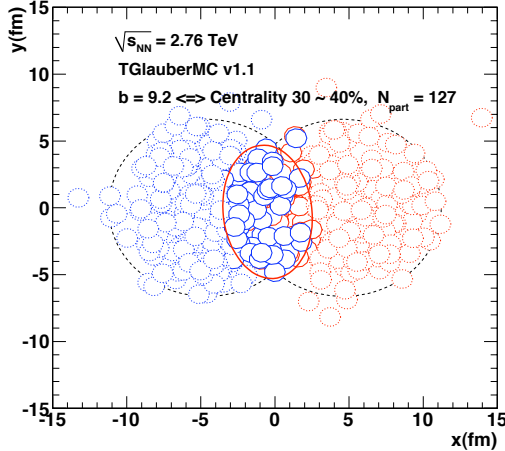


Figure 6: The results of one Glauber Monte Carlo simulation. Big circles with black dotted boundaries represent the two colliding nuclei. The participant zone is highlighted with the solid red line. Small red and blue circles represent nucleons. Circles with thick boundaries are participants i.e. they interact with at least one nucleon from the other nucleus. Small circles with dotted boundaries are spectators which do not take part in the collision.

469 The use of relativistic hydrodynamics in high-energy physics dates back to
 470 Landau [51] and the 1950's, before QCD was discovered. Back then it was used
 471 in proton-proton collisions. Development of hydrodynamics for the use of heavy-
 472 ion physics has been active since the 1980's, including Bjorken's study of boost-
 473 invariant longitudinal expansion and infinite transverse flow [?]. Major steps were
 474 taken later with the inclusion of finite size and and dynamically generated trans-
 475 verse size [?, ?], a part of which was done at the University of Jyväskylä. The role
 476 of hydrodynamics in heavy-ion physics was strengthened when QGP was observed
 477 to behave like a liquid by RHIC [3].

478 The evolution of a heavy-ion event can be divided into four stages. A schematic
 479 representation of the evolution of the collisions is shown in Fig. 7. Stage 1 follows
 480 immediately the collision. This is known as the pre-equilibrium stage. Hydrody-
 481 namic description is not applicable to this regime because thermal equilibrium is
 482 not yet reached. The length of this stage is not known but it is assumed to last
 483 about 1 fm/c in proper time τ .

484 The second stage is the regime where thermal equilibrium or at least near-
 485 equilibrium is reached. In this stage hydrodynamics should be applicable if the
 486 temperature is above the deconfinement temperature [50]. This lasts about 5 –
 487 10 fm/c until the temperature of the system sinks low enough for hadronization to

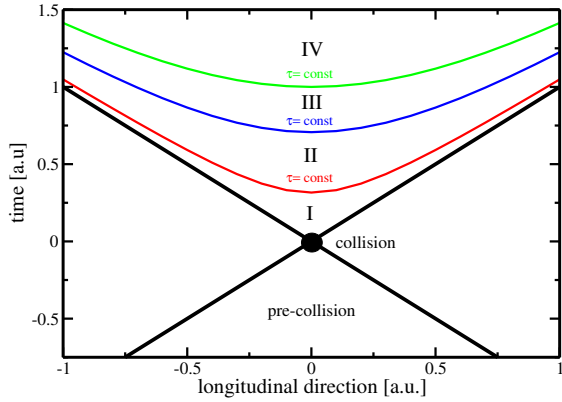


Figure 7: Schematic representation [50] of a heavy-ion collision as the function of time and longitudinal coordinates z . The various stages of the evolution correspond to proper time $\tau = \sqrt{t^2 - z^2}$ which is shown as hyperbolic curves separating the different stages.

488 occur. Now the system loses its deconfined, strongly coupled, state and hydrodynamics
 489 can no longer be used. The third stage is the hadron gas stage where the
 490 hadrons still interact. This ends when hadron scattering becomes rare and they
 491 no longer interact. In the final stage hadrons are free streaming and they fly in
 492 straight lines until they reach the detector.

493 The hydrodynamical approach treats the ensemble of particles as a fluid. It
 494 uses basic equations from hydrodynamics and thermodynamics but with a few
 495 modifications to account for the relativistic energies. The calculation is based
 496 on a collection of differential equations connecting the local thermal variables like
 497 temperature, pressure etc. to local velocities of the fluid. One also needs equations
 498 of state that connect the properties of the matter, e.g. temperature and pressure
 499 to density. Given initial conditions and equations of state the calculation gives the
 500 time-evolution of the system.

501 At first only ideal hydrodynamics was used. Ideal hydrodynamics does not
 502 include viscosity but it is a relatively good approximation and it could predict
 503 phenomena like elliptic flow. For more detailed calculations also viscosity must be
 504 considered and viscosity itself is an interesting property of QGP.

505 In this thesis I compare my results of identified particle flow to calculations from
 506 two hydrodynamical models; VISHNU model by Song *et al.* [52] and calculations
 507 by Niemi *et al.* [53].

508 1.4 Flow

509 In a heavy-ion collision the bulk particle production is known as flow. The pro-
 510 duction is mainly isotropic but a lot of studies including my thesis focus on the
 511 small anisotropies. After the formation of the QGP, the matter begins to expand
 512 as it is driven outwards by the strong pressure difference between the center of the
 513 collision zone and the vacuum outside the collision volume. The pressure-driven
 514 expansion is transformed into flow of low-momentum particles in the hadroniza-
 515 tion phase. Since the expansion is mainly isotropic the resulting particle flow is
 516 isotropic with small anisotropic corrections that are of the order of 10% at most.
 517 The isotropic part of flow is referred to as radial flow.

518 The transverse momentum spectra dN/dp_T in heavy-ion collisions is shown

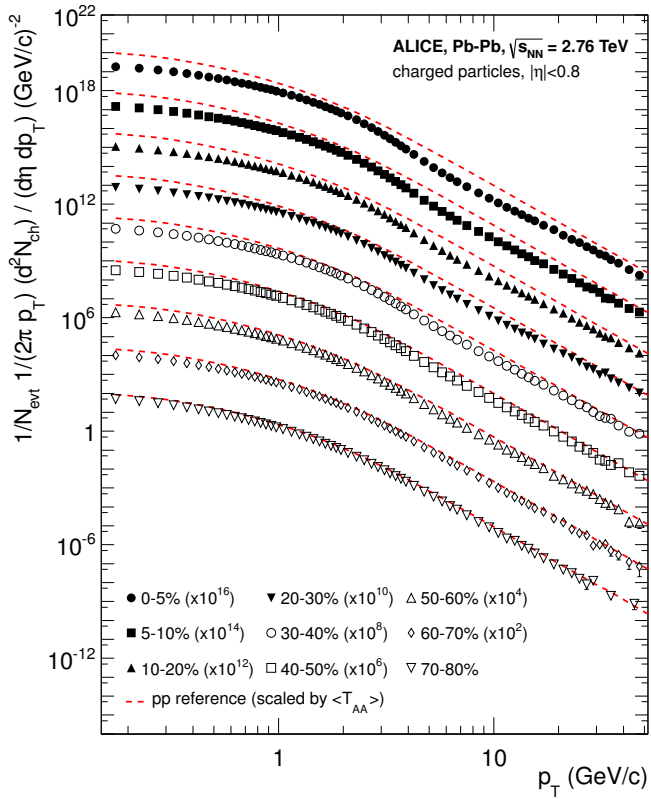


Figure 8: Charged particle spectra measured by ALICE [54] for the 9 centrality classes given in the legend. The distributions are offset by arbitrary factors given in the legend for clarity. The distributions are offset by arbitrary factors given in the legend for clarity. The dashed lines show the proton-proton reference spectra scaled by the nuclear overlap function determined for each centrality class and by the Pb-Pb spectra scaling factors [54].

519 in Fig. 8. The vast majority of produced particles have small p_T . The difference
 520 between the yield of 1 GeV/c and 4 GeV/c particles is already 2-3 orders of mag-
 521 nitude. Any observables that are integrated over p_T are therefore dominated by
 522 the small momentum particles.

523 1.4.1 Anisotropic Flow

524 In a non-central heavy-ion collision the shape of the impact zone is almond-like.
 525 In peripheral collisions the impact parameter is large which means a strongly
 526 asymmetric overlap region. In a central collision the overlap region is almost
 527 symmetric in the transverse plane. In this case the impact parameter is small.
 528 Collisions with different impact parameters are shown in Fig. 4.

529 The pressure gradient is largest in-plane, in the direction of the impact pa-
 530 rameter b , where the distance from high pressure, at the collision center, to low
 531 pressure, outside the overlap zone, is smallest. This leads to stronger collective
 532 flow into in-plane direction, which in turn results in enhanced thermal emission
 533 through a larger effective temperature into this direction, as compared to out-of-
 534 plane [5, 6, 55]. The resulting flow is illustrated in Fig. 9. Flow with two maxima
 535 in the direction of the reaction plane is called elliptic flow. This is the dominant

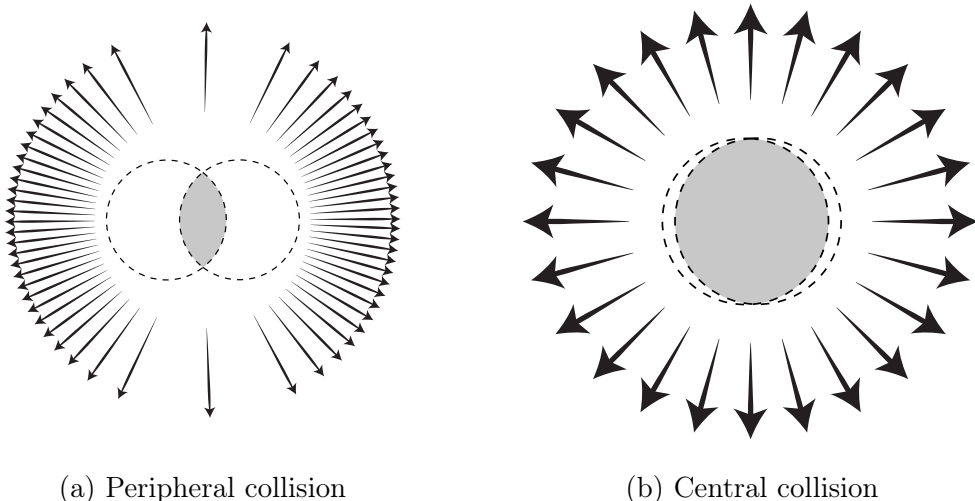


Figure 9: Illustration of flow in momentum space in central and peripheral collisions. The density of the arrows represent the magnitude of flow seen at a large distance from the collision in the corresponding azimuthal direction. In a peripheral collision momentum flow into in-plane direction is strong and flow into out-of-plane direction is weak. In a central collision anisotropy in flow is smaller, but the total yield of particles is larger.

part of anisotropic flow. Also more complex flow patterns can be identified. The most notable of these is the triangular flow, which is mainly due to fluctuations in the initial conditions.

Flow is nowadays usually quantified in the form of a Fourier composition

$$E \frac{d^3N}{dp^3} = \frac{1}{2\pi p_T} \frac{d^2N}{dp_T d\eta} \left(1 + \sum_{n=1}^{\infty} 2v_n(p_T, \eta) \cos(n(\phi - \Psi_n)) \right), \quad (13)$$

where the coefficients v_n give the relative strengths of different anisotropic flow components and the overall normalisation gives the strength of radial flow. Elliptic flow is represented by v_2 and v_3 represents triangular flow. The first coefficient, v_1 , is connected to directed flow. This will however in total be zero because of momentum conservation. It can be nonzero in some rapidity or momentum regions but it must be canceled by other regions.

The first approaches to quantifying the anisotropy of flow did not use the Fourier composition. Instead they approached the problem with a classic event shape analysis using directivity [56] or sphericity [5, 57] to quantify the flow.

The first experimental studies of anisotropy were performed at the AGS [58] in 1993. They noted that the anisotropy of particle production in one region correlates with the reaction plane angle defined in another region.

The first ones to present the Fourier decomposition were Voloshin and Zhang in 1996 [59]. This new approach was useful for detecting different types of anisotropy in flow, since the different Fourier coefficients give different harmonics in flow. They also show the relative magnitude of each harmonic compared to radial flow.

Some parts of the Fourier composition approach were used for Au-Au collisions at $\sqrt{s_{NN}} = 11.4\text{GeV}$ at AGS in 1994 [60]. This analysis still focused on event shapes but they constructed these shapes using Fourier composition from different rapidity windows.

1.4.2 High p_T Phenomena

The measurement of anisotropic flow coefficients can be extended to very high transverse momenta p_T . High p_T measurements of v_2 from CMS [61] are shown in Fig. 16. For high transverse momenta v_2 values are positive and they decrease slowly as a function of p_T . At high transverse momentum the v_2 values don't, however, represent flow.

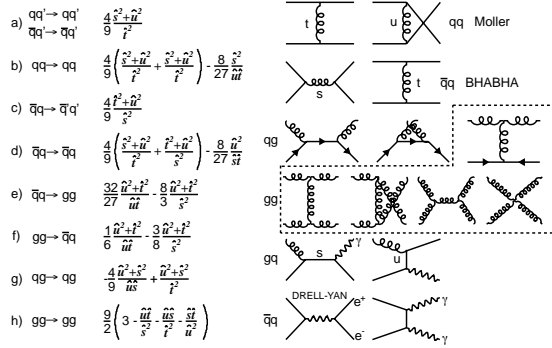


Figure 10: The basic pQCD processes and their quadratic matrix elements

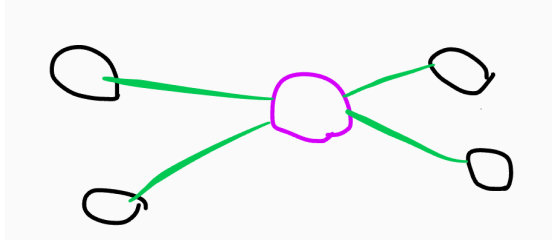


Figure 11: Schematic view of hard scattering process of $p + p \rightarrow 2 \text{jets}$

566 1.5 Hard processes

567 1.5.1 pQCD factorization

The term Hard Scattering is used in connection with the scattering of two point-like constituents (partons) of colliding nucleons, when the momentum transfer Q^2 is large ($Q \gg \Lambda_{\text{QCD}}$). Figure ?? shows the incoming partons, quarks or gluons, as they exchange a space-like virtual gluon and produce two highly virtual outgoing partons. The outgoing partons will eventually fragment into collimated showers of partons, referred to as jets

Jet fragmentation can be factorised into three components; the parton distribution functions f_a , f_b that give the probability of getting a parton with momentum fraction x of the proton, the cross section of the elementary scattering $ab \rightarrow cd$ (Fig. 10) and the fragmentation functions that give the probability of getting hadron h from the parton.

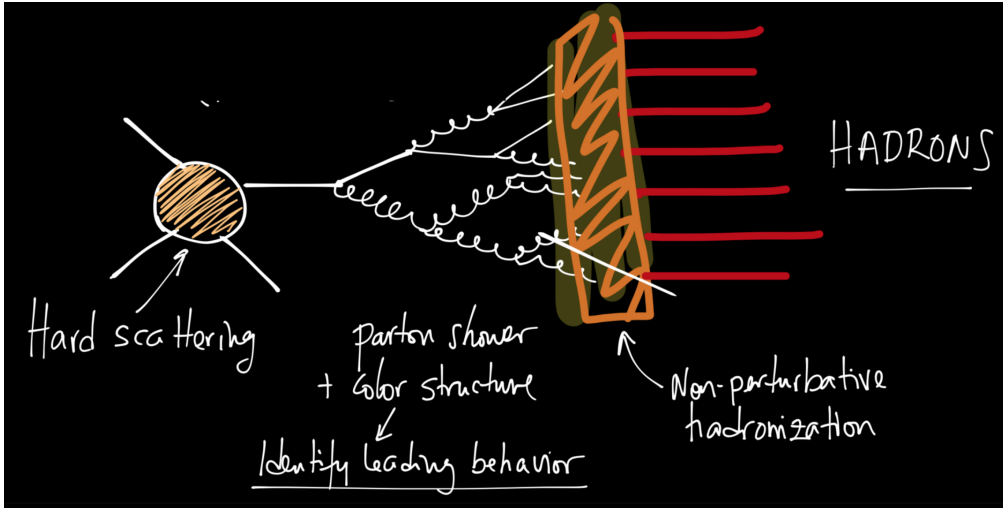


Figure 12: REPLACE FIGURE An illustration of jet showering. The highly virtual parton from the hard scattering will produce a shower of softer partons. When the virtuality is low enough the shower will go through a hadronisation process that produces the hadrons, which will be eventually observed in the detector.

$$\frac{d\sigma_{pp}^h}{dy d^2 p_T} = K \sum_{abcd} \int dx_a dx_b f_a(x_a, Q^2) f_b(x_b, Q^2) \frac{d\sigma}{dt} (ab \rightarrow cd) \frac{D_{h/c}^0}{\pi z_c}$$

$$x_a = \frac{|p_a|}{|p_{proton}|}$$

⁵⁷⁹ Parton Distribution Function

⁵⁸⁰ Parton Distribution Functions (PDFs) are essential to calculate the scattering cross
⁵⁸¹ section. They are extracted from comprehensive global analysis of experimental
⁵⁸² results from a variety of fixed-target and collider experiments. PDFs $f_a(x)$ give the
⁵⁸³ differential probability for parton a to carry momentum fraction x of the proton
⁵⁸⁴ momentum.

⁵⁸⁵ PDFs cannot be calculated from first principles. In practice the PDFs are
⁵⁸⁶ measured in Deeply Inelastic Scattering (DIS) experiments and are extrapolated
⁵⁸⁷ to the relevant momentum scales at LHC using the Dokshitzer-Gribov-Lipatov-
⁵⁸⁸ Altarelli-Parisi (DGLAP) evolution scheme [?] 14.

$$\mu_F^2 \frac{\partial f_i(x, \mu_F^2)}{\partial \mu_F^2} = \sum_j \frac{\alpha_s(\mu_F)}{2\pi i} \int_x^1 \frac{dz}{z} P_{ij}(z) f_j\left(\frac{x}{z}, \mu_F^2\right), \quad (14)$$

589 where μ_F is a factorization scale. The splitting functions P_{ij} describe a probability to radiate parton i from parton j as a function of the momentum fraction z carried away by the offspring parton.

592 The final component in the factorization, fragmentation functions, describe
 593 the distribution of the fractional momenta of particles radiated from the outgoing
 594 parton. Fragmentation function are given with respect to the momentum fraction
 595 z which is defined as the longitudinal momentum fraction of jet momentum p_{jet}
 596 carried away by the jet fragment p_{part}

$$z = \frac{\bar{p}_{\text{part}} \cdot \bar{p}_{\text{jet}}}{p_{\text{jet}}^2} = \frac{p_{\text{part}}}{p_{\text{jet}}} \Big|_{\bar{p}_{\text{part}} \times \bar{p}_{\text{jet}} = 0} \quad (15)$$

597 Fragmentation function $D(z)$ then gives the average multiplicity m of jet fragments having $z > z_0$ [].

$$m(z_0) = \int_{z_0}^1 D(z) dz \Rightarrow m(0) \equiv \langle m \rangle = \int_0^1 D(z) dz \quad (16)$$

599 Because of momentum conservation the sum of all jet fragments must be equal
 600 to the jet momentum, i.e.

$$\sum p_{i,\text{part}} = p_{\text{jet}} \Rightarrow \sum z_i = 1 \Rightarrow \int_0^1 z D(z) dz = 1 \quad (17)$$

601 A natural consequence is that the average momentum fraction is the inverse of
 602 the average multiplicity

$$\langle z \rangle = \frac{\int_0^1 z D(z)}{\int_0^1 D(z)} = \frac{1}{\langle m \rangle} \quad (18)$$

603 1.5.2 Jet hadronisation

604 When the parton shower reaches a scale close to Λ_{QCD} , the perturbative description
 605 is no longer valid. Thus the hadronisation stage must be described in a
 606 non-perturbative manner. One simple scenario that is used in several theory calculations
 607 is the so-called local parton-hadron duality [62]. In the local parton-hadron
 608 duality hypothesis it is assumed that there exists a low virtuality scale Q_0 in which
 609 the hadronisation happens, that is independent of the scale of the primary hard
 610 process. At this scale the partons are transformed into hadrons, assuming that the
 611 flow of momentum and quantum numbers for the hadrons can be directly obtained
 612 from those of partons introducing only small normalising constants.

613 Hadronisation is assumed to be universal, i.e. it shouldn't depend on the
 614 collision energy or system.

615 **Lund string model**

616 One common implementation in MC generators is the Lund string fragmentation
617 algorithm [63]. The string model is based on the fact that in QCD linear confinement
618 is expected over large distances [64]. This can be modelled by imagining a
619 colour flux tube being stretched between the outgoing partons. The left side of
620 Fig. 14 illustrates this point for a $q\bar{q}$ -pair. The tube is assumed to have a uniform
621 fixed transverse size of about 1 fm along its length, which leads to a linearly rising
622 potential $V(r) = \kappa r$, where the string constant κ describes the amount of energy
623 per unit length. A value of $\kappa \approx 1\text{GeV}/\text{fm} \approx 0.2\text{GeV}^2$ can be obtained from hadron
624 mass spectroscopy.

625 The evolution of string fragmentation is illustrated schematically on the right
626 side of Fig. 14. This figure is drawn in a light cone presentation, so the initial
627 quark and antiquark are going to separate directions at the speed of light, which
628 assumes them as massless. The string between them, illustrated in the figure by
629 the red line, stretches until its potential energy becomes high enough that it can
630 break, forming a new quark-antiquark pair. If the original pair was $q\bar{q}$ and the
631 new pair $q'\bar{q}'$, now two new pairs $q\bar{q}'$ and $q'\bar{q}$ have formed. As these particles
632 are also moving away from each other, the strings between them can stretch and
633 break, creating yet more pairs. The process continues until the invariant mass of
634 the system connected by the string becomes small enough and a final state meson
635 is formed.

636 To mathematically model the string one can use a massless relativistic string
637 with no transverse degrees of freedom. The gluons are represented as energy and
638 momentum carrying kinks on the string with incoherent sums of one colour charge
639 and one anticolour charge. When this string breaks, it is classically required that
640 the created quark and antiquark are produced at a certain distance if they are to
641 have any mass or transverse momentum. However, taking into account quantum
642 mechanics, the pair must be created at one point and then tunnel out to the
643 classically allowed region. Thus the probability to create a new quark-antiquark
644 pair becomes proportional to the tunnelling probability [63].

$$P_{\text{tunnelling}} \propto \exp\left(\frac{-\pi m_\perp^2}{\kappa}\right) = \exp\left(\frac{-\pi m^2}{\kappa}\right) \left(\frac{-\pi p_\perp^2}{\kappa}\right), \quad (19)$$

645 where the transverse mass m_\perp is defined as $m_\perp^2 = m^2 + p_\perp^2$. The transverse
646 momentum is now defined to be transverse to the string axis. This formula gives
647 flavour-independent Gaussian p_\perp -distribution for the created $q\bar{q}$ pairs.

648 As explained above the string fragmentation would only produce mesons in
649 the final state, but we know that also baryons are created in the process. In the
650 string fragmentation model baryon production is included by adding a probability
651 that a diquark-antidiquark pair is created instead of a quark-antiquark pair when

652 a string breaks.

653 The kinematics of each string breaking are determined iteratively. Since there
654 is no natural ordering, the string breaking can be considered in any order and
655 the answer obtained must be the same. One can start from the q leg and work
656 one's way to the \bar{q} leg, or vice versa. This give a left-right symmetry of the
657 string fragmentation. In the Lund model this is taken into account by defining a
658 symmetric fragmentation function

$$f(z) \propto \frac{1}{z} (1-z)^a \exp\left(-\frac{bm_{\perp}^2}{z}\right) \quad (20)$$

659 to break the string into a hadron and a remainder system. In the function z is
660 the fraction of light-cone momentum p^+ given to the hadron in the string breaking,
661 m_{\perp} is the transverse mass of the hadron and a and b are tuneable parameters of
662 the model. For heavy quarks this has to be modified as

$$f(z) \propto \frac{1}{z^{1+bm_Q^2}} (1-z)^a \exp\left(-\frac{bm_{\perp}^2}{z}\right) \quad (21)$$

663 The process can be thought as follows: first start from the q-leg of a $q\bar{q}$ system
664 and choose to consider the breaking to new $q'\bar{q}'$ pair closest to this leg. Now the
665 breaking will produce a hadron $q\bar{q}'$ and a remainder system spanning from $q'\bar{q}$.
666 Then the process is continued until the \bar{q} -leg is reached. A small detail here is
667 that in equation (20) it is assumed that the mass of the remainder system is large.
668 Thus some patching up is needed for the last two hadrons coming from a string.
669 The patching up is done such that the place where it happens looks as closely like
670 any other string break as possible.

671 One additional possibility one must consider is that a string can have such a
672 low mass that it cannot break at all. In this case a single hadron is generated out
673 of the string and if necessary energy and momentum are exchanged with other
674 partons in the event.

675 After all the hadrons are produced, the short-lived ones can still decay before
676 the set of final state particles in the simulation is obtained []

677 Cluster model

678 Instead of a string model HERWIG [] uses a cluster model [65] for hadronisation.
679 The advantage of cluster models is that they require a smaller number of param-
680 eters than string models. The model is based on the preconfinement property of
681 parton showers, i.e. the colour structure of the shower at any evolution scale Q_0 is
682 such that colour singlet combinations of partons can be formed with an asymptot-
683 ically universal invariant mass distribution. The invariant mass does not depend

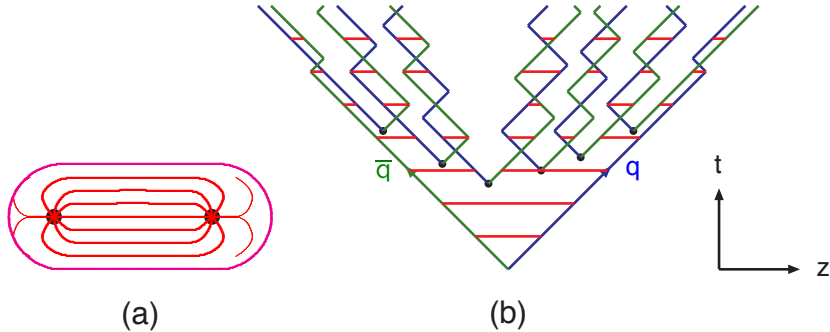


Figure 13: (a) A flux tube spanned between a quark and an antiquark. (b) The motion and breakup of a string system, with the two transverse degrees of freedom suppressed (diagonal lines are (anti)quarks, horizontal ones snapshots of the string field). [64]

on the initial hard process scale Q , but only on Q_0 and the QCD scale Λ_{QCD} , when $Q \gg Q_0$.

The cluster model starts from transforming all gluons non-perturbatively into $q\bar{q}$ pairs, which requires that the gluons get a mass, which must be at least twice the lightest quark mass. After the gluons are transformed into quarks, the adjacent colour lines can be clustered together to colour singlet states with mesonic quantum numbers. The momentum of these clusters is defined to be the sum of the momenta of the clustering partons. According to preconfinement, the mass distribution of these clusters is independent of the details of the hard scattering. Additionally the clusters can be regarded as highly excited hadron resonances and decayed into the final state hadrons.

Some of these initial clusters are too heavy to reasonably describe an excited state of a hadron. These must be split before they are allowed to decay. The cluster C is split if its mass fulfills the condition []

$$M_C^p \geq M_{\max}^p + (m_1 + m_2)^p, \quad (22)$$

where $m_{1,2}$ are the masses of the constituents partons of the cluster and M_{\max} and p are the main parameters of the model. These have to be chosen separately for clusters containing light, charmed and bottom quarks. When a cluster is split, a pair of light quarks is generated from the vacuum and two new clusters are made, both containing one quark from the original cluster and one from the newly generated pair. The splitting is continued until no clusters with masses M_C fulfilling the equation 22 remains.

When are clusters are light enough, they decay into final state hadrons. If the mass of the cluster is high enough for decaying into a baryon-antibaryon pair,

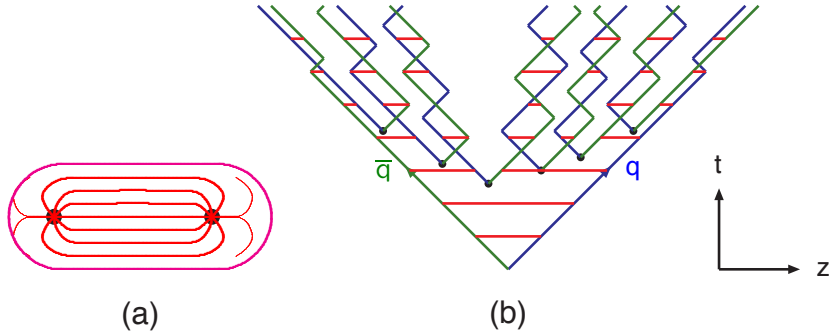


Figure 14: Colour structure of a parton shower to leading order in N_c . [64]

there is a parameter deciding whether the cluster undergoes mesonic or baryonic decay. For a mesonic decay a quark-antiquark pair is created from the vacuum and for the baryonic decay a diquark-antidiquark pair is made. Then the exact decay products are chosen and the cluster decays isotropically in the rest frame of the cluster. If there are partons produced in the perturbative phase involved in the decay, they retain their original direction in the cluster rest frame, up to some Gaussian smearing. If the cluster mass is too low to decay into a pair of mesons, it decays into the lightest possible hadron and some energy and momentum is exchanged with the adjacent clusters. At the end we are left with the final state hadrons, some of which might still decay until the end of the simulation if they are very short-lived. []

1.5.3 Jet energy loss

Figure 15 shows the relevant medium modification phenomena for different regions of the phase space at time t , when a jet propagates through a thermal cloud of temperature T . As in practice jets propagate over a finite path-length L in QCD matter, Fig. 15 can be taken as a representation of the distribution of partonic jet fragments at moment $t \approx L$, when the jet escapes the medium.

The region marked as DGLAP is dominated by the primary vacuum splittings. This region is determined by $\theta > \theta_{\text{vac}}$ with

$$\theta_{\text{vac}} \propto 1/\sqrt{pt}. \quad (23)$$

Medium-induced parton branching fills the log p -log- θ -plane from the bottom up (in p) and from the inside out (in θ). This is because transverse momentum is acquired by Brownian motion in the medium, $k_\perp^2 \propto \hat{q}t$. Then the formation time constraint $t \geq p/k_\perp^2 \approx p/\hat{q}t$ implies that medium-induced quanta can be formed in the region $p \leq k_{\text{form}}$ where

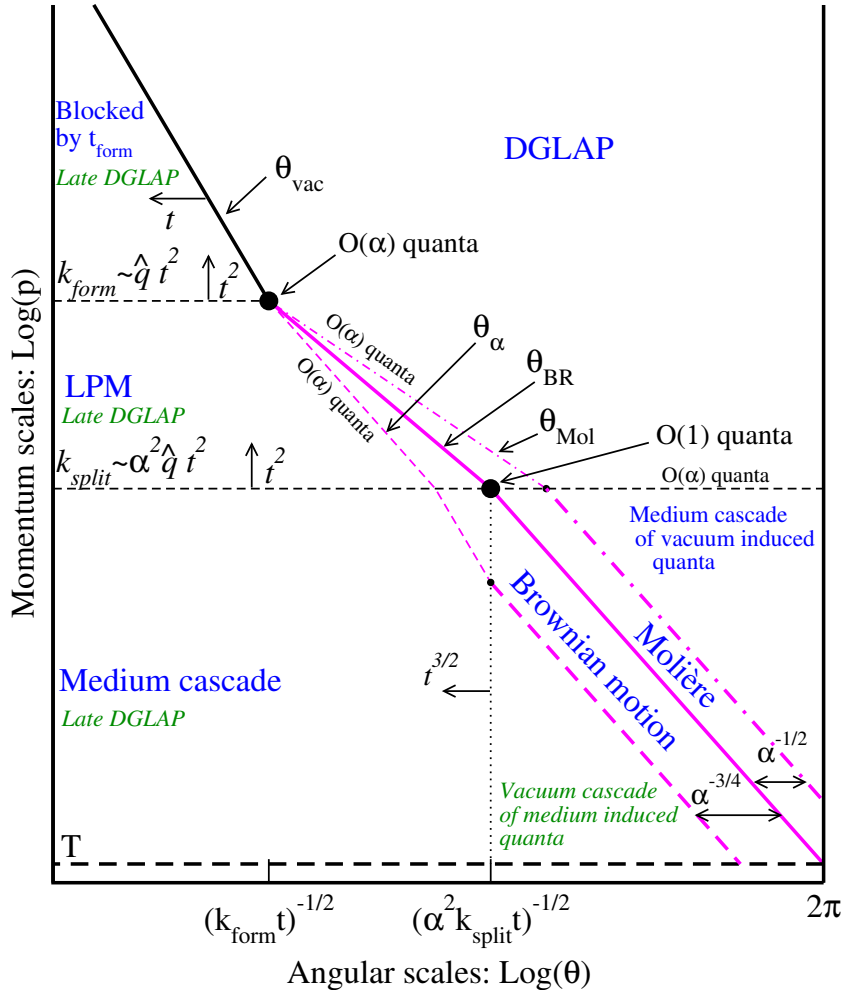


Figure 15: Parametrically accurate picture of how a medium-modified parton cascade fills the phase space. At time t , quanta can be formed up to momentum scale k_{form} and they are formed with $O(1)$ probability per $\log p$ at lower scale k_{split} . Quanta below k_{split} split further and their energy cascades to the thermal scale T in less than an epoch t . Transverse Brownian motion moves quanta up to the angle $\theta_{\text{BR}}(p)$ denoted by the thick purple line. The Molière region at larger θ is dominated by rare large angle scattering. At even larger angle, there are $O(\alpha_s)$ quanta per double logarithmic phase space from DGLAP ‘vacuum’ radiation, and for momenta below k_{split} these cascade within time t to T . After the jet escapes the medium, the jet and the emitted fragments will undergo vacuum radiation. This late time vacuum radiation emitted by the original parton dominates at sufficiently small $\log \theta$ (regions marked “late DGLAP” and bounded by θ_{vac} and θ_α), whereas the late time radiation of the fragments dominates in the region denoted by “Vacuum cascade of the medium induced quanta”. [66].

$$k_{\text{form}}(t) = \hat{q}t^2$$

731 .

732 The probability of finding a splittee with a momentum p with $p < k_{\text{form}}$ is

$$\frac{dP_{\text{find}}(t)}{d \log p} \propto \alpha_s t/t_{\text{form}}(p) \propto \alpha_s \hat{q}^{nicefrac{1}{2}} p^{-1/2} t \quad (24)$$

733 Not all quanta will stay where they were created. Those modes that have time
 734 to lose a significant fraction of their energy will cascade to a significantly lower
 735 scale p . For LPM-type radiation, the splitting that degrades energy the most is
 736 the hardest splitting.

737 The $\log p$ distribution has the same $\frac{1}{\sqrt{p}}$ dependence as in the LPM region

$$\frac{dn}{d \log p} = \frac{1}{p} \frac{d\epsilon}{d \log p} \approx \alpha_s \frac{\sqrt{\hat{q}t}}{\sqrt{p}} \quad (25)$$

738 Also the quanta originating from the DGLAP region will undergo medium
 739 interactions that will make the quanta radiate and split. The distribution of radi-
 740 ation is the same as from any other mode. Above a certain momentum scale k_{split}
 741 the distribution of originating daughters is

$$\frac{dP_{\text{find}}}{d \log p d \log \theta} \approx \alpha_s \frac{t}{t_{\text{split}}(p)}, \quad (26)$$

742 Note that the ratio t/t_{split} is smaller than 1 for nodes above k_{split} and therefore
 743 the number of daughters is smaller than the number of vacuum splitted quanta.
 744 Below k_{split} the cascade is similar to the medium cascade and the number of quanta
 745 become

$$\frac{dn}{d \log p d \log \theta} \approx \alpha_s \frac{t}{t_{\text{split}}(p)}, \text{ for } p < k_{\text{split}}(p) \quad (27)$$

746 The angular distribution is driven by two mechanisms; Multiple soft scatterings
 747 give rise to transverse Brownian motion, which determines the distribution at small
 748 angles. The typical angle reached in the LPM region is

$$\theta_{\text{BR}}(p) \approx \frac{\sqrt{\hat{q}t}}{p}, \text{ for } k_{\text{form}} > p > k_{\text{split}}, \quad (28)$$

749 while in the medium cascade region of the phase space this becomes

$$\theta_{\text{BR}}(p) \approx \left(\frac{T}{p}\right)^{\frac{3}{4}} \quad (29)$$

750 Large angular scales cannot be reached by Brownian motion, but can arise from
751 rare large angle scatterings, described by Molière [].

752 ...

753 "Jet quenching in heavy-ion collisions evolves multi-scale problems [?,66]. The ele-
754 mentary scattering and the subsequent branching process down to non-perturbative
755 scales are dominated by hard scales in the vacuum as well as in the medium. Soft
756 scales, of the order of the temperature of the medium, characterise the interac-
757 tions of soft partons produced in the shower with the QGP. Soft scales also rule
758 hadronisation, which is expected to take place in vacuum for sufficiently energetic
759 probes, even though some modifications can persist from modifications of color
760 flow [?, ?, ?]. Understanding the contributions from the different processes to the
761 jet shower evolution in medium and their scale dependence is crucial to constrain the
762 dynamics of jet energy loss in the expending medium, the role of colour
763 coherence [?], and fundamental medium properties like temperature dependent
764 transport coefficient [?, ?]. "

765 High momentum particles are very rare and they are only produced in the
766 initial collisions. After they are created they escape the medium before a thermal
767 equilibrium is reached. Thus they are not part of the pressure-driven collective
768 expansion. Instead high momentum yield is suppressed because of energy loss in
769 the medium. When propagating through the medium these partons lose energy as
770 they pass through the medium. This is referred to as jet quenching. Jet quenching
771 depends on the path lengths through the medium. Thus anisotropy in this region
772 is mainly dependent on the collision geometry and density of medium.

773 The energy loss of partons in medium is mainly due to QCD bremsstrahlung
774 and to elastic scatterings between the parton and the medium.

775 The radiative energy loss mechanism is given in terms of the transport coef-
776 ficient $\langle \hat{q} \rangle$, which describes the average momentum transfer between the medium
777 and parton [67]. The exact definition of this depends on the theoretical formalism
778 used to describe the energy loss mechanism.

779 Many of the energy loss models exploit the analogy between the QCD interac-
780 tion of parton propagating through the colored medium and the QED energy loss
781 of electron propagating through material. An electron propagating through matter
782 loses its energy by photon Bremsstrahlung radiation. In the simplest case, each
783 individual scattering center results in a single emission of a photon. This is known
784 as the Bethe-Heitler regime [68]. The energy spectrum of radiated photons dN/dE
785 is, in this case, proportional to $1/E$. However, the Bremsstrahlung photon, can be
786 radiated only when the distance between the scattering centers is larger than the
787 formation length. In the limit, when the scattering centers are closer than the
788 formation length, the Bremsstrahlung process is suppressed. This phenomenon

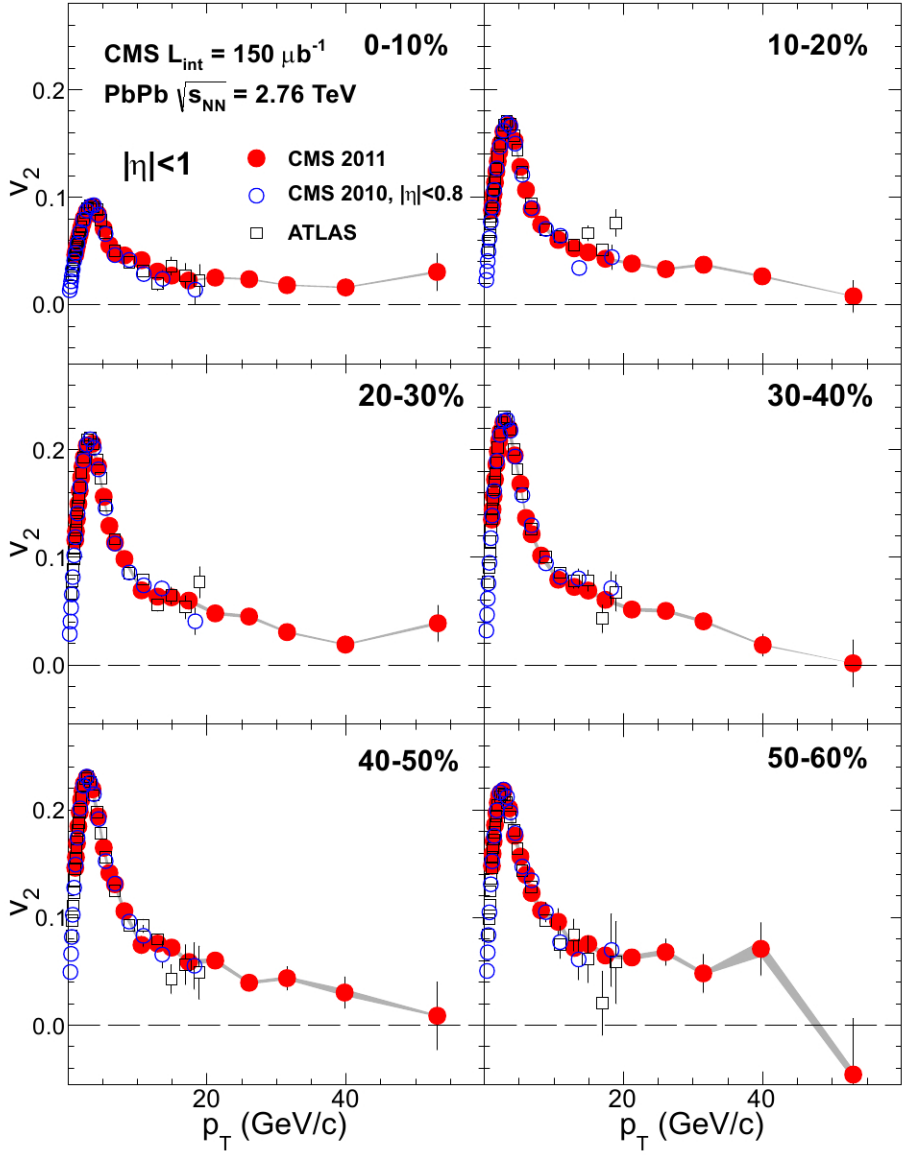


Figure 16: Elliptic flow, v_2 , as a function of the charged particle transverse momentum from 1 to 60 GeV/c with $|\eta| < 1$ for six centrality ranges in Pb-Pb collisions at $\sqrt{s_{NN}} = 2.76 \text{ TeV}$, measured by the CMS experiment. [61].

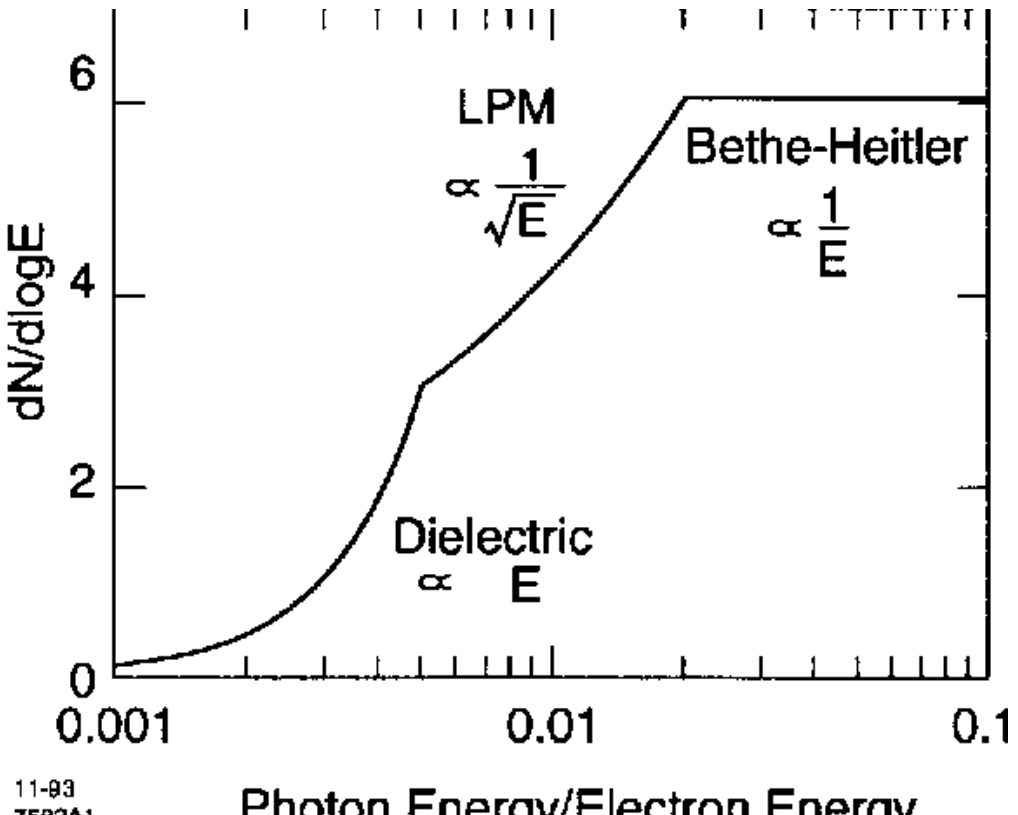


Figure 17: The expected bremsstrahlung spectrum for a electron propagating through material. [71].

is known as the Landau-Pomeranchuk-Migdal (LPM) [69, 70] suppression. The radiated spectrum in this regime is proportional to $1/\sqrt{E}$.

Lower energy photons are further suppressed by the destructive interference leading to the suppression of Bremsstrahlung photons of $E < \gamma\omega_p$, where ω_p is the plasma frequency of the radiator. This is known as Dielectric suppression. The photon energy distribution in this regime is proportional to the energy of the photon. A schematic view of the effect of these three regimes is shown in Fig. 17.

The simplest energy loss process is elastic QCD scattering off the medium partons. In elastic scatterings the recoil energy of the scattered partons are absorbed by the thermal medium, which reduces the energy of the initial parton. The mean energy loss from elastic scatterings can be estimated by

$$\langle \Delta E \rangle_{\text{el}} = \sigma \rho L \langle E \rangle_{\text{1scatt}} \propto L, \quad (30)$$

where σ is the interaction cross section and $\langle E \rangle_{\text{1scatt}}$ is the mean energy transfer of one individual scattering [72]. This assumption holds if the mean energy is

802 independent of the total energy of the parton (E). The transport coefficient of
 803 elastic scattering, $\langle \hat{q}_{\text{el}} \rangle = \langle \Delta E \rangle / L$, is defined as the mean energy loss per unit path
 804 length.

805 Another energy loss mechanism is medium-induced radiation. In QCD this
 806 radiation is mainly due to the elementary splitting processes, $q \rightarrow qg_r$ and $g \rightarrow gg_r$.
 807 Assuming that the parton is moving with the speed of light radiation energy loss
 808 can be estimated by

$$\langle \Delta E \rangle_{\text{rad}} \propto T^3 L^2, \quad (31)$$

809 where L is the length of the medium and T is its temperature [73]. The different
 810 exponents of L in equations 30 and 31 indicate that radiative energy loss is
 811 dominant over elastic energy loss.

812 There are several models that attempt to describe the nature of the energy loss
 813 mechanism. The most used models can be divided into four formalisms.

814 In the Gyulassy-Levai-Vitev (GLV) [74] opacity expansion model the radiative
 815 energy loss is considered on a few scattering centers N_{scatt} . The radiated gluon
 816 is constructed by pQCD calculation as summing up the relevant scattering am-
 817 plitudes in terms of the number of scatterings. Another approach into opacity
 818 expansion is the ASW model by Armesto, Salgado and Wiedermann [75].

819 Thermal effective theory formulation by Arnold, Moore and Yaffe (AMY) [76]
 820 uses dynamical scattering centers. It is based on leading order pQCD hard thermal
 821 loop effective field theory. This model assumes that because of the high temper-
 822 ature of the plasma the strong coupling constant can be treated as small. The
 823 parton propagating through the medium will lose energy from soft scatterings and
 824 hard scatterings.

825 The above models calculate the energy loss while the parton propagates through
 826 the medium, focusing on the pQCD part. The higher twist (HT) approach by Wang
 827 and Guo [77] implements the energy loss mechanism in the energy scale evolution
 828 of the fragmentation functions.

829 The last category is formed by the Monte Carlo methods. The PYTHIA event
 830 generator [78] is widely used in high-energy particle physics. Two Monte Carlo
 831 models based on PYTHIA describing the energy loss mechanism are PYQUEN [79]
 832 and Q-Pythia [80]. Other Monte Carlo models include JEWEL [81] and Ya-
 833 JEM [82].

834 Jet quenching in heavy-ion collisions is usually quantized with the nuclear
 835 modification factor R_{AA} , which is defined as

$$R_{AA}(p_T) = \frac{(1/N_{AA}^{\text{evt}}) dN^{AA}/dp_T}{\langle N_{\text{coll}} \rangle (1/N_{pp}^{\text{evt}}) dN^{pp}/dp_T} \quad (32)$$

836 where dN^{AA}/dp_T and dN^{pp}/dp_T are the yields in heavy-ion and proton-proton

837 collisions, respectively and $\langle N_{coll} \rangle$ is the average number of binary nucleon-nucleon
 838 collisions in one heavy-ion event. The number of binary collisions can be calculated
 839 from the Glauber model as shown in Sec. 1.3.2. From the point of view of direct
 840 production a heavy-ion collision can be estimated relatively well to be only a series
 841 of proton-proton collisions.

842 If the medium has no effect on high p_T particles the nuclear modification factor
 843 should be 1. At RHIC and LHC this has been observed to be as low as 0.2 because
 844 of jet quenching. Measurements of R_{AA} from different sources are shown in Fig. 18

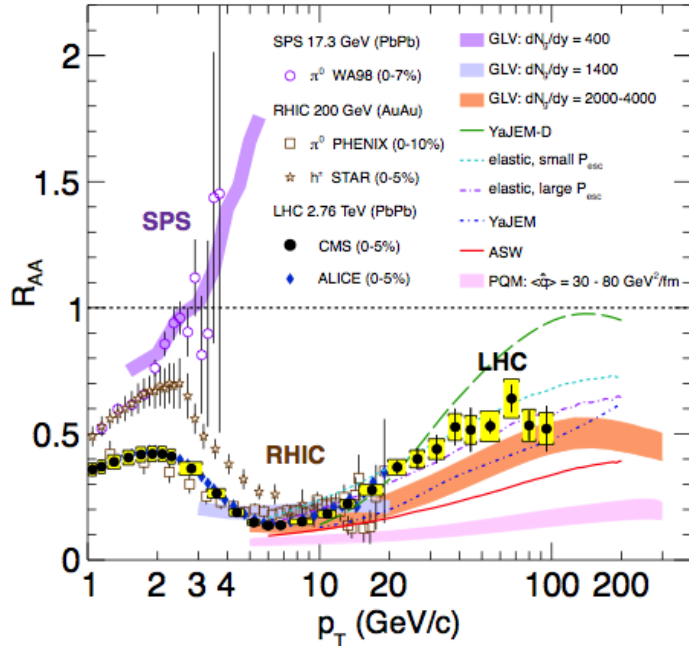


Figure 18: Measurements of the nuclear modification factor R_{AA} in central heavy-ion collisions at three different center-of-mass energies, as a function of p_T , for neutral pions (π^0), charged hadrons (h^\pm), and charged particles [83–87], compared to several theoretical predictions [34, 88–92]. The error bars on the points are the statistical uncertainties, and the yellow boxes around the CMS points are the systematic uncertainties. The bands for several of the theoretical calculations represent their uncertainties [93].

845 The nuclear modification factor can also be used to quantify anisotropy. In
 846 the study of anisotropy R_{AA} in-plane and out-of-plane can be compared. The
 847 distance traveled through medium is largest out-of-plane which leads to stronger
 848 suppression in this direction. The nuclear modification factor as a function of
 849 $\Delta\phi = \phi - \psi_n$ is given by

$$\begin{aligned}
R_{AA}(\Delta\phi, p_T) &= \frac{(1/N_{AA}^{evt}) d^2 N^{AA}/d\Delta\phi dp_T}{\langle N_{coll} \rangle (1/N_{pp}^{evt}) dN^{pp}/dp_T} \approx \frac{dN^{AA}/dp_T (1 + 2 \cdot v_2 \cos(2\Delta\phi))}{\langle N_{coll} \rangle dN^{pp}/dp_T} \\
&= R_{AA}^{incl}(p_T) (1 + 2 \cdot v_2 \cos(2\Delta\phi)). \tag{33}
\end{aligned}$$

850 The yield of proton-proton collisions is independent of the reaction plane and
851 the yield in heavy-ion collisions is modulated by the second harmonics. In Eq. (33)
852 R_{AA} is approximated only up to the second harmonics. From Eq. (33) it follows
853 that

$$\frac{R_{AA}(0, p_T) - R_{AA}(\pi/2, p_T)}{R_{AA}^{incl}(p_T)} \approx \frac{R_{AA}^{incl}(p_T) (1 + 2 \cdot v_2 - (1 - 2 \cdot v_2))}{R_{AA}^{incl}(p_T)} = 4 \cdot v_2 \tag{34}$$

854 The observed $R_{AA}(\Delta\phi, p_T)$ from PHENIX measurements in Au-Au collisions at
855 $\sqrt{s} = 200\text{GeV}$ [94] is compared to R_{AA} using v_2 via Eq. (33) in Fig. 19. They
856 agree very well within the statistical errors for all centrality and p_T bins.

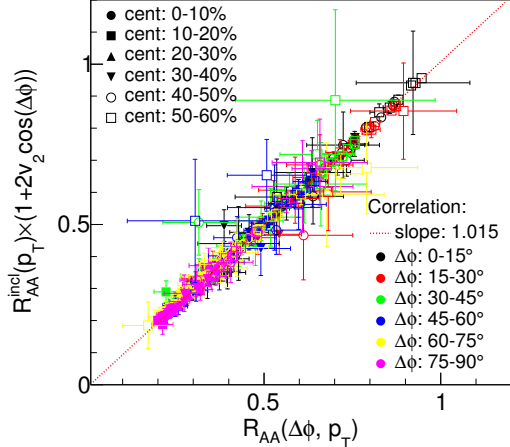


Figure 19: A comparison between observed $R_{AA}(\Delta\phi, p_T)$ and R_{AA} using v_2 from PHENIX measurements of Au-Au collisions at $\sqrt{s} = 200\text{GeV}$. On the X-axis is the measured $R_{AA}(\Delta\phi, p_T)$. On the y-axis is the inclusive R_{AA} multiplied by $1 + 2v_2 \cos(\Delta\phi)$ [94].

856 At high- p_T , the pQCD processes are dominant, hence the v_n (or $R_{AA}(\Delta\phi, p_T)$)
857 characterize the pathlength-dependence of the energy loss process.
858

859 Jet quenching is not the only high p_T phenomenon studied in heavy-ion collisions.
860 Another property is jet fragmentation. The high momentum parton created
861 in the initial collision fragments into a number of partons with smaller p_T . Jet
862 fragmentation occurs also in proton-proton collisions in the vacuum, but it can
863 be modified due to the presence of the medium. In order to study the jet frag-
864 mentation function ($D(z)$, where $z = p_T^h/p_T^{part}$) modification due the medium, we
865 use the two-particle correlations. The particle yield can be extracted from the
866 correlation function. The background from the flow processes is correlated and
867 needs to be subtracted to get the particle yield associated only with the jet. The
868 ratio of the jet yields in Au-Au and p-p collision $I_{AA} = Y^{Au+Au}/Y^{p+p}$ character-
869 izes the jet fragmentation modification [95]. I_{AA} probes the interplay between the
870 parton production spectrum, the relative importance of quark-quark, gluon-gluon
871 and quark-gluon final states, and energy loss in the medium.

872 1.5.4 Monte Carlo Implementations

873 1.6 QGP in Small systems

874 After the existence of QGP in heavy ion collisions has been established, attention
875 has been turned to small systems. Proton-proton (pp) and proton-Lead (pPb)
876 collisions have been studied at LHC and RHIC has studied a host of different
877 collision systems; namely proton-Gold (pAu), deuteron-Gold (dAu) and Helium³-
878 Gold (He³Au) collisions starting in 2000.

879 Already before the era of modern colliders, collective behaviour in proton-
880 proton collisions was considered by names like Heisenberg, Fermi and Bjorken. [96]
881 Eventually there were some experimental searches of QGP in pp and $p\bar{p}$ collisions
882 in E735 at Tevatron [97] and MiniMAX [98]. However no conclusive evidence was
883 found.

884 In the early years of RHIC these small systems were mostly considered as con-
885 trol measurement, for example in constraining nuclear modified parton distribution
886 functions (nPDFs) that determine the initial gluon distributions that determine
887 the first epoch of heavy ion collisions [99, 100].

888 In 2010 ultrahigh-multiplicity pp collisions were studied at CMS. The study
889 found that particles had a weak but clear preference to be emitted along a com-
890 mon transverse ϕ angle across all rapidities [101]. This seemed like behaviour
891 were similar to AA collisions, but it was argued that it could as well come from
892 momentum correlations present in the earliest moments of the collision.

893 In 2012 LHC ran its first pPb data taking period. Around the same time
894 dAu data was reexamined at RHIC. Now it was revealed that most of the flow
895 signatures attributed to hydrodynamic expansion in AA collisions also existed in
896 smaller systems.

897 -Sub nucleonic structure needed to describe intial conditions in pA, pp

898 1.6.1 Collective phenomena

899 The most rugged analysis of collective behaviour concerns the two (or more) parti-
900 cle correlations, often parametrised via the relative azimuthal angle and pseudora-
901 pidity differences, $\Delta\phi$ and $\Delta\eta$ respectively. Figure 21 shows two-particle correla-
902 tions measurements in PbPb, pPb and pp collisions at the LHC. In PbPb collisions
903 long-range correlations dominate over short-range phenomena. This shows in the
904 two ridges at $\Delta\phi = 0$ and $\Delta\phi = \pi$. At $\Delta\phi \approx \Delta\eta \approx 0$, there is a peak coming from
905 single jet fragmentation. Since the away-side jet can be spread out in $\Delta\eta$, this
906 contribution disappears when compared to the flow contribution at the away side
907 ridge. In pPb, and pp the near side peak is more distinguished and the away-side
908 jet contribution starts to show. Still, one can see long-range correlations that seem
909 like flow-like collective behaviour in both systems.

910 In addition to the two particle correlations, correlations have been observed in
911 the form of v_n coefficients both at LHC and at RHIC. The results have also been
912 described with hydrodynamical models, although the applicability of said models
913 is questionable, because of the large Reynolds numbers in small systems. Figure
914 20 shows results for v_2 in different collisions systems at RHIC as measured by
915 PHENIX. These different systems provide also different initial geometries. dAu
916 collisions naturally have an ellipsoidal form, while a He3 collision has a triangular
917 form and thus produces larger triangular flow, v_3 components.

918 Other observations that produce flow-like results include mass ordered v_2 coeffi-
919 cients and higher order harmonics coming from fluctuations in the initial geometry.

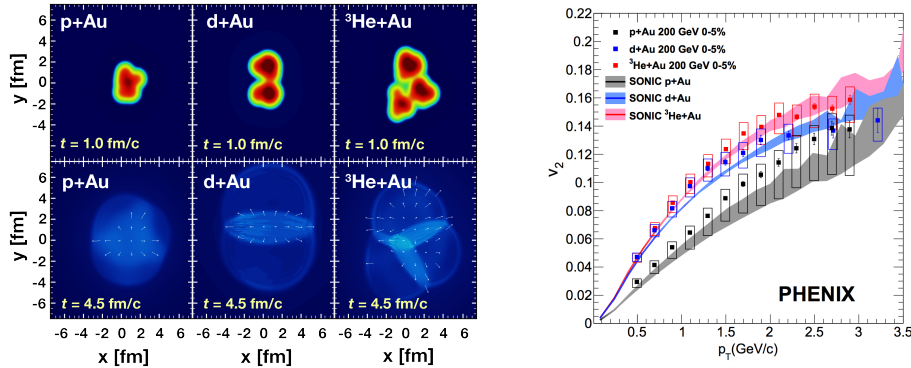


Figure 20: Calculations of the intial energy density in small collision systems at RHIC and the resulting hydrodynamic evolution.

920 Thus all the major collective flow phenomena observed in heavy-ion collisions have
 921 been also identified in small systems.

922 One open question is identifying the point the point, where flow-like correlations end. The question has proved challenging since low multiplicity events are
 923 dominated by non-flow phenomena. This makes observations in low multiplicity
 924 events model/method dependant. Different methods assess non-flow contributions
 925 differently. Thus some methods fail to observe a signal in cases, where others do
 926 and it is unclear whether this is true collective motion or it comes from non-flow
 927 contributions.

929 1.6.2 Absence of jet quenching

930 In A+A collisions, an important confirmation of the standard model comes from
 931 the energy loss of high p_T partons traversing the medium, referred to as jet quench-
 932 ing [102–104]. In 2003 the jet quenching effect was observed to disappear in d+Au
 933 collisions. This was taken as an indication that no QGP was created. Similarly at
 934 LHC no jet modification has been observed in pPb collisions. Fig. 22 shows the
 935 nuclear modification factor R_{pA} in pPb collisions as measured at the LHC.

936 The lack of jet modification seems surprising considering the multitude of flow
 937 observations supporting the existence of QGP in small systems. One possible
 938 explanation is simply the size of medium. In PbPb collision partons traversing
 939 through the medium lose energy to the medium. If the medium is very small there
 940 is limited time for interaction with the medium.

941 Calculations indicate that there should be modification in the most central
 942 pPb collisions, but selecting these in the analysis is complicated. In PbPb colli-
 943 sions most of the particle production comes from the medium and thus the total
 944 multiplicity is a good indicator of centrality. In pPb collisions, however the total
 945 multiplicity is smaller and is more strongly influenced by jet phenomena. Events

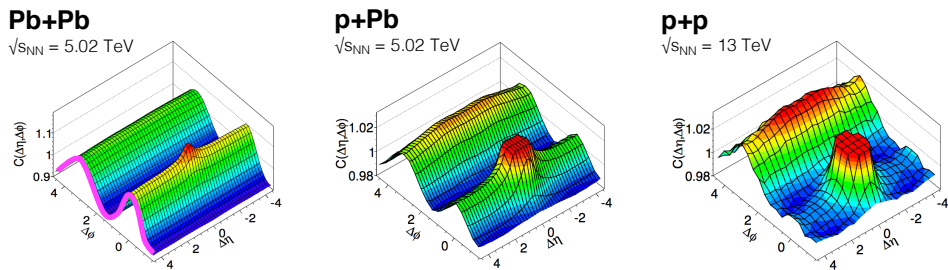


Figure 21: Two-particle correlation results in PbPb, pPb, and pp collisions at the LHC [1].

946 with jets have naturally larger multiplicities and are more likely to be classified as
 947 central events.

948 So far the only observable indicative of jet quenching in pPb collisions is the
 949 high $p_T v_2$. In heavy-ion collisions this is not explained by hydrodynamics. Instead
 950 it is assumed to come from jet quenching with different path lengths through the
 951 medium in different directions. In Fig.22 ATLAS and CMS measurements of v_2 in
 952 pPb and PbPb collisions are shown. The pPb results seem to follow a very similar
 953 pattern. But

Table 1: Summary of observations in small system

Observable	PbPb	pPb	pp
Jet RpA/RAA	Modified	No modification	-
Hadron RpA/RAA	Modified	No modification	-
Heavy flavors			
Jet shape	Broadening	No observations	-
Two-particle correlations	Ridge	Ridge	Ridge
v_2	Observed	Observed	Observed
Mass ordered flow			
Higher ordered harmonics			
High $p_T v_2$	Observed	Maybe	-

954 1.6.3 Centrality determination in small systems

955 In lead-lead collisions the total multiplicity of the event is a good indicator of the
 956 centrality of the collision. In proton-lead collisions the connection of multiplicity

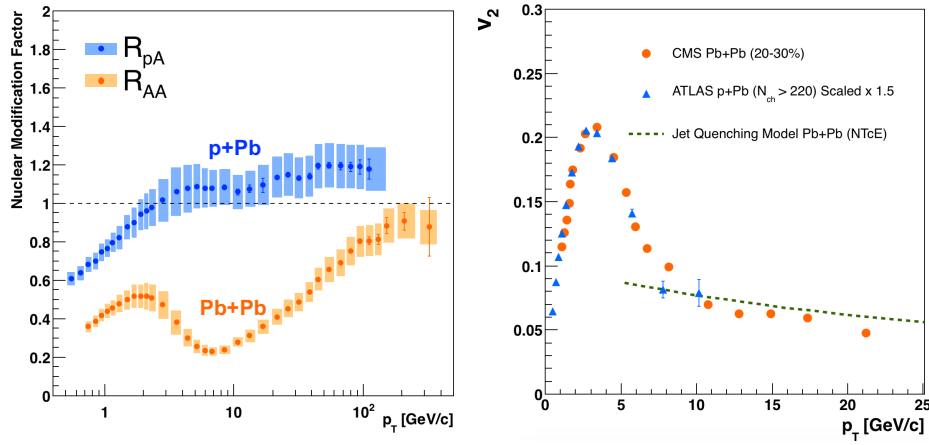


Figure 22: RpA in proton-lead collisions

ity and centrality is less clear. In p–Pb collisions the impact parameter is only loosely correlated to N_{part} or N_{coll} . Hence, although one uses traditionally the term centrality to refer to these measurements, the relevant parameters are N_{part} and N_{coll} [1].

The Glauber model [?] is generally used to calculate geometrical quantities of nuclear collisions (A–A or p–A). In this model, the impact parameter b controls the average number of participating nucleons N_{part} and the corresponding number of collisions N_{coll} . It is expected that variations of the amount of matter overlapping in the collision region will change the number of produced particles, and parameters such as N_{part} and N_{coll} have traditionally been used to describe those changes quantitatively, and to relate them to pp collisions.

The problem in p–Pb collisions, is that fluctuations in multiplicity coming from for example hard scatterings are of the same order as the differences in multiplicity between centrality classes. In Pb–Pb collisions these multiplicity fluctuations have little influence on the centrality determination, the range of N_{part} or N_{coll} is large and $P(M|v)$ converges quickly to a Gaussian with a small width relative to the range of v .

Thus in practice selecting high multiplicity one chooses not only large average N_{part} , but also positive multiplicity fluctuations leading to deviations from the binary scaling of hard processes. These fluctuations are partly related to qualitatively different types of collisions. High multiplicity nucleon-nucleon collisions show a significantly higher particle mean transverse momentum. They can be understood as harder collisions with larger momentum transfer Q^2 or as nucleon-nucleon collisions where multiple parton-parton interactions (MPI) take place. This is illustrated in Fig. 24.

Of particular interest are estimators from kinematic regions that are causally disconnected after the collision. The measurement of a finite correlation between them unambiguously establishes their connection to the common collision geometry. Typically these studies are performed with observables from well separated pseudorapidity (η) intervals, e.g. at zero-degree (spectators, slow-nucleons, deuteron break-up probability) and multiplicity in the rapidity plateau.

One centrality selection that is argued not to induce a bias on the binary scaling of hard processes is provided by the energy measurement with the Zero Degree Calorimeters (ZDC) in ALICE, due to their large η -separation from the central barrel detectors. They detect the "slow" nucleons produced in the interaction by nuclear de-excitation processes or knocked out by wounded nucleons.

Additional kinematic biases exist for events containing high- p_{T} particles, which arise from the fragmentation of partons produced in parton-parton scattering with large momentum transfer. Their contribution to the overall multiplicity increases with increasing parton energy and thus can introduce a trivial correlation between

the centrality estimator and the presence of a high- p_T particle in the event. For very peripheral collisions, the multiplicity range that governs the centrality for the bulk of soft collisions can represent an effective veto on hard processes. For the nuclear modification factor this would lead to $R_{pPb} < 1$.

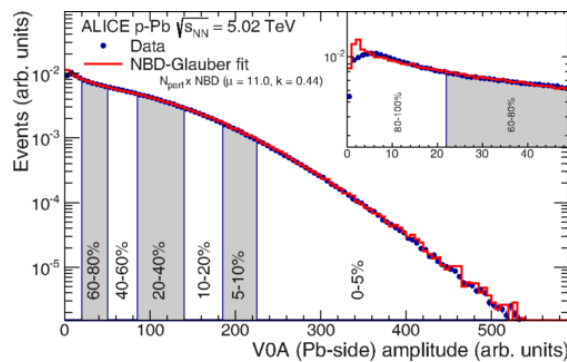


Figure 23: Distribution of the sum of amplitudes in the V0A hodoscopes (Pb-going), as well as the NBD-Glauber fit (explained in the text). Centrality classes are indicated by vertical lines. The inset shows a zoom-in on the most peripheral events. [1]

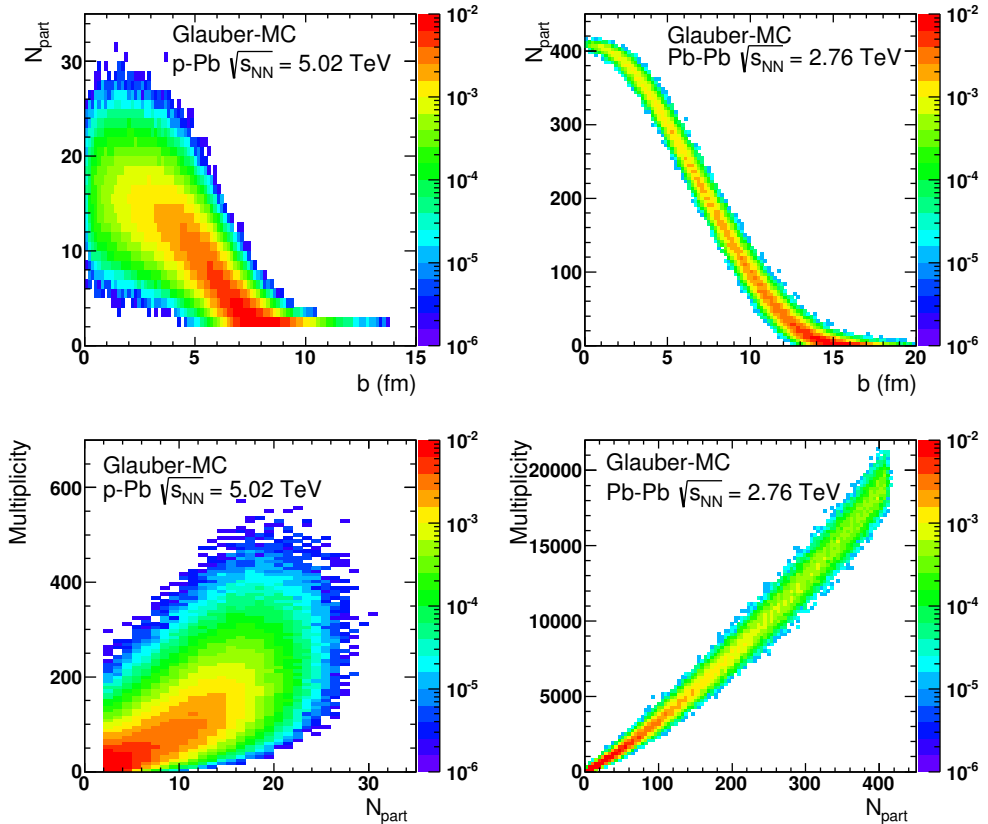


Figure 24: Top: Scatter plot of number of participating nucleons versus impact parameter; Bottom: Scatter plot of multiplicity versus the number of participating nucleons from the Glauber fit for V0A. The quantities are calculated with a Glauber Monte Carlo of p-Pb (left) and Pb-Pb (right) collisions. [1]

1001 2 Experimental setup and data samples

1002 The $\sqrt{s_{\text{NN}}} = 5.02$ TeV p–Pb ($1.3 \cdot 10^8$ events, $\mathcal{L}_{\text{int}} = 620 \text{ nb}^{-1}$) collisions were
1003 recorded in 2013 by the ALICE detector [105]. The details of the performance of
1004 the ALICE detector during LHC Run 1 (2009–2013) are presented in Ref. [106].

1005 The analysis uses charged tracks that are reconstructed with the Inner Track-
1006 ing System (ITS) [107] and the Time Projection Chamber (TPC) [108]. These
1007 detectors are located inside the large solenoidal magnet, that provides a homo-
1008 geneous magnetic field of 0.5 T. Tracks within a pseudorapidity range $|\eta| < 0.9$
1009 over the full azimuth can be reconstructed. The ITS is made up of the innermost
1010 Silicon Pixel Detector (SPD), the Silicon Drift Detector (SDD) and the outermost
1011 Silicon Strip Detector (SSD). Each of these consists of two layers. The TPC is a
1012 cylinder filled with gas. Gas is ionised along the path of charged particles. Liber-
1013 ated electrons drift towards the end plates of the cylinder where they are detected.
1014 Combining the information from the ITS and the TPC provides a resolution rang-
1015 ing from 1 to 10 % for charged particles with momenta from 0.15 to 100 GeV/c.
1016 For tracks without the ITS information, the momentum resolution is comparable
1017 to that of ITS+TPC tracks below transverse momentum $p_T = 10 \text{ GeV}/c$, but for
1018 higher momenta the resolution reaches 20 % at $p_T = 50 \text{ GeV}/c$ [106, 109].

1019 Neutral particles used in jet reconstruction are reconstructed by the Electro-
1020 magnetic Calorimeter (EMCAL) [110]. The EMCAL covers an area with a range
1021 of $|\eta| < 0.7$ in pseudorapidity and 100 deg in azimuth. EMCAL is complimented
1022 with the Dijet Calorimeter (DCal) [111] and Photon Spectrometer (PHOS) [112]
1023 that are situated opposite of the EMCAL in azimuth. PHOS covers 70 degrees
1024 in azimuth and $|\eta| < 0.12$. The DCal is technologically identical to EMCal. The
1025 DCal coverage spans over 67 degrees in azimuth, but in pseudorapidity the mid
1026 region is occupied by the PHOS. In between PHOS and DCal active volumes, there
1027 is a gap of 10 cm. DCal is fully back-to-back with EMCal.

1028 The combination of charged tracks with $p_T > 0.15 \text{ GeV}/c$ and neutral particles
1029 with $p_T > 0.30 \text{ GeV}/c$ is used to construct jets.

1030 The V0 detector [113] provides the information for event triggering. The V0
1031 detector consists of two scintillator hodoscopes that are located on either side of
1032 the interaction point along the beam direction. It covers the pseudorapidity region
1033 $-3.7 < \eta < -1.7$ (V0C) and $2.8 < \eta < 5.1$ (V0A). For the 2013 p–Pb collisions
1034 events are required to have signals in both V0A and V0C. This condition is used
1035 later offline to reduce the contamination of the data sample from beam-gas events
1036 by using the timing difference of the signal between the two stations [106].

1037 EMCAL is also used to provide the jet trigger used in triggered datasets. EM-
1038 CAL can be used to trigger on single shower deposits or energy deposits integrated
1039 over a larger area. Latter case is used for jet triggers. The EMCAL trigger defini-

1040 tion in the 2013 p–Pb collisions requires an energy deposit of either 10 GeV for the
1041 low threshold trigger or 20 GeV for the high threshold trigger in a 32×32 patch
1042 size.

1043 In p–Pb collisions the tracks are selected following the hybrid approach [114]
1044 which ensures a uniform distribution of tracks as a function of azimuthal angle
1045 (φ). The momentum resolutions of the two classes of particles are comparable up
1046 to $p_T \approx 10$ GeV/ c , but after that, tracks without ITS requirements have a worse
1047 resolution [106, 109].

1048 3 Experimental Details

1049 3.1 CERN

1050 The European Organization for Nuclear Research (CERN) is the largest particle
1051 physics laboratory in the world. CERN was founded in 1954. In 2019 CERN
1052 consists of 22 member states. Additionally CERN has contacts with a number
1053 of associate member states and various individual institutions. Some 12000 vis-
1054 iting scientists from over 600 institutions in over 70 countries come to CERN for
1055 their research. CERN itself is located near Geneva at the border of France and
1056 Switzerland and itself employs about 2500 people.

1057 The laboratory includes a series of accelerators, which are used to accelerate
1058 the particle beams used. A schematic view of the complex as of 2019 is shown
1059 in Figure ???. In the framework of this thesis the main component is the Large
1060 Hadron Collider (LHC), the largest collider at CERN. LHC will be discussed in
1061 the chapter in more detail. Other accelerators in the series are used to inject the
1062 particle beam into LHC, but they are also used in itself for various experimental
1063 studies.

1064 The second largest accelerator is the super proton synchrotron (SPS). It is final
1065 step before the particle beam is injected into LHC. Commissioned in 1976, it was
1066 the largest accelerator at CERN until the the Large Electron-Positron Collider
1067 (LEP) was finished in 1989. Originally it was used as a proton-antiproton collider
1068 and as such provided the data for the UA1 and UA2 experiments, which resulted in
1069 the discovery of the W and Z bosons. At the moment there are several fixed target
1070 experiments utilising the beam from SPS. These study the structure (COMPASS)
1071 and properties (NA61/SHINE) of hadrons, rare decays of kaons (NA62) and radi-
1072 ation processes in strong electromagnetic fields (NA63). Additionally the AWAKE
1073 and UA9 experiments are used for accelerator research and development.

1074 -PS

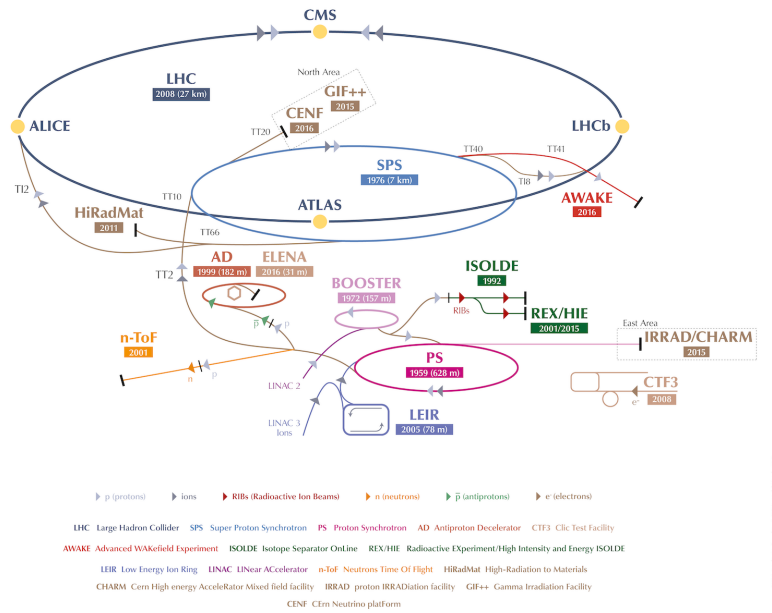


Figure 25: A schematic view of the accelerator complex at CERN. Before particles can be injected into the LHC they require a series of preliminary? acceletarors. Until 2018 protons start their journey in LINAC2 (Linear Accelerator) and continue through the Booster, Proton Synchrotron (PS) and Super Proton Synchrotron (SPS). Between 2019 and 2020 LINAC2 will be replaced by LINAC4 [115]

1075 3.2 Large Hadron Collider

1076 The Large Hadron Collider (LHC) is the largest accelerator at CERN and the
1077 largest particle collider ever built. The LHC is designed to accelerate protons
1078 up to an energy of 8 TeV and lead ions up to 2.76 TeV per nucleon [?]. The design
1079 luminosity of the LHC is $10^{34} \text{ cm}^{-2} \text{ s}^{-1}$. In 20xx it achieved a record peak luminosity
1080 of xxx. For lead beams the design luminosity is xxx. All this is achieved with a
1081 ring of 26.7 km, that consists of 1232 superconducting dipole magnets that keep
1082 particles in orbit.

1083 The particles are accelerated through the use of radio-frequency (RF) cavities.
1084 The RF are build such that the electromagnetic waves become resonant and build
1085 up inside the cavity. Charges passing through the cavity feel the overall force
1086 and are pushed forward along the accelerator. As they consist of electromagnetic
1087 waves, the field in the RF cavity oscillates. Thus particles must enter the cavity at
1088 the correct phase of oscillation to receive a forward push. When timed correctly,
1089 the particles will feel zero accelerating voltage when they have exactly the correct
1090 energy. Particles with higher energies will be decelerated and particles with lower
1091 energies will be accelerated. This focuses particles in distinct bunches. The RF
1092 oscillation frequency at the LHC is 400.8 MHz. Thus RF "buckets" are separated
1093 by 2.5 ns. However only 10 % are actually filled with particles, so the bunch
1094 spacing in the LHC is 25 ns, at a bunch frequency of 40 MHz.

1095 With 7 TeV proton beams the dipole magnets used to bend the beam must
1096 produce a magnetic field of 8.33 T. This can be only achieved through making
1097 the magnets superconducting, which requires cooling them down with helium to a
1098 temperature of 1.9 K. The 1232 dipole magnets make up roughly 2/3 of the LHC
1099 circumference. The remaining part is made up of RF cavities, various sensors and
1100 higher multipole magnets used to keep the beam focused. The most notable of
1101 these are the 392 quadrupole magnets.

1102 The LHC is divided into octants, where each octant has a distinct function.
1103 Octants 2 and 8 are used to inject beam into the LHC from SPS. The 2 beams
1104 are crossed in octants 1,2,5 and 8. The main experiments are built around these
1105 crossing points. Octants 3 and 7 are used for beam cleansing. This is achieved
1106 through collimators that scatter particles with too high momentum or position
1107 offsets off from the beam. The RF cavities used for acceleration are located in
1108 octant 4 and octant 6 is used for dumping the beam. The beam dump is made
1109 up of two iron septum magnets, one for each beam, that will kick the beam away
1110 from machine components into an absorber when needed.

1111 **3.2.1 LHC experiments**

1112 As of 2018 there are four main experiments at the LHC; ALICE, ATLAS, CMS
1113 and LHCb and three smaller ones LHCf, TOTEM and MoEDAL. ALICE will be
1114 covered in section 3.3.

1115 ATLAS (A Toroidal LHC ApparatuS) and CMS (Compact Muon Solenoid) are
1116 the two largest experiments at the LHC. They are both multipurpose experiments
1117 designed to be sensitive to many different possible new physics signals. The biggest
1118 discovery made by these so far is the discovery of the Standard Model Higgs boson,
1119 which was simultaneously published by the experiments in 2012 [?, ?].

1120 The LHCb (LHC beauty) experiment [?] is made for studying the bottom
1121 (beauty) quark. Main physics goals include measurement of the parameters of CP
1122 violation with decays of hadron containing the bottom quark. One of the most
1123 important results published by LHCb is the first measurement of $B_s^0 \rightarrow \mu^+ \mu^-$
1124 decay, which was found to be in line with the Standard Model.

1125 In addition to the four large experiments there are three smaller experiments
1126 along the LHC ring. LHCf (LHC forward) is located at interaction point 1 with
1127 ATLAS. It aims to simulate cosmic rays by the particles thrown forwards by the
1128 collisions in ATLAS.

1129 TOTEM (TOTal Elastic and diffractive cross section Measurement) is located
1130 near the CMS experiment at point 5. This allows it to measure particles emerging
1131 from CMS with small angles. The main goals is to measure the total, elastic and
1132 inelastic cross-sections in pp collisions [?].

1133 The MoEDAL (Monopole and Exotics Detector At the LHC) experiment is
1134 located at the interaction point 8 together with the LHCb experiment. MoEDAL
1135 tries to measure signatures of hypothetical particles with magnetic charge, mag-
1136 netic monopoles.

1137 **3.3 ALICE**

1138 ALICE (A Large Ion Collider Experiment) [116] is the dedicated heavy ion ex-
1139 periment at the LHC. ALICE was designed to cope with the expected very high
1140 multiplicity environment of heavy ion collisions. The design allows measurement
1141 of a large number of low momentum tracks. The different detector subsystems are
1142 optimised to provide high momentum resolution and excellent particle identifica-
1143 tion capabilities over a broad range of momentum.

1144 A schematic view of the ALICE detector in 2018 is presented in Figure 26.
1145 This section will go through the composition of ALICE as it has been during
1146 run 2 between 2014 and 2018. The detector will go through significant upgrades
1147 during Long Shutdown 2 in 2019-2020. As in all the major high energy physics
1148 experiments the positioning of the detectors follows a layered structure. Closest to

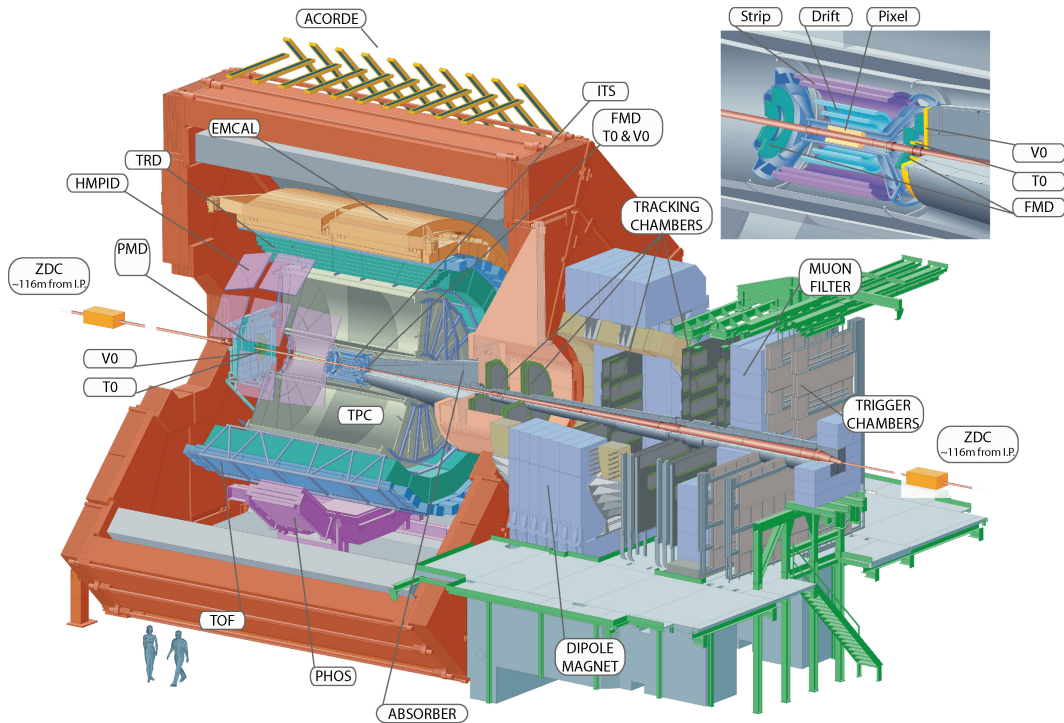


Figure 26: Schematic view of ALICE

the interaction point are the tracking detectors. The main task of these detectors is to locate the position of the primary interaction vertex accurately and to record the tracks of charged particles. To achieve this they need a very good spatial resolution close to the interaction point. Tracking detectors do not significantly alter the tracks of traversing particles. Thus they can be located in the innermost layers.

Calorimeters are designed to stop any particles hitting them and use the absorption to measure the energy of the particles. Thus they must be located behind the tracking detectors. ALICE has two separate calorimeter systems, the electromagnetic calorimeters measure mainly electrons and photons, while the muon detection system measures muons.

3.3.1 Tracking

The main design guideline for the tracking detectors in ALICE was the requirement to have good track separation and high granularity in the high multiplicity environment of heavy ion collisions. Before LHC was built the wildest estimates put the particle density at 8000 charged particles per unit of rapidity [1]. In reality the particle density turned out to be significantly smaller, about 1600 charged

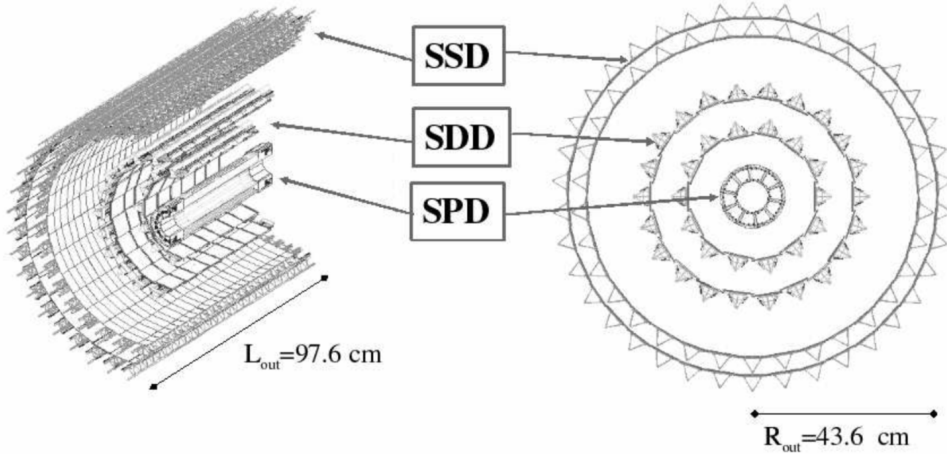


Figure 27: Schematic view of ALICE Inner Tracking System

1166 particles per rapidity unit. []

1167 The main tracking detector in ALICE is the Time Projection Chamber (TPC),
1168 discussed in more detail in section 3.3.2

1169 Between TPC and the beam pipe there is an array of six layers of silicon detec-
1170 tors, called the inner tracking system (ITS) [?]. The main tasks of the ITS are to
1171 locate the primary vertex with a resolution better than $100 \mu\text{m}$, to reconstruct the
1172 secondary vertices from decaying particles, to track and identify particles with mo-
1173 menta below 200 MeV and to compliment the momentum and angle measurements
1174 of TPC. During long shutdown 2 in 2019-2020 the entire ITS will be replaced [?].
1175 As of 2018 the two innermost layers are made of the silicon pixel detector (SPD).
1176 As it's the closest detector to the interaction point it requires are very high spatial
1177 resolution. Thus the choice of pixel technology is natural. In heavy ion collisions
1178 the particle density is around 50 particles per cm^2 .

1179 The next two layers are the silicon drift detector (SDD), which is made out of
1180 homogeneous neutron transmutation doped silicon. It is ionized when a charged
1181 particle goes through the material. The generated charge then drifts to the col-
1182 lection anodes, where it is measured. The maximum drift time in SDD is about 5
1183 μs . This design gives very good multitrack capabilities and provides two out of the
1184 four dE/dx samples in the ITS.

1185 The two remaining layers in the ITS are the silicon strip detector (SSD). The
1186 strips work in a similar way as silicon pixels, but by itself one layer only provides
1187 good resolution in one direction. Combining two crossing grids of strips provides 2
1188 dimensional detection. Each charged particle will hit two intervening strips. The
1189 position of the hit can be deduced from the place where the strips cross each other.

1190 **3.3.2 TPC**

1191 Time projection chamber (TPC) is a cylindrical detector filled with $88m^3$ of
1192 Ne – CO₂ (90/10 %) gas mixture. The gas is contained in a field cage that provides
1193 an uniform electric field of $400V/cm$ along the z-axis (along the beam direction).
1194 Charged particles traversing through the TPC volume will ionise the gas along
1195 their path. This liberates electors that drift towards the end plates of the cylin-
1196 der.

1197 The field cage is separated into two detection volumes by the central high
1198 voltage electrode. Both sides have a drift length of 2.5 m and inner/outer diameters
1199 of 1.2/5 m. This means the central electrode must provide a maximum potential
1200 of 100 kV to achieve the design field magnitude. The maximum time required for
1201 electrons to drift through the chamber is about $90 \mu s$.

1202 When electrons reach the end of the main cylinder they enter the readout
1203 chambers. The readout section of both sides consists of 18 outer chambers and
1204 18 inner chambers. Each of them are made of multiwire proportional chambers
1205 with cathode pad readout. This design is used in many TPCs before. During
1206 Long Shutdown 2 in 2019-2020, the multiwire chambers will be replaced by Gas
1207 Electron Multipliers (GEMs, see section 3.3.3).

1208 The relatively slow drift time of $90 \mu s$ is the limiting factor for the luminosity
1209 ALICE can take. The occupancy of the TPC must be kept in a manageable level.

1210 **3.3.3 TPC upgrade**

1211 During long shutdown 2 in 2019-2020 ALICE will go through significant modifica-
1212 tions. The goal is to be able have continuous readout [?] in heavy ion collisions at
1213 an interaction rate of 50 kHz. I have made a personal contribution to the quality
1214 assurance of the new GEM readout of TPC.

1215 ALICE will add a new Forward Interaction trigger (FIT) to replace the V0 and
1216 T0 detectors.

1217 Additionally the current inner tracking system (ITS) will be completely re-
1218 placed. The current layered structure with three different technologies will be
1219 replaced by an all pixel detector with significantly reduced pixel size. Additionally
1220 the first layer will be brought closer to the beam pipe. The new ITS will have
1221 better tracking efficiency and better impact parameter resolution.

1222 The muon detection will be complimented by the Muon Forward Tracker (MFT) [?].
1223 Based on the same technology as the new ITS, MFT will be placed before the
1224 hadron absorber that sits in front of the existing muon spectrometer. MFT should
1225 significantly increase the signal/background ratio in heavy quark measurements.

1226 Many subdetectors will make small improvements to enhance the readout rate.
1227 The central trigger processor will be replaced and ALICE will introduce a new

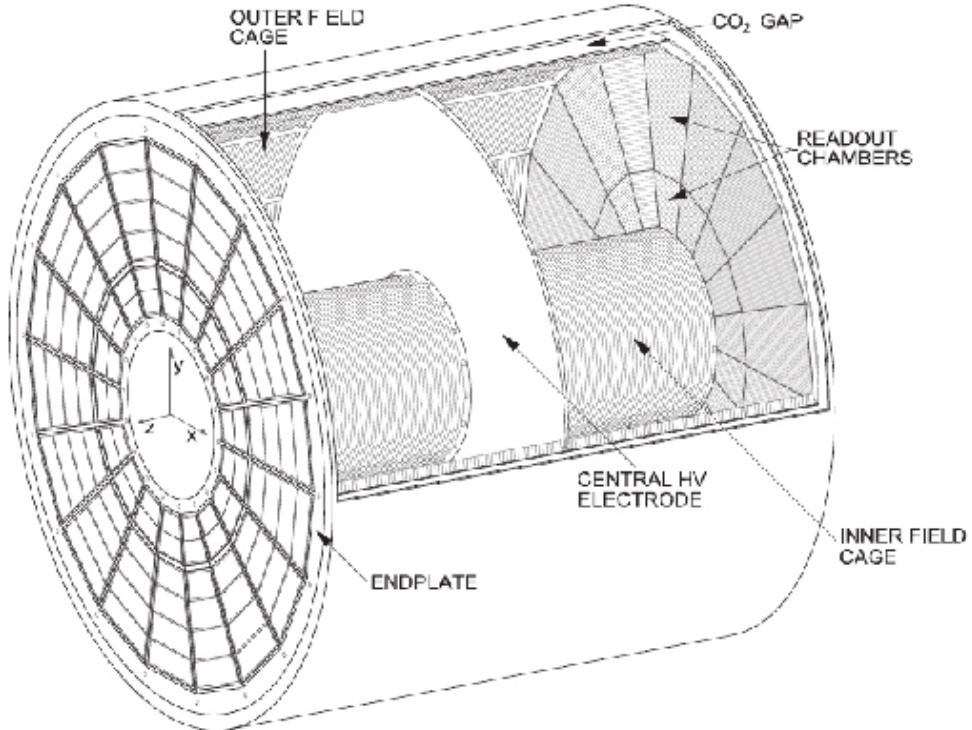


Figure 28: Schematic view of ALICE Time Projection Chamber

1228 framework O^2 that combines both online data acquisition and offline analysis.

1229 The detector restricting the readout the most at the moment is the TPC. The
 1230 current wire chamber based system limits the readout rate to 3.5 kHz. To achieve
 1231 the 50 kHz readout rate goal the wire chambers will be replaced by a Gas Electron
 1232 Multiplier (GEM) based system.

1233 TPC has a total of 36 inner and 36 outer readout chambers. Each of these will
 1234 consist of 4 layers of GEM foils. The inner chambers will only have one foil for
 1235 each layer. The outer chambers are separated into three sections, each with its
 1236 own layer of foils. Each gem foil is made up of a $50\ \mu\text{m}$ thick resistive capton layer,
 1237 coated on both sides by $5\ \mu\text{m}$ thick layers of copper. Each foils is separated into a
 1238 number (20-24) of distinct active areas. The active areas are pierced quite densely,
 1239 they have 50-100 holes in the area of a single mm^2 . The density of holes changes
 1240 from layer to layer. The two middle layers of foils have a larger (double) pitch
 1241 (smaller hole density) while the top and bottom layers have a smaller (normal)
 1242 pitch (larger hole density).

1243 The holes have a conical shape which they acquire during a two step chemical
 1244 etching process.

1245 The working principle of these foils is based on electrodynamics. **elaborate** There
1246 is a large potential difference (140-400 V) applied to the two sides of the foil, which
1247 results in large field in each hole. This acts both as a lens and an amplifier for
1248 the electrons. The amplification happens inside the holes where the field is the
1249 strongest.

1250 The GEMs are designed to minimize ion backflow to allow continuous, ungated
1251 and untriggered readout.

1252 3.3.4 Particle identification

1253 One guiding principle in the design of ALICE was to achieve good particle iden-
1254 tification (PID) over a large part of phases space and for several different particle
1255 types. In ALICE there are several detectors taking part in the identification of
1256 particles.

1257 One of the particle identification detectors is the transition radiation detector
1258 (TRD) [?]. Its main task is identifying electors with momenta larger than 1 GeV.
1259 Transition radiation is produced when highly relativistic particles traverse the
1260 boundary between to media having different dielectric constants. The average
1261 energy of the emitted photon is approximately proportional to the Lorentz factor γ
1262 of the particle, which provides an excellent way of discriminating between electrons
1263 and pion. ALICE TRD is made of a composite layer of foam and fibres. The
1264 emitted photons are then measured in six layers of Xe/CO₂ filled time expansion
1265 wire chambers.

1266 The time of flight (TOF) detector uses a very simple physics principle, i.e.
1267 calculating the velocity of the particle using the time of flight between two points.
1268 Combining this with the momentum of particle, obtained from the tracking de-
1269 tectors, one can calculate the mass of the particle, which identifies particles. The
1270 TOF detector consists of multigap resistive wire chambers. These are stacks of
1271 resistive plates spaced equally. They allow time of flight measurements in large
1272 acceptance with high efficiency and with a resolution better than 100 ps.

1273 The third specific particle identification detector is the high momentum particle
1274 identification (HMPID) detector. The HMPID uses a ring imaging Cherenkov
1275 counter to identify particles with momenta larger than 1 GeV. Particles moving
1276 through a material faster than the speed of light in the material will produce
1277 Cherenkov radiation. The velocity of the particle determines the angle at which
1278 the radiation is emitted. Measuring this angle gives the velocity of the particle.
1279 This can be again used to calculate the mass of the particle, if the momentum is
1280 known. In HMPID the material is a liquid radiator and the photons are measured
1281 with multiwire proportional chambers in conjunction with photocathodes.

1282 In addition to the specific particle identification detectors, the general purpose
1283 tracking detectors can be used for identification through the use of specific energy

1284 loss of charged particles traversing through a medium and the transition radiation
1285 emitted by charged particles when crossing the boundary between two materials.

1286 dE/dx measurements are provided by the last four layers of the ITS detector, i.e.
1287 the SDD and the SSD, thanks to their analog readout. [117] ITS provides particle
1288 identification in the low p_T region, up to 1GeV, and pions reconstructed in the
1289 standalone mode can be identified down to 100 MeV. Similar to ITS the TPC
1290 detector provides specific energy loss measurements. TPC can identify charged
1291 hadrons up to p_T 1 – 2GeV as well as light nuclei, He3 and He4.

1292 3.3.5 Electromagnetic Calorimeter

1293 Calorimeters are designed to measure the energy of particles. Electromagnetic
1294 calorimeters specialise in detecting particles that interact primarily through the
1295 electromagnetic interaction, namely photons and electrons. They are required in
1296 many neutral meson and direct photon analyses. In addition the energy informa-
1297 tion enhance jet measurements.

1298 ALICE has two electromagnetic calorimeters, the photon spectrometer (PHOS) [112]
1299 and the electromagnetic calorimeter (EMCal) [?]. PHOS is a homogeneous calorime-
1300 ter that consists of scintillating PbWO₄ crystals, which generate a bremsstrahlung
1301 shower and produce scintillation light. The energy of the particle determines the
1302 amount of light produced. To improve the charged particle rejection, PHOS in-
1303 cludes a charged particle veto detector (CPV) [?]. PHOS is built to have a very
1304 fine granularity, making it well suited for measuring direct photons and neutral
1305 mesons.

1306 EMCal is a sampling calorimeter. It consists of layers of lead and scinilla-
1307 tor tiles. The lead tiles produce the shower and scintillator tiles the light. The
1308 signal is then read with wavelength shifting fibres. The acceptance of EMCal in
1309 the azimuthal angle is 80 deg < ϕ < 187 deg. During long shutdown 1 in 2013-
1310 2015, EMCal was extended with the di-jet calorimeter (DCal) [111], giving an
1311 additional acceptance region of 260 deg < ϕ < 320 deg. This provides partial
1312 back-to-back coverage. In comparison to PHOS, EMCal has coarser granularity,
1313 but a significantly larger acceptance, making it suitable for jet physics.

1314 3.3.6 Forward detectors

1315 ALICE includes a few small and specialised detectors of importance. The event
1316 time is determined with very good precision (< 25 ns) by the T0 detector [?]. T0
1317 consists of two sets of Cherenkov counters that are mounted around the beam pipe
1318 on both sides of the interaction point. T0 gives the luminosity measurement in
1319 ALICE.

1320 Another small detector in the forward direction is the V0 detector [?]. This

1321 consists of two arrays of segmented scintillator counters located at $-3.7 < \eta <$
1322 -1.7 and $2.8 < \eta < 5.1$. V0 is used as a minimum bias trigger and for rejection
1323 of beam-gas background. Particle multiplicity in the forward direction can be
1324 related to the event centrality. Thus V0 is the main detector used in centrality
1325 determination in PbPb collisions.

1326 The multiplicity measurement of V0 is complimented by the forward multi-
1327 plicity detector (FMD) [?]. FMD includes five rings of silicon strip detectors that
1328 make up the FMD. FMD gives acceptance in the range $-3.4 < \eta < -1.7$ and
1329 $1.7 < \eta < 5.0$.

1330 During long shutdown 2 in 2019-2020, V0 and T0 will be replaced by the Fast
1331 Interaction Trigger (FIT) detector [?]. For historical reasons elements of FIT are
1332 also referred to as V0+ and T0+. FIT will allow centrality, event plane, luminosity
1333 and interaction time determination in the continuous readout mode, that ALICE
1334 will operate in after 2020.

1335 For photon multiplicity measurement ALICE has the photon multiplicity de-
1336 tector (PMD) [?]. PMD uses two planes of gas proportional counters with a
1337 cellular honeycomb structure. PMD gives the multiplicity and spatial distribution
1338 of photons in the region $2.3 < \eta < 3.7$.

1339 On top of the ALICE magnet there is an array of 60 large scintillators called
1340 the ALICE cosmic ray detector (ACORDE) [?]. ACORDE is used as a trigger
1341 for cosmic rays for calibration and alignment.

1342 The only hadronic calorimeters in ALICE are the zero degree calorimeters
1343 (ZDC) [?], which are located next to the beam pipe in the machine tunnel about
1344 116 m from the interaction point. There are two sets of calorimeters. One is
1345 made of tungsten, specialising in measuring neutrons, while the other, made of
1346 brass, is specialised in measuring protons. In heavy ion and especially in proton-
1347 lead collisions, ZDC gives information about the centrality of the event. ZDC is
1348 meant to detect spectators, i.e. parts of the colliding ions that do not take part
1349 in the interaction. If there are more spectators, the collisions is likely to be more
1350 peripheral.

1351 A new detector installed during the long shutdown 1 is the ALICE diffractive
1352 detector (AD) [?]. AD consists of two assemblies, one in each side of the interaction
1353 point, both made of two layers of scintillators. These assemblies are situated about
1354 17 m and 19.5 m away from the interaction points. The pseudorapidity coverage is
1355 $-6.96 < \eta < -4.92$ and $4.78 < \eta < 6.31$. AD greatly enhances ALICE's capability
1356 for diffractive physics measurements that require a large pseudorapidity gap.

1357 3.3.7 Muon spectrometer

1358 Outside the main magnet, ALICE has a spectrometer dedicated to measuring
1359 muons [?]. In heavy ion physics muons are mainly used to measure the production

₁₃₆₀ of the heavy quark resonances J/ψ , Ψ' , Υ , Υ' and Υ'' .

₁₃₆₁ The muon spectrometer consists of three parts, the absorber, the muon tracker
₁₃₆₂ and the muon trigger. The absorber is meant to remove the hadronic background
₁₃₆₃ as efficiently as possible. After the absorber there are ten plates of thin cathode
₁₃₆₄ strip tracking stations with high granularity, the muon tracker. After the muon
₁₃₆₅ tracker there is a layer of iron to filter out any remaining particles, other than
₁₃₆₆ muons. The muon trigger is located behind this layer. The trigger consists of four
₁₃₆₇ resistive plate chambers.

₁₃₆₈ **3.3.8 Trigger**

₁₃₆₉ **4 Event and track selection**

₁₃₇₀ **5 Analysis method**

₁₃₇₁ **5.1 Jet Finding**

₁₃₇₂ The analysis is performed by analysing jet constituents. In each collision event, the
₁₃₇₃ jets are reconstructed using FastJet [118] with the anti- k_T algorithm [119]. Jets for
₁₃₇₄ $R=0.4$ are selected in $|\eta| < 0.25$ to satisfy the fiducial acceptance of the EMCAL. In
₁₃₇₅ jet reconstruction both charged tracks with $p_T > 0.15 \text{ GeV}/c$ and neutral cluster
₁₃₇₆ with $p_T > 0.30 \text{ GeV}/c$ are considered. In the analysis, results are presented in
₁₃₇₇ terms of the jet transverse momentum $p_{T,\text{jet}}$.

₁₃₇₈ **5.1.1 Anti k_T algorithm**

₁₃₇₉ Jets are reconstructed using the anti- k_T algorithm [119]. The algorithm works by
₁₃₈₀ trying to undo the splittings through combining pseudojets/tracks.

$$k_{T,i}^2 = p_{T,i}^{2p}$$

₁₃₈₁ For each pair of protojets the distance measure is calculated as

$$k_{T,(i,j)}^2 = \min(p_{T,i}^{2p}, p_{T,j}^{2p}) \frac{\Delta R_{i,j}^2}{D^2},$$

₁₃₈₂ where

$$R_{i,j} = (\phi_i - \phi_j)^2 + (y_i - y_j)^2$$

₁₃₈₃ If $k_{T,i}$ is the smallest quantity then the protojet is a jet and it is removed
₁₃₈₄ from further consideration. If $k_{T,(i,j)}$ is the smallest quantity the two protojets are
₁₃₈₅ merged. Iterate until no protojets are left.

₁₃₈₆ The choice of the power p in the distance measure depends on the algorithm
₁₃₈₇ used

- ₁₃₈₈ • $p = 1$: k_T algorithm
- ₁₃₈₉ • $p = 0$: Cambridge Aachen algorithm
- ₁₃₉₀ • $p = -1$: anti- k_T algorithm

₁₃₉₁ With the choice $p = -1$ in anti- k_T algorithm, the softest splittings are undone
₁₃₉₂ first.

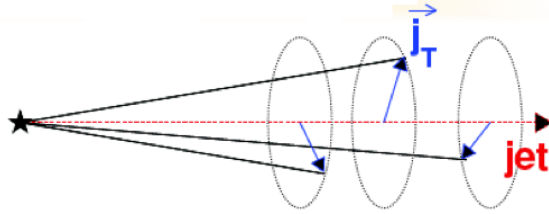


Figure 29: Illustration of \vec{j}_T . The jet fragmentation transverse momentum, \vec{j}_T , is defined as the transverse momentum component of the track momentum, \vec{p}_{track} , with respect to the jet momentum, \vec{p}_{jet} .

1393 5.2 j_T

1394 The jet fragmentation transverse momentum, j_T , is defined as the component of
1395 the constituent particle momentum, \vec{p}_a , transverse to the jet momentum, \vec{p}_{jet} . The
1396 resulting \vec{j}_T is illustrated in Fig. 29. The length of the \vec{j}_T vector is

$$j_T = \frac{|\vec{p}_{\text{jet}} \times \vec{p}_{\text{track}}|}{|\vec{p}_{\text{jet}}|}. \quad (35)$$

1397 It is commonly interpreted as a transverse kick with respect to the initial hard
1398 parton momentum that is given to a fragmenting particle during the fragmentation
1399 process, which is a measure of the momentum spread of the jet fragments [].

1400 The reconstructed jet axis is used for j_T reference. Any charged track within
1401 a fixed cone with radius R is taken as a jet constituent, as opposed to using the
1402 constituent list provided by the jet algorithm. Anti- k_T produces jets that are
1403 very circular in shape. Thus this doesn't change the constituent list considerably.
1404 Neutral tracks are used only in jet reconstruction.

1405 5.2.1 1 over j_T

j_T results are shown as

$$\frac{1}{j_T} \frac{dN}{dj_T}$$

1406 distributions. The logic behind this is that j_T is inherently a two-dimensional
1407 observable, comprised of j_{Tx} and j_{Ty} components. So the actual physical observable
1408 would be

$$\frac{d^2N}{dj_{Tx} dj_{Ty}}$$

1409 Changing into polar coordinates with $j_{\text{Tr}} = j_{\text{T}}$ and θ gives

$$\frac{d^2N}{j_{\text{T}} dj_{\text{T}} d\theta},$$

1410 where j_{T} over the azimuth θ should stay constant and it can be integrated over
1411 giving

$$\frac{1}{2\pi} \frac{dN}{j_{\text{T}} dj_{\text{T}}}.$$

1412 5.3 Unfolding

1413 Extend unfolding

1414 The resulting j_{T} distributions are corrected for the detector inefficiency using
1415 the unfolding method. The response matrix for the unfolding is obtained from a
1416 PYTHIA [120] simulation.

Measured distributions are affected by two main factors; Limited acceptance -
The probability to observe a given event is less than one and limited resolution -
Quantity x cannot be determined exactly, but there is a measurement error. True
 $f(x)$ and measured $g(y)$ distributions are connected by a convolution integral.
Including statistical fluctuations this becomes

$$\hat{g}(y) = \int_a^b A(y, x) f(x) dx + \epsilon(y),$$

where A is the detector response obtained by Monte Carlo simulations and $\epsilon(y)$
is the term coming from statistical fluctuations. If x and y are discrete variables
we have

$$\hat{g}_i = \sum_{j=1}^m A_{ij} f_j + \epsilon_i,$$

Or in matrix form

$$\hat{g} = Af + \epsilon$$

If the only detector effect is limited acceptance, A is a diagonal matrix. In a
general discrete case the (naive) solution is obtained by the inverse matrix

$$\hat{f} = A^{-1} \hat{g}$$

1417 However this usually leads to oscillating solutions and determining the inverse
1418 matrix can be difficult.

1419 Two common methods to perform this inversion are Bayesian and SVD unfold-
1420 ing methods. Often the solution requires some additional *a priori*. For example
1421 the solution should be smooth in most cases.

¹⁴²² **5.3.1 Bayesian unfolding**

The bayesian (iterative) method is based on the Bayes formula [].

$$P(C_i|E_j) = \frac{P(E_j|C_i) P_0(C_i)}{\sum_{l=1}^{n_C} P(E_j|C_l) P_0(C_l)},$$

¹⁴²³ i.e. Probability of Cause ("truth") C_i given Effect ("observed") E_j is proportional to the probability of observing E_j given C_i (response matrix) and the truth distribution $P_0(C_i)$.

At first P_0 is given some starting distribution, either a uniform distribution or some guess of the final distribution. Taking into account the inefficiency this gives

$$\hat{n}(C_i) = \frac{1}{\epsilon_i} \sum_{j=1}^{n_E} n(E_j) P(C_i|E_j),$$

where

$$P(C_i|E_j) = \frac{P(E_j|C_i) P_0(C_i)}{\sum_{l=1}^{n_C} P(E_j|C_l) P_0(C_l)},$$

and

$$\hat{n}(C_i) = \frac{1}{\epsilon_i} \sum_{j=1}^{n_E} n(E_j) P(C_i|E_j).$$

First $P(C_i|E_j)$ is calculated with the uniform distribution or best guess of the shape of the distribution. This is then used to calculate the new distribution $\hat{P}(C_i)$

$$\hat{N}_{true} = \sum_{i=1}^{n_C} \hat{n}(C_i), \quad \hat{P}(C_i) = P(C_i|n(E)) = \frac{\hat{n}(C_i)}{\hat{N}_{true}}$$

¹⁴²⁶ P_0 is then replaced with \hat{P} and the procedure is repeated until an acceptable ¹⁴²⁷ solution is found.

¹⁴²⁸ **5.3.2 Toy Monte Carlo**

remove? A toy Monte Carlo simulation was performed to see the performance in an ideal case. Sample jet p_T values from observed p_T distribution. Starting from this p_T start creating tracks with

$$p_{\text{track}} = z_{\text{track}} p_{T,\text{jet}}$$

¹⁴²⁹ where z_{track} is sampled from the observed z distribution. All tracks below 0.15GeV ¹⁴³⁰ are discarded. Sampling is continued until the sum of the track transverse momenta

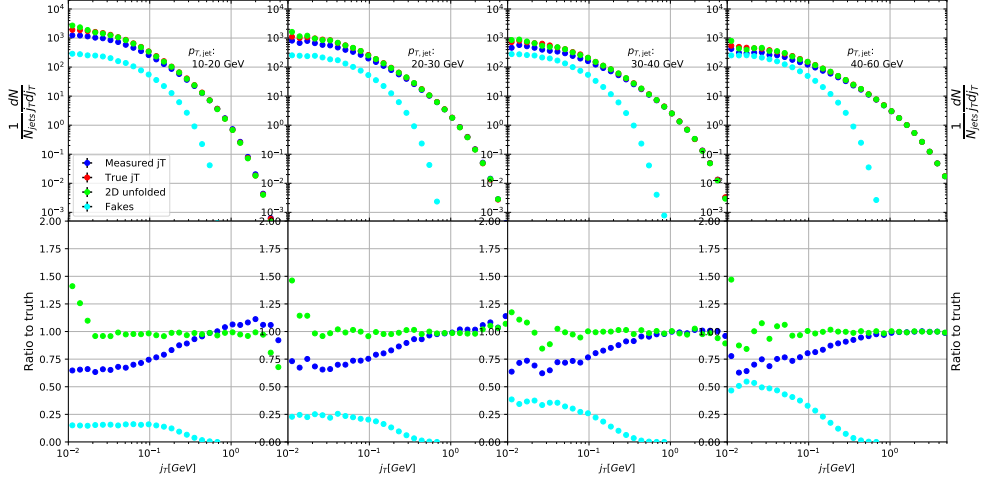


Figure 30: Results from unfolding in Toy Monte Carlo

1431 exceeds the jet transverse momentum. Jet is then defined as the sum of the track
 1432 momenta.

1433 Simultaneously a p_T dependant observation efficiency is applied to the tracks
 1434 and a separate observed jet is calculated using only the observed tracks. Addi-
 1435 tionally a set of fake tracks is added to the observed jet. Tracks are always either
 1436 observed or not at the true momentum. No smearing is added to the observed
 1437 momentum.

Afterwards the tracks are looped over for j_T calculation. For observed tracks we calculate j_T with respect to both the true jet axis and the observed jet. 2D Response matrix is filled with

$$(j_{T,\text{obs}}, p_{T,\text{jet},\text{obs}}, j_{T,\text{true}}, p_{T,\text{jet},\text{true}})$$

1438 In practice this is done with a set of 3D histograms, where $p_{T,\text{jet},\text{true}}$ determines
 1439 the histogram index and the remaining three values the bin in the 3D histogram.

1440 After creating the response matrices, an identical procedure is carried out the
 1441 create testing data. Now instead of filling response matrices, 2D histograms are
 1442 filled with $(j_{T,\text{obs}}, p_{T,\text{jet},\text{obs}})$ and $(j_{T,\text{true}}, p_{T,\text{jet},\text{true}})$

1443 The observed distributions are unfolded using RooUnfold's 2D Bayesian (iter-
 1444 ative) algorithm. Results are shown in figure 30.

1445 5.3.3 Pythia Response matrices

1446 Response matrices are filled through correlation between MC detector and particle
 1447 level jets and tracks.

Table 2: j_T and p_T ranges used in unfolding. The same ranges are used for detector and truth level.

	j_T	$p_{T\text{jet}}$
Min	0.01	5
Max	20	500

The ranges of both j_T and $p_{T\text{jet}}$ extend the ranges in end results. These are shown in Tab. 2. The ranges are the same in detector and particle level.

When calculating j_T for MC particles the code checks whether a corresponding detector level track exists and if that track had a j_T value. Additionally check for detector level tracks that don't have corresponding particle level track or that track does not have j_T value.

Possible cases:

- We find a corresponding track with a j_T value, response matrix is filled normally with $(j_T^{obs}, p_T^{obs}, j_T^{true}, p_T^{true})$
- We don't find a corresponding track. Record (j_T^{true}, p_T^{true}) as a miss
- We find a corresponding track, but it didn't have j_T value. Most likely because it was not part of a jet. Similary record (j_T^{true}, p_T^{true}) as a miss
- For detector level tracks with no correspondence in particle level set record cord (j_T^{obs}, p_T^{obs}) as a fake

5.3.4 2D response matrices

In the analysis code the response matrix is made of an array of 3 dimensional histograms, with $(j_{T,obs}, p_{T,obs}, j_{T,true})$ as axes. The histogram index gives the $p_{T,true}$ value.

5.3.5 Unfolding algorithm

As a primary method unfolding is performed with an iterative (bayesian) algorithm using the RooUnfold [121] package. The number of iterations used is 4.

5.3.6 Effect of number of iterations

The iterative unfolding algorithm permits the change of number of iterations. The unfolding was carried out using different numbers of iterations. The results from these different cases are shown in Fig. 31. The results are compared to the default unfolding algorithm with 4 iterations. The difference in results between the different cases is mostly less than 2.5%.

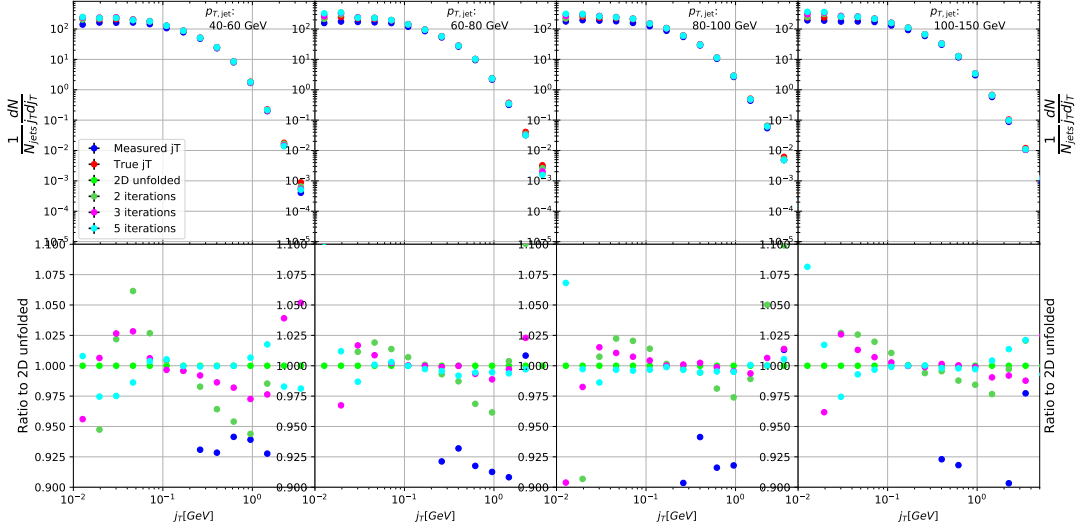


Figure 31: Unfolding with different number of iterations

1475 5.3.7 Effect of different prior

1476 The iterative algorithm requires a prior estimate of the shape of the distribution.
 1477 As a default prior the truth (particle level) distribution is used. To test the effect
 1478 of changing the prior we instead use the unfolded j_T distribution as prior. The
 1479 results are compared to the unfolding algorithm with the default prior. This is
 1480 shown in Fig. 32 The difference in results between the different cases is mostly less
 1481 than 2.5%.

1482 5.3.8 Effect of p_T truncation

1483 5.3.9 Unfolding closure test

1484 Pythia set is divided in 2 halves. First is used to fill the response matrices, as well
 1485 as record missed and fake tracks. Second half is used to test the effectiveness of
 1486 the unfolding method. Jet p_T distributions are shown in figure 34a and response
 1487 matrix are shown in figure 34b.

1488 Response matrices within single jet p_T bins are shown in figure 35. Results
 1489 from the closure test are shown in figure 36. In the lowest jet p_T bins unfolding
 1490 fails to recover the true distribution. The lowest jet p_T bins are dominated by
 1491 combinatorial jets and thus the true detector response is likely not retrieved.

1492 Above jet p_T 30-40 GeV the distribution is recovered well in the mid j_T region.
 1493 At $j_T < 0.1$ there is clear discrepancy. The final results are shown only for $j_T > 0.1$.
 1494 Additionally there is some discrepancy at very high j_T . This is taken into account

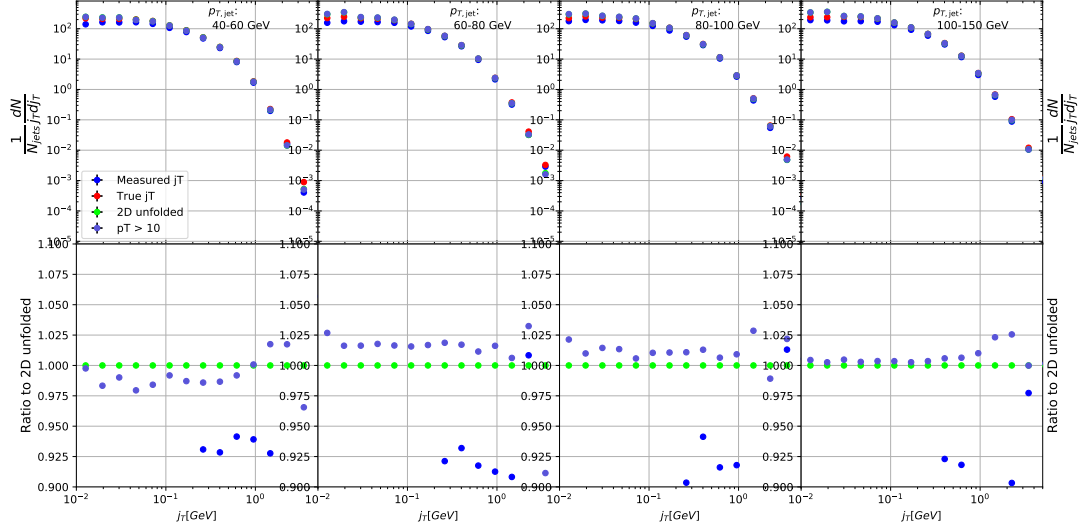


Figure 32: Effect of changing minimum jet p_T used in unfolding from 5 to 10 GeV

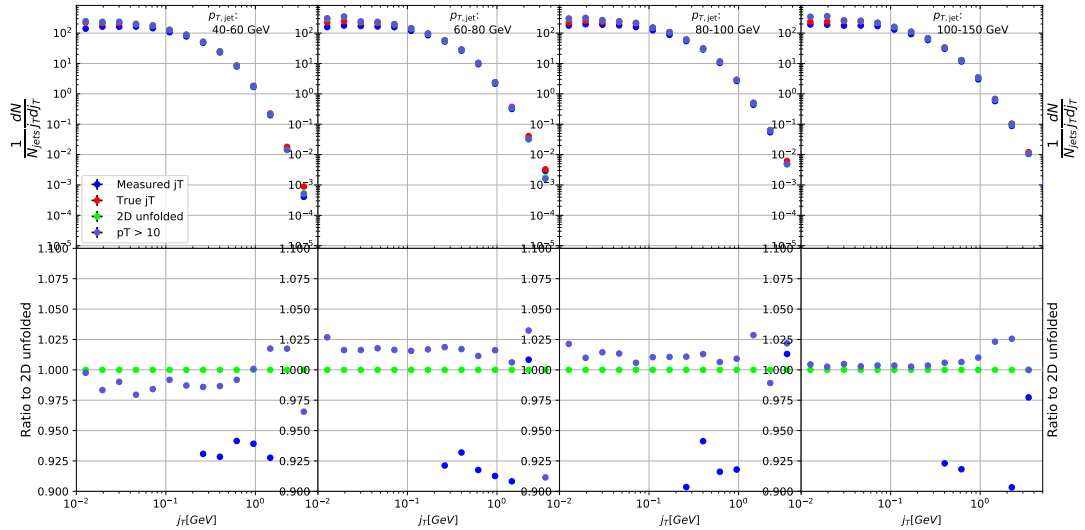
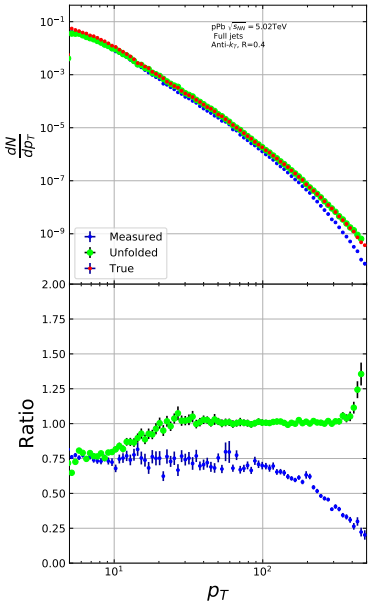
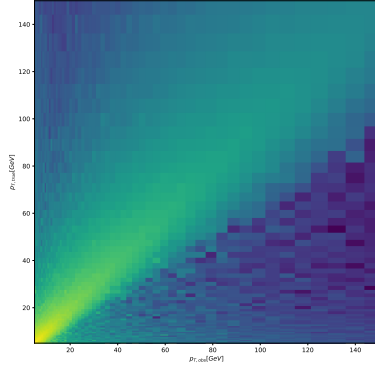


Figure 33: Effect of changing minimum jet p_T used in unfolding from 5 to 10 GeV



(a) Unfolded jet p_T distribution in Pythia
 closure test



(b) Jet p_T response matrix from unfolding
 closure test

1495 in the unfolding systematics. (TODO: Show this)

1496 5.4 Background

1497 When calculating j_T distribution for jet constituents there is a contribution from
 1498 underlying event (UE), i.e. tracks that just happen to be close to the jet axis.
 1499 To find the signal coming from the actual jet we need to subtract the background
 1500 (UE) contribution. On a jet-by-jet basis this is impossible, so we try to estimate
 1501 the background by looking at regions of the detector where there are no tracks
 1502 from jets, but only uncorrelated tracks from the underlying event.

1503 The underlying event is estimated by looking at an imaginary jet cone perpen-
 1504 dicular to the observed jet axis ($\frac{\pi}{2}$ Rotation in ϕ). j_T is calculated for any tracks
 1505 found within this cone. The vector sum of the individual track momentum and
 1506 the imaginary jet axis is used as reference for j_T . The background obtained in
 1507 this manner is subtracted from the unfolded inclusive j_T distribution, which gives
 1508 the resulting signal distribution. To make sure there is no jet contribution in the
 1509 background, any events with jets inside the perpendicular cone are not used for
 1510 background estimation.

1511 We have two methods for background estimation. In the first we look at the
 1512 direction perpendicular to the jet. This is assumed to be the region least likely to
 1513 contain jet contributions.

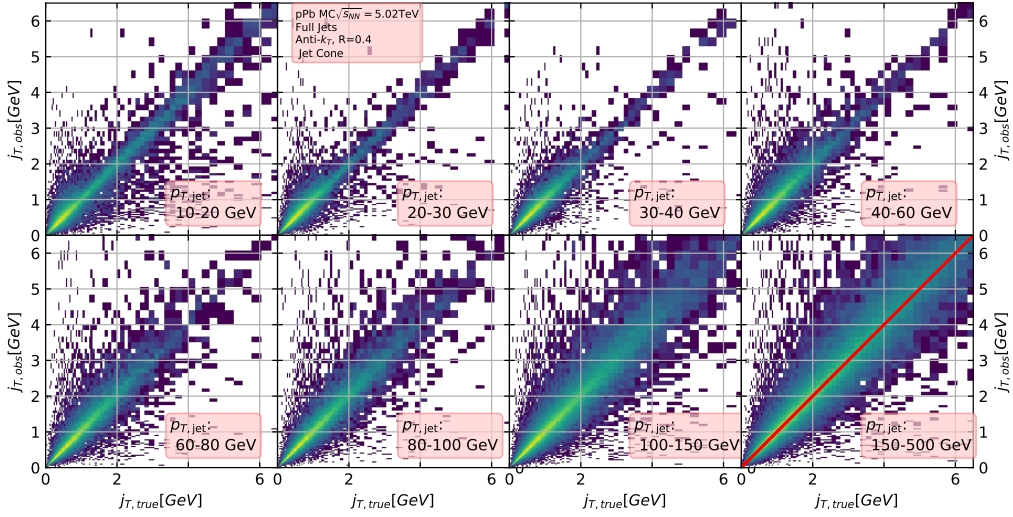


Figure 35: j_T Response matrices in single jet p_T bins

1514 In the second method we randomly assign the tracks of event new ϕ and η
 1515 values. The result is guaranteed to be uncorrelated.

1516 5.4.1 Perpendicular cone background

1517 After calculating the j_T values for tracks in the jet, we rotate the jet axis by $\frac{\pi}{2}$
 1518 in positive ϕ direction. We check that there are no other jets closer than $2R$ to
 1519 the rotated axis. If there are then background calculation is skipped for this jet.
 1520 Probability of this happening is 1-2% depending on the jet p_T bin.

1521 If we don't find other jets in the vicinity we move on to estimate the background.
 1522 We find all tracks within a cone of radius R around the rotated axis and calculate
 1523 j_T of these tracks with respect to the rotated axis. Auto-correlations are added to
 1524 match effect to jet. (see 5.4.3)

1525 5.4.2 Random background

1526 In the random background method we look at all tracks in the event, except for
 1527 tracks close to jets found by the jet algorithm. We randomly assign new η and ϕ
 1528 values to all tracks using uniform distribution. $|\eta| < 1.0$ p_T values are kept the
 1529 same. To increase statistics there is a possibility to create a number of random
 1530 tracks for each actual track. In the analysis we currently do this 10 times for each
 1531 track. Again the track p_T value is kept the same.

1532 We create a random jet cone from uniform η and ϕ distributions. Here $|\eta| <$
 1533 0.25. Now we calculate j_T of the random tracks with respect to the random cone

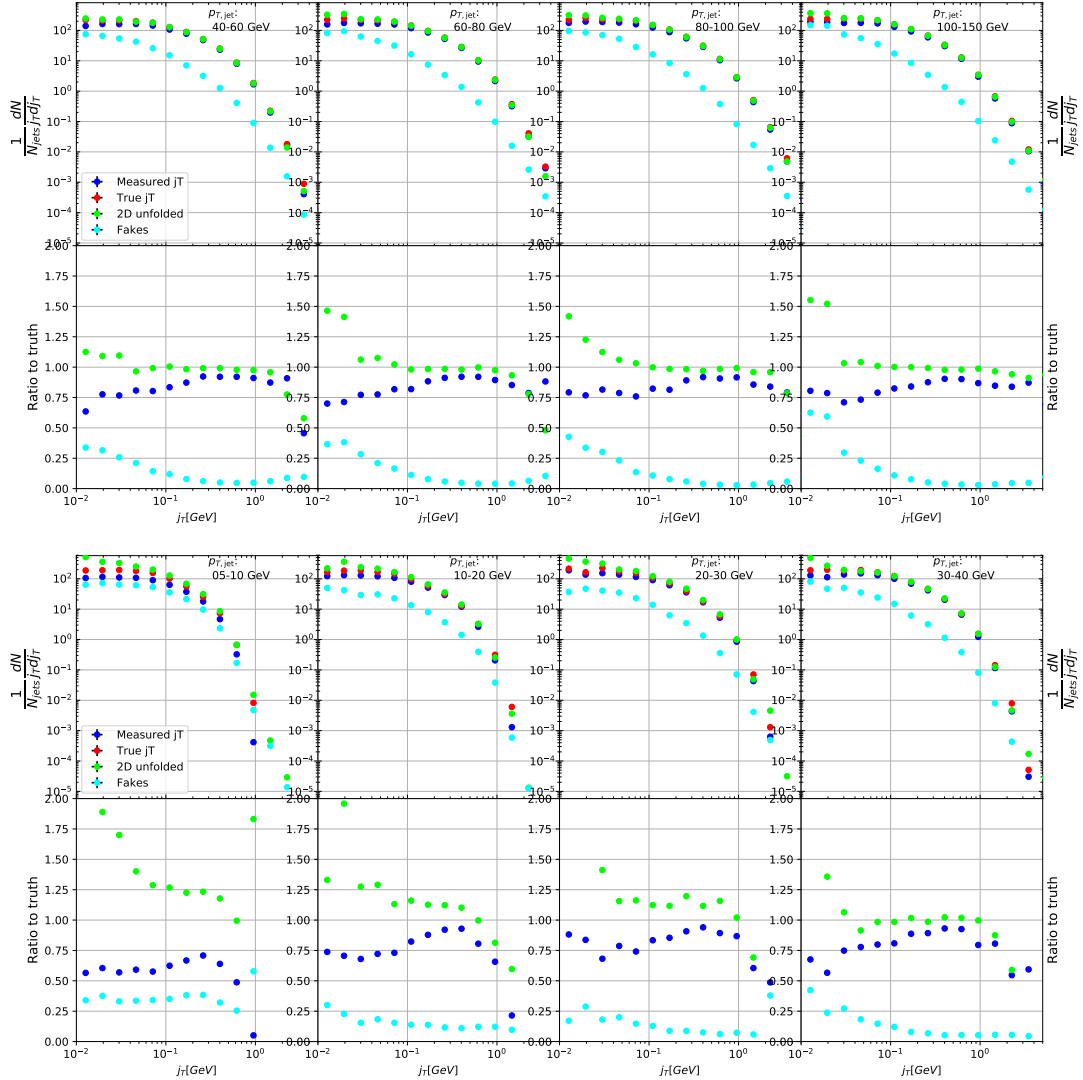
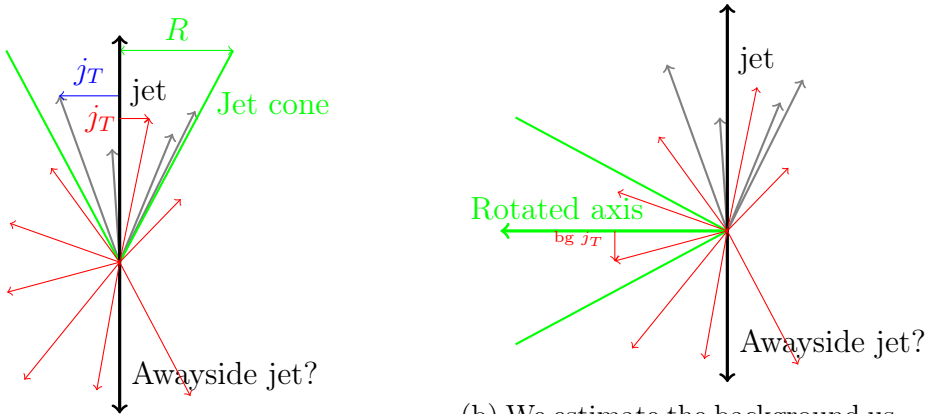
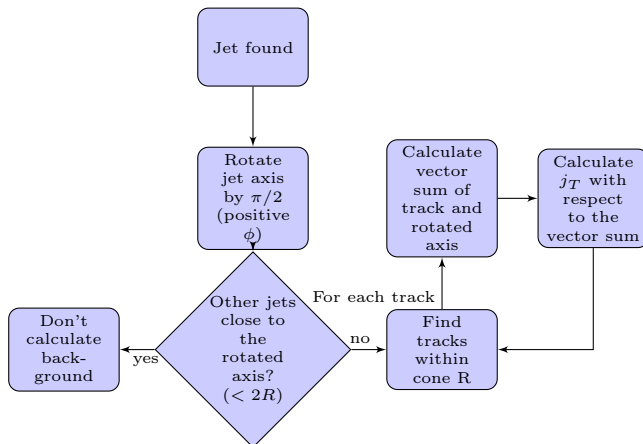


Figure 36: Pythia closure test results. Fake tracks include also tracks that do exist in the true dataset, but for one reason or another were not given j_T values. j_T is only calculated for tracks that are associated with jets



(a) Red is underlying event while gray tracks represent the signal
(b) We estimate the background using a cone where the axis is perpendicular to the jet axis



1534 axis. Auto-correlations are added before calculating j_T (see 5.4.3)

1535 5.4.3 Auto-correlations

1536 Jet axis is simply a vector sum of all its constituents. Thus having an additional
1537 track in the jet from the underlying event moves the jet axis towards this track.
1538 Since the axis is now closer to the track, it has a smaller j_T value. Assuming a 1
1539 GeV background track at the edge of a $R = 0.4$ the j_T value would be 0.4GeV.
1540 If this is added to a 5GeV jet, the j_T value becomes 0.33GeV. In a 50GeV jet it
1541 would be 0.39GeV. This is a region where the inclusive j_T distribution is domi-
1542 nated by background. The distribution is also steeply falling. Overestimating the
1543 background can lead to a situation where the background estimation exceeds the
1544 inclusive distribution.

1545 To take this effect into account we can't use a fixed axis for background, but
1546 it has to behave like a jet would when additional tracks are added. Thus before
1547 calculating j_T values we make a vector sum of the track and the axis used for back-
1548 ground, which is either the perpendicular cone axis or the random axis depending
1549 on the background method. In each case the momentum of this background axis
1550 is assumed to be the same as the jet which initiated the background estimation.

1551 In pPb data there is on average about one underlying event track in a $R = 0.4$
1552 cone.

1553 Extend Background, Perp. cone vs. Random

1554 5.5 Fitting

1555 The resulting signal distribution are fitted with a 2 component function shown in
1556 Eq. 36. Gaussian distribution is used for low j_T and an inverse gamma function is
1557 used for high j_T . The gaussian is taken to have the center at $j_T = 0$. In total this
1558 gives 5 parameters.

$$\frac{1}{N_{\text{jets}} j_T \text{d}j_T} \frac{\text{d}N}{\text{d}j_T} = \frac{B_2}{B_1 \sqrt{2\pi}} e^{-\frac{j_T^2}{2B_1^2}} + \frac{B_3 B_5^{B_4}}{\Gamma(B_4)} \frac{e^{-\frac{B_5}{j_T}}}{j_T^{B_4+1}} \quad (36)$$

1559 To achieve stable results the fitting is performed in two steps. First each
1560 component is fitted separately. Gaussian component is fitted to the low end in j_T .
1561 Inverse gamma component is fitted to j_T above 1 GeV/c. After getting the results
1562 from the individual fits they are combined into a single function with initial values
1563 from the individual results and an additional fit is performed. Fitting only the
1564 gaussian component to the entire distribution produces approximately the same
1565 result as the gaussian component in the two-component model.

1566 After getting the fit function $\sqrt{\langle j_T^2 \rangle}$ (RMS) and yield values are extracted
1567 separately from each component. The narrow component RMS is

$$\sqrt{\langle j_T^2 \rangle} = \sqrt{2}B_1,$$

1568 and the wide component RMS value is calculated as

$$\sqrt{\langle j_T^2 \rangle} = \frac{B_5}{\sqrt{(B_4 - 2)(B_4 - 3)}},$$

1569 where it is required that $B_4 > 3$.

1570 6 Systematic uncertainties

1571 Extend Systematics

1572 The systematic uncertainties in this analysis come from the background esti-
1573 mation, the unfolding procedure and the cuts used to select the tracks. Tracking
1574 uncertainties are estimated from variations of the track selection cuts defined in
1575 Sec. 2. The resulting variations in RMS are shown in Table 4. The uncertainties
1576 from unfolding and background subtraction are of the same magnitude.

1577 The systematics in background estimation were studied using an alternative
1578 method to extract the background, mainly the random background method. The
1579 resulting uncertainty is below 5% for the wide component RMS and below 9% for
1580 the narrow component RMS.

1581 The systematic uncertainty that arises from the unfolding procedure is esti-
1582 mated by performing the unfolding with two separate methods. Data corrected
1583 by the iterative unfolding method are used as the results and the SVD unfolding
1584 method is employed to estimate the uncertainty. In a PYTHIA closure test the
1585 true distribution was in general found to be between the unfolded distributions
1586 from the iterative and SVD method. The difference between the methods when
1587 unfolding data should give a reasonable estimate of the unfolding uncertainty. The
1588 resulting uncertainty is below 8% for both wide and narrow component RMS.

1589 The different source of the systematic uncertainty are considered as uncorre-
1590 lated and the values of each source are summed in quadrature. The resulting
1591 uncertainty is 9 % for the wide component RMS and 12 % for the narrow compo-
1592 nent RMS.

1593 There is no tracking and no unfolding uncertainty in the Monte Carlo simula-
1594 tions.

Table 3: Summary of systematic errors

Systematic	Wide RMS	Narrow RMS
Background	5 %	9 %
Unfolding	8 %	8 %
Tracking	? %	? %
Total	9 %	12%

₁₅₉₅ 7 TPC Upgrade?

1596 8 Systematic errors

1597 8.1 Background subtraction

1598 Fits are performed on both perpendicular cone and random background signals.
 1599 Difference between them is taken as the systematic error. The fits for individual bins from the random background method are shown in figure 40. Resulting
 1600 differences between the methods for different components are shown in figure 39.
 1601

1602 8.2 Unfolding

1603 Unfolding is performed using both SVD and Bayesian unfolding. Difference between
 1604 the methods is taken as the systematic error. Since SVD unfolding does not have a 2 dimensional options, the unfolding is done bin by bin. The resulting
 1605 distributions after SVD unfolding and background subtraction with the perpendicular
 1606 cone method are shown in fig ???. Resulting differences between the methods for different
 1607 components are shown in figure 41.
 1608

1609 8.3 Tracking

1610 8.4 Combining systematics

1611 Resulting systematic errors are shown in table 4. Systematic errors are combined
 1612 bin-by-bin in quadrature to get the total systematic errors.

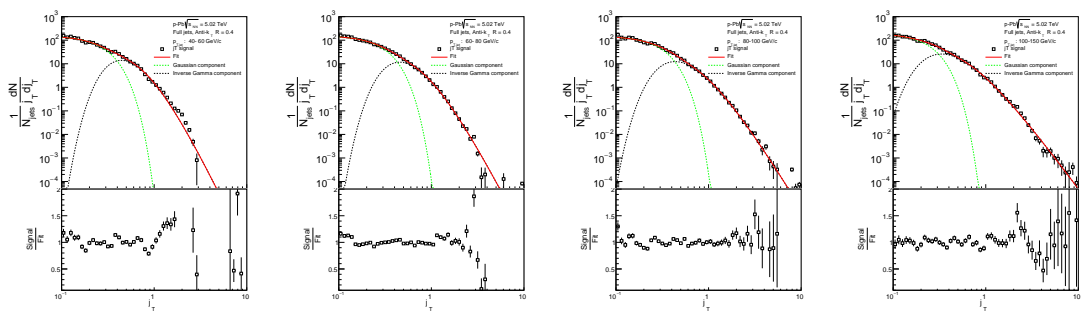


Figure 38: j_T signal with random background subtraction fits in different jet p_T bins

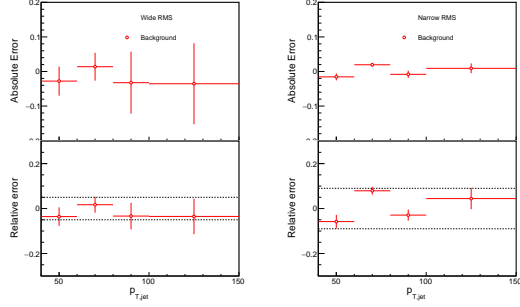


Figure 39: Differences between perpendicular cone and random background subtraction in the resulting RMS values.

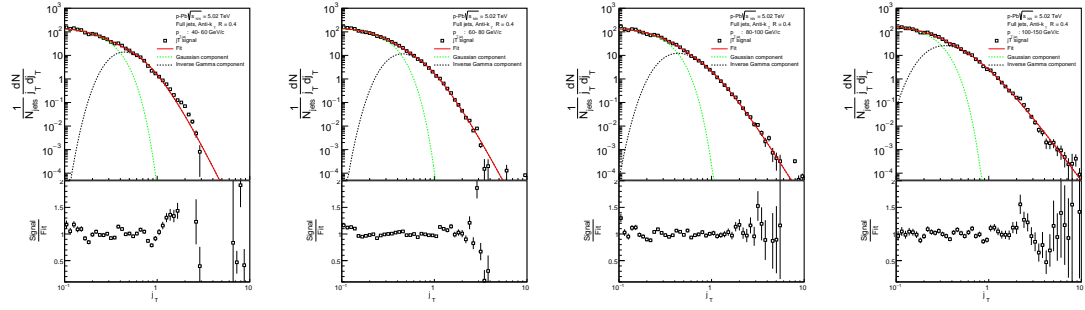


Figure 40: j_T signal with random background subtraction fits in different jet p_T bins

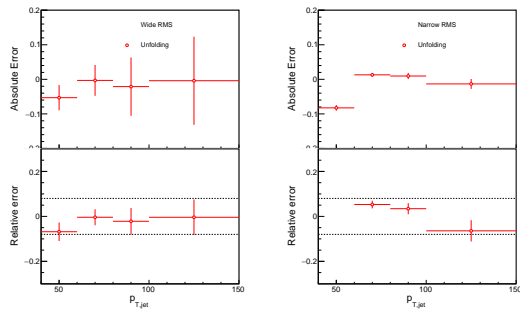


Figure 41: Differences between Bayesian and SVD unfolding in the resulting RMS values

Table 4: Summary of systematic errors

Systematic	Wide RMS	Narrow RMS
Background	5 %	9 %
Unfolding	8 %	8 %
Total	9 %	12%

1613 9 Results

1614 9.1 statistics

1615 Number of jets in different datasets and with different jet finders is shown in table
 1616 5. Background statistics for number of background cones (number of jets minus
 1617 number of discarded cones) are shown in table 6. Ratio of background cones to
 1618 number of jets is shown in table 7. The likelihood of having to discard a jet from
 background calculation is about 1-2%.

Table 5: Number of found jets by dataset and jet p_T bin

Jet p_T	5-10	10-20	20-30	30-40	40-60	60-80	80-100	100-150	150-500
MBFullR04	4969393	621753	32552	5584	1974	310	90	37	5
MBFullR05	4750567	826598	42373	5543	1719	276	73	29	3
MBChargedR04	3144538	673419	37783	4121	1009	148	36	12	1
MBChargedR05	2229247	175763	7961	1270	410	61	12	3	
TriggeredFullR04	187557	115927	78138	51317	39262	8621	2409	1167	171
TriggeredFullR05	99991	77147	48612	34325	28104	6342	1726	794	104
TriggeredChargedR04	37411	29945	18186	13148	11142	2517	675	326	44
TriggeredChargedR05	433155	175031	54789	19776	10626	1983	457	194	15

1619

Table 6: Number of background cones used in perpendicular cone background calculation

Jet p_T	5-10	10-20	20-30	30-40	40-60	60-80	80-100	100-150	150-500
MBFullR04	4947583	617895	32357	5548	1965	310	90	37	5
MBFullR05	4710217	815461	41584	5439	1698	273	73	29	3
MBChargedR04	3117495	661106	36739	4014	988	144	36	12	1
MBChargedR05	2195286	172919	7860	1249	406	61	12	3	
TriggeredFullR04	186574	115376	77949	51216	39196	8603	2405	1167	171
TriggeredFullR05	99102	76462	48320	34216	28038	6334	1722	794	103
TriggeredChargedR04	37160	29543	17988	13099	11129	2515	675	326	44
TriggeredChargedR05	313421	140707	45229	16243	8709	1604	377	154	14

Table 7: Ratio of background cone number to number of jets

MBFullR04	99.56%	99.38%	99.40%	99.36%	99.54%	100.00%	100.00%	100.00%	100.00%
MBFullR05	99.15%	98.65%	98.14%	98.12%	98.78%	98.91%	100.00%	100.00%	100.00%
MBChargedR04	99.14%	98.17%	97.24%	97.40%	97.92%	97.30%	100.00%	100.00%	100.00%
MBChargedR05	98.48%	98.38%	98.73%	98.35%	99.02%	100.00%	100.00%	100.00%	100.00%
TriggeredFullR04	99.48%	99.52%	99.76%	99.80%	99.83%	99.79%	99.83%	100.00%	100.00%
TriggeredFullR05	99.11%	99.11%	99.40%	99.68%	99.77%	99.87%	99.77%	100.00%	99.04%
TriggeredChargedR04	99.33%	98.66%	98.91%	99.63%	99.88%	99.92%	100.00%	100.00%	100.00%
TriggeredChargedR05	72.36%	80.39%	82.55%	82.13%	81.96%	80.89%	82.49%	79.38%	93.33%

1620 9.2 Data

1621 9.3 Inclusive results

1622 Results in figure 42

1623 As outlined in Section ?? the inclusive j_T distributions and corresponding
 1624 backgrounds are obtained for different jet p_T bins starting from $10 \text{ GeV} < p_{T\text{jet}} <$

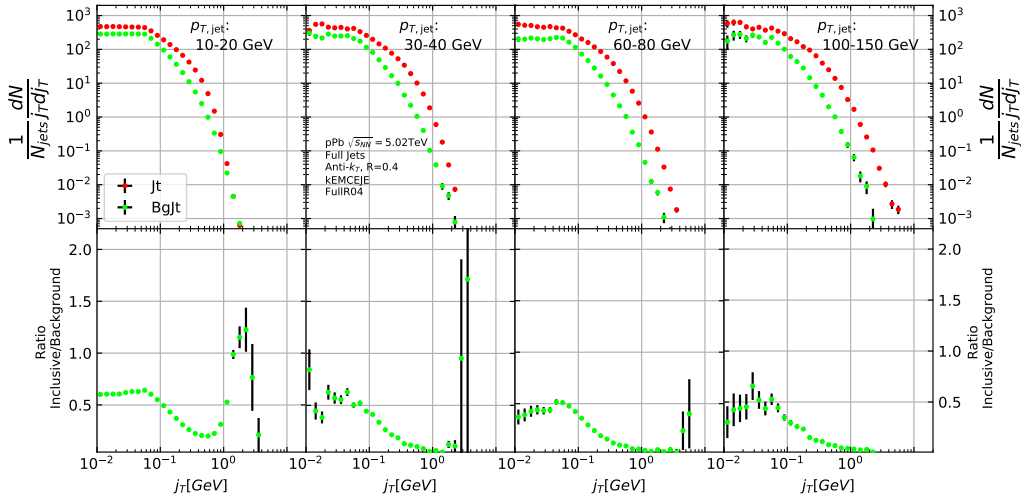


Figure 42: Inclusive j_T with background

1625 20 GeV. Later the lowest p_T bins are omitted because of problems in unfolding
1626 and fitting. The results are shown in Fig. 42. The background distribution the
1627 figure is obtained by the perpendicular cone method.

1628 9.4 Background

1629 Comparison between perpendicular cone and random background in figure 43. The
1630 advantage of the random background method is the added amount of statistics as
1631 the procedure can be repeated several times for each event. However, it seems that,
1632 especially in the highest $p_{T,jet}$ bins there is some jet contribution left at the high
1633 end. One should note that the results from perpendicular cone background show no
1634 observable change between $p_{T,jet}$ bins. It is a good indication that the background
1635 is actually dominated by the underlying event over the entire j_T region.

1636 9.5 Comparison between A and C side

1637 In 2013 there were some issues with tracking. To rule out effects on j_T distributions
1638 a study was performed comparing j_T distributions between A and C side. No
1639 systematic differences were observed.

1640 9.6 Subtracted signal

1641 Results in figure 45. Comparison between signals with different backgrounds in
1642 figure 46

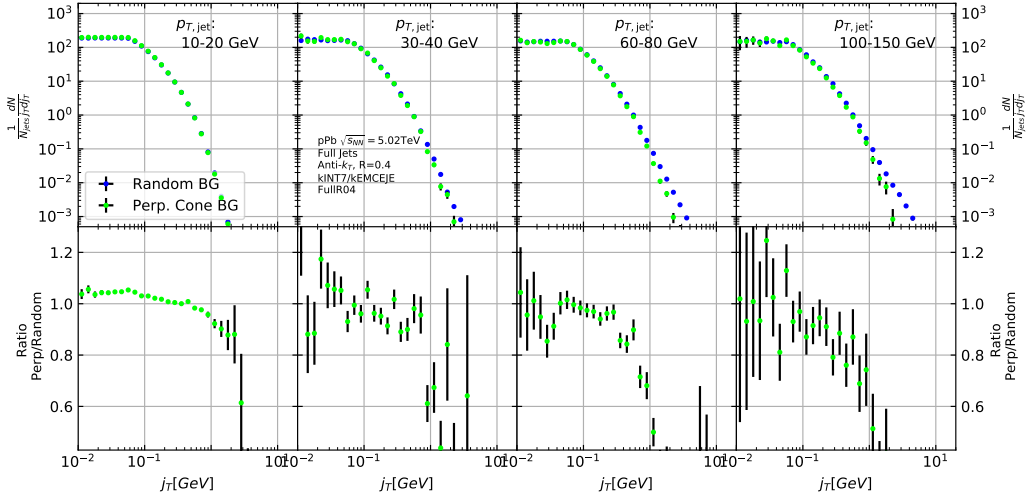


Figure 43: j_T background with two different methods

1643 9.7 Fitting

1644 Fits of j_T distributions in different jet p_T bins with $p_T > 40\text{GeV}$ are shown in figure
 1645 47. Additional jet p_T bins are shown in appendix ???. In lowest jet p_T bins the
 1646 jets are mainly combinatorial which makes background subtraction and unfolding
 1647 difficult and thus the signal can't be trusted.

1648 The fits describe the data well. There is some fluctuation of the order of 10 %
 1649 around the fit function. At hight j_T the statistical errors in the signal are large.

1650 9.7.1 Results

1651 RMS and yield results with systematic errors are shown separately in figure 48.
 1652 Figure 49 shows RMS values for both components combined. The figure also
 1653 includes results from a PYTHIA simulation.

1654 9.8 Comparison to dihadron results

1655 Comparison to RMS values in dihadron analysis [?] are shown in figure Dihadron
 1656 results from [?]. For comparison the dihadron trigger p_T bins are converted to jet
 1657 p_T bins and vice versa. Bin-by-bin comparison is still not possible, but dihadron
 1658 analysis gives systematically larger RMS values. This could be caused by several
 1659 kinematical factors. In jet j_T analysis the jet cone limits possible j_T values and
 1660 thus the width and RMS of the j_T distributions. The effect of this limitation can
 1661 be studied by changing the cone size as is described in section 9.9.

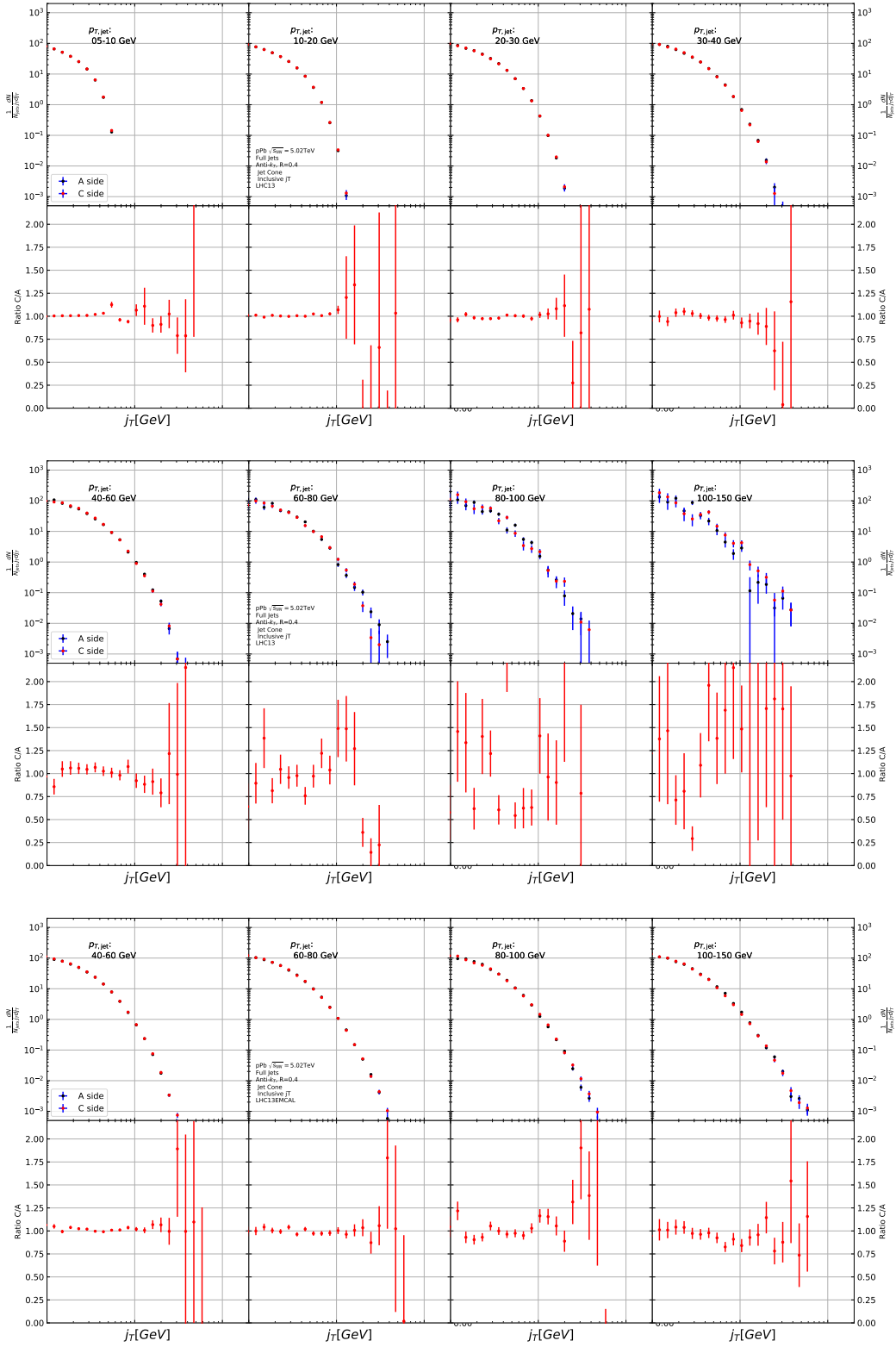


Figure 44: Comparison of inclusive j_{T8} distributions between A and C side for minimum bias and EMCAL triggered data.

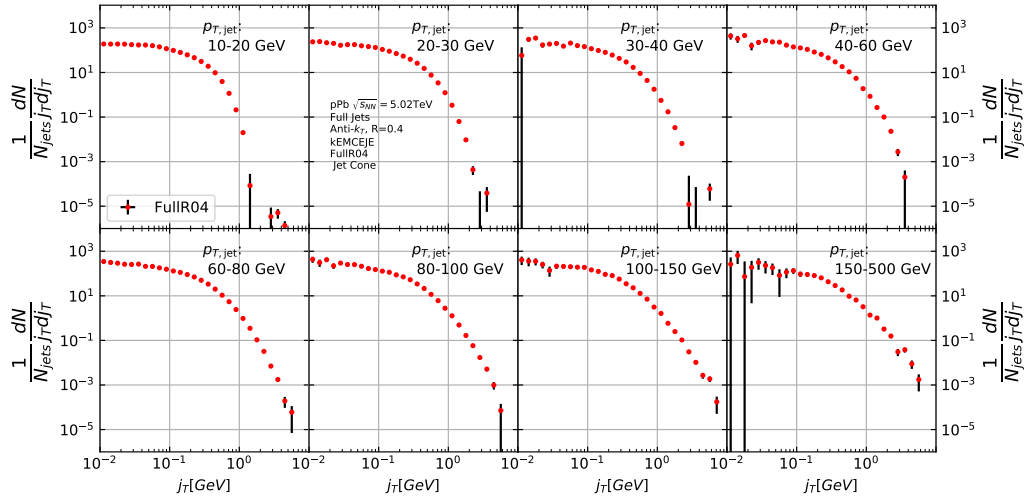


Figure 45: j_T signal with background subtracted

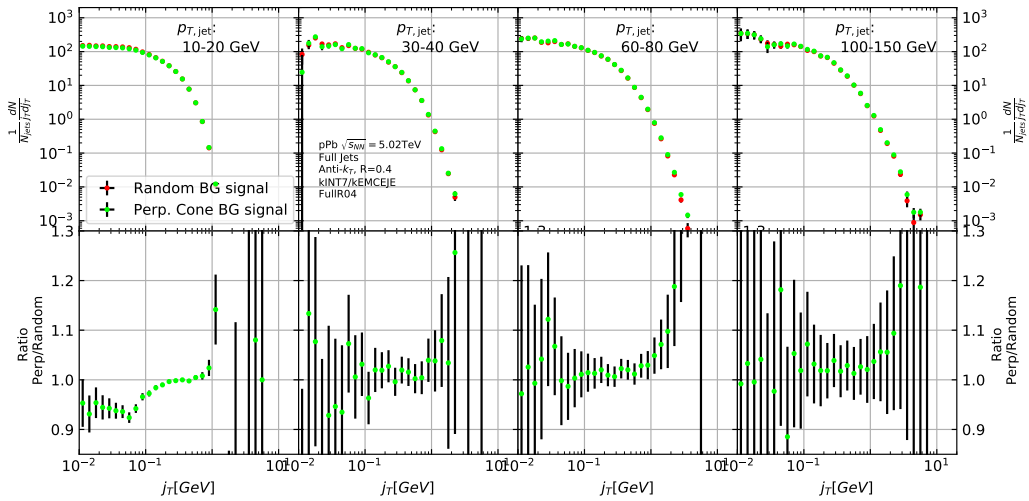


Figure 46: Comparison of the effect of background method on j_T signal.

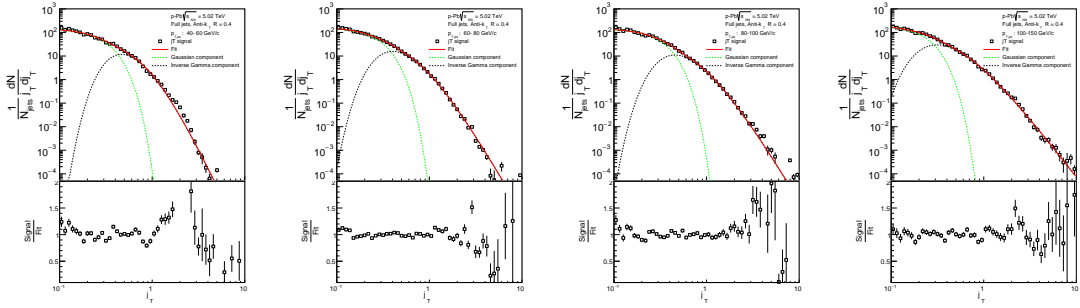


Figure 47: j_T signal fits in different jet p_T bins

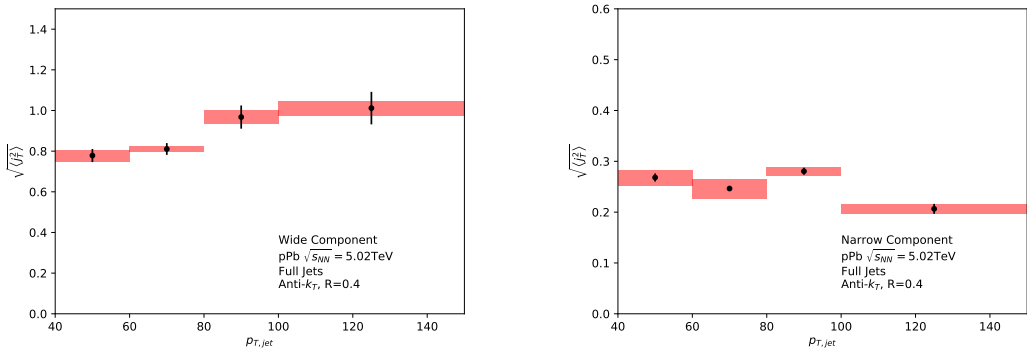


Figure 48: RMS values extracted from the fits for the gaussian (narrow) and inverse gamma (wide) components

1662 Comparison to j_T results from dihadron analysis [?] is shown in figure 55.
 1663 Trigger p_T bins used in dihadron analysis are converted to jet p_T bins using ob-
 1664 served average jet p_T values in leading track momentum bins. Similarly jet p_T bins
 1665 are converted to $p_{T,trigger}$ bins using average leading track p_T values in $p_{T,jet}$ bins.

1666 The trends are similar in dihadron and jet j_T results. Wide component RMS
 1667 values tend to increase with increasing $p_{T,trigger}/p_{T,jet}$. Narrow component RMS
 1668 increases slightly in dihadron analysis but not in jet j_T , WHY? (Depends on $x_{||}$
 1669 bin in dihadron)

1670 In general dihadron j_T gives wider distributions with larger RMS values. In
 1671 jet analysis the cone size limits width and thus the RMS values. The effect of this
 1672 limitation can be studied by changing the cone size as is described in section 9.9.

1673 Additionally the leading track is an imperfect estimate of the jet/original par-
 1674 ton. Because the leading track in general is at an angle compared to the jet axis,
 1675 the resulting j_T values are different. In practice the jet axis found by the jet finding
 1676 algorithm tends to minimize the average j_T of jet constituents. Thus the yield at

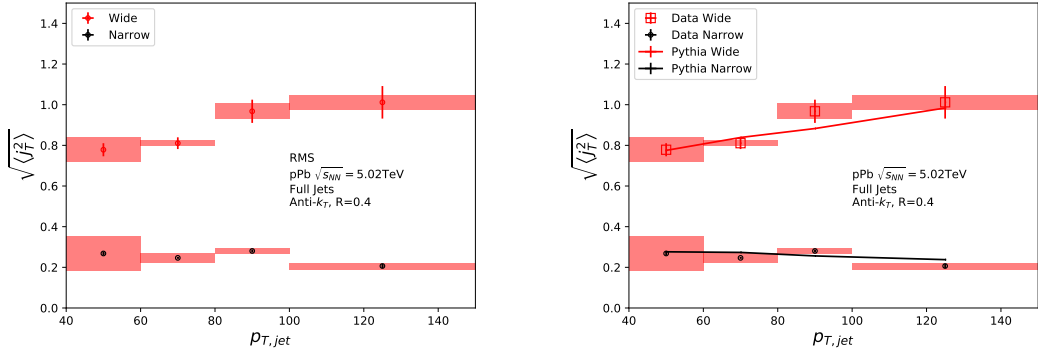


Figure 49: RMS values extracted from the fits for the gaussian (narrow) and inverse gamma (wide) components

¹⁶⁷⁷ high j_T is limited and the RMS values are smaller.

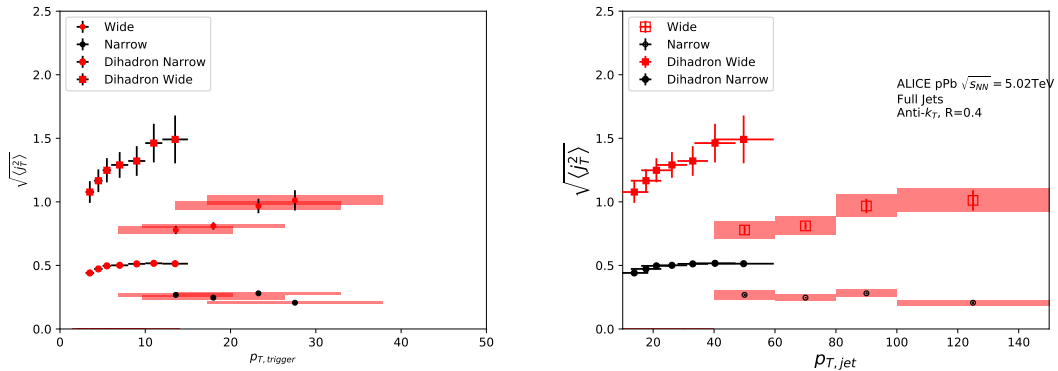


Figure 50: Jet j_T results are compared to results obtained in the dihadron analysis. This is done both in jet p_T and trigger p_T bins by converting between them.

¹⁶⁷⁸ 9.9 Different R parameters

¹⁶⁷⁹ Study the effect of cone sizes on j_T distribution in particle level Pythia.

¹⁶⁸⁰ Increasing the cone size of jets gives more room for high j_T tracks. This is seen
¹⁶⁸¹ in the individual j_T distributions as increased high j_T production. At low j_T there
¹⁶⁸² is no change.

¹⁶⁸³ When looking at RMS values from wide component we see an increase/decrease
¹⁶⁸⁴ of about 10% when going from $R = 0.4$ to $R = 0.5/R = 0.3$.

1685 The message from narrow component RMS values is less clear. At low jet p_T
 the behaviour is similar, but at high p_T the order is reversed.

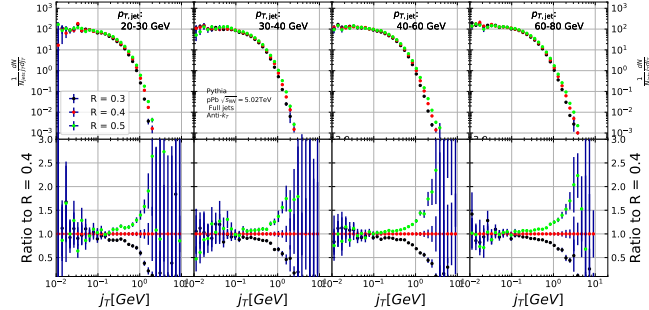


Figure 51: Effect of changing R parameter in jet finding on j_T distributions

1686

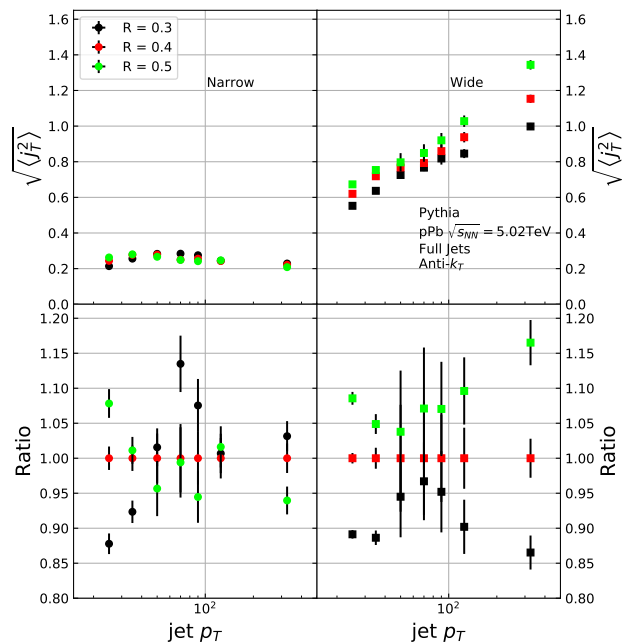


Figure 52: Effect of changing R parameter in jet finding on narrow and wide component RMS values. Wide component RMS values increase with increasing cone size.

1687 10 Discussion

1688 10.1 Discussion

1689 10.1.1 Dihadron j_T

1690 The jet fragmentation transverse momentum j_T has been studied previously at
 1691 ALICE with dihadron correlations [2]. The study took the leading hadron in
 1692 each event and calculated j_T for any near-side tracks with respect to the leading
 1693 hadron. Thus there is no kinematical limit to j_T from the jet cone. In the analysis
 1694 the background shape is estimated using pairs with large $\Delta\eta$. The normalisation of
 1695 the background is done when fitting the j_T distribution. The inclusive and signal
 1696 distributions from the analysis are shown in Fig. 53. The inclusive distribution is
 1697 fitted with a three component function,

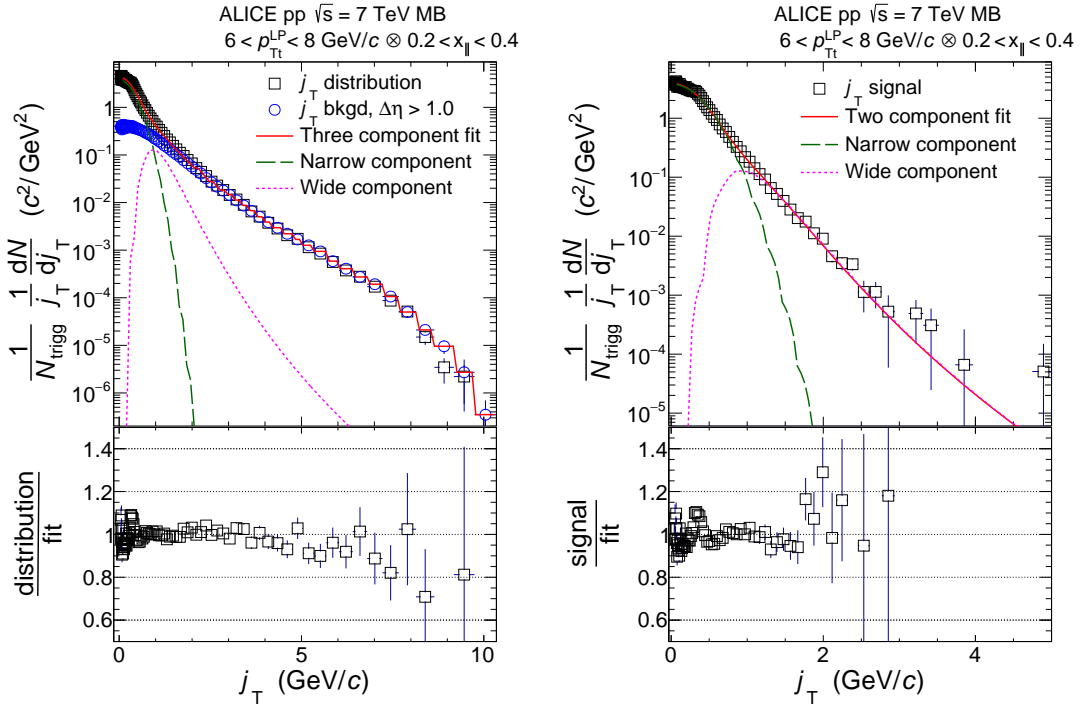


Figure 53: *Left:* Measured j_T distribution including a three-component fit. The three components describe the background (circular symbols), hadronization (long dashed line), and showering (short dashed line). *Right:* The same j_T distribution but with background subtracted.

1698 The analysis was the first to introduce this factorisation of j_T into components.
 1699 At $j_T \approx 0.4 \text{ GeV}$ there is a small bump in the distribution to fit ratio. This
 1700 was attributed to cases where the trigger particle decayed after hadronisation. As

it is difficult to correct for, this bump is included in the systematic errors of the results.

The RMS results from the fitting in both pp and p-Pb collisions are shown in Fig. 54. Qualitatively the results are similar to jet j_T results. The RMS value of the wide component has an increasing trend with respect to p_{Tt}/p_{Tjet} , while the RMS value of the narrow component stays constant. Both components are well described by PYTHIA simulations.

In the dihadron analysis there is no difference between pp and p-Pb results.

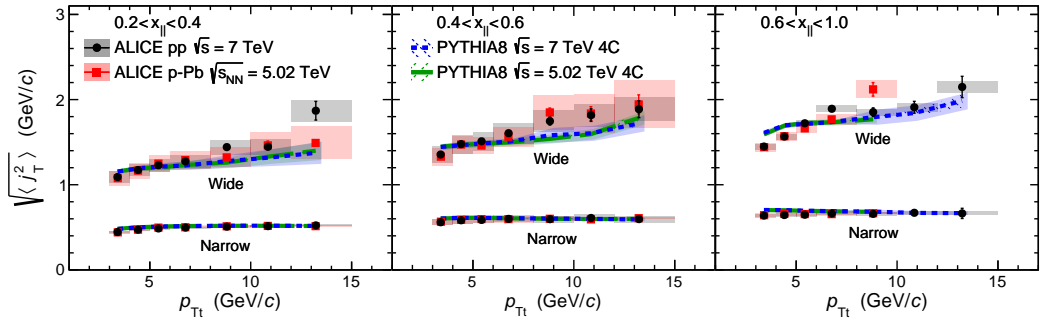


Figure 54: RMS values of the narrow and wide j_T components in the dihadron correlation analysis. Results from pp collisions at $\sqrt{s} = 7$ TeV (circular symbols) and from p-Pb collisions at $\sqrt{s_{NN}} = 5.02$ TeV (square symbols) are compared to PYTHIA 8 tune 4C simulations at $\sqrt{s} = 7$ TeV (short dashed line) and at $\sqrt{s} = 5.02$ TeV (long dashed line). Different panels correspond to different x_{\parallel} bins with $0.2 < x_{\parallel} < 0.4$ on the left, $0.4 < x_{\parallel} < 0.6$ in the middle, and $0.6 < x_{\parallel} < 1.0$ on the right. The statistical errors are represented by bars and the systematic errors by boxes. [2]

Comparison between jet and dihadron j_T results shown in Fig. 55. Trigger p_T bins used in dihadron analysis are converted to jet p_T bins using observed average jet p_T values in leading track momentum bins. Similarly jet p_T bins are converted to $p_{T\text{trigger}}$ bins using average leading track p_T values in $p_{T\text{jet}}$ bins.

In general dihadron j_T gives wider distributions with larger RMS values. There are several factors that could explain this. In jet analysis the cone size limits width and thus the RMS values. With increasing cone size one gets increasing wide RMS values as seen in Fig. 56. This should be the dominant factor.

Effect of the R parameter choice is studied in PYTHIA. Having a fixed cone puts hard limits on the possible j_T values. Increasing the cone size loosens these limits and allows higher j_T values. The results are shown in Fig. 56. Left hand side shows the j_T distributions. There is very little change in low j_T but at high j_T the yield increases.

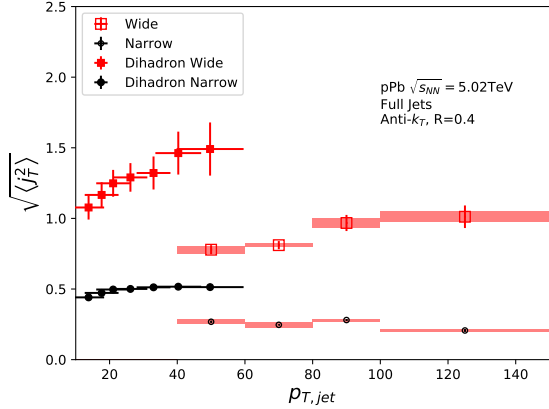


Figure 55: Comparison of results with dihadron j_T results. Dihadron trigger p_T bins are converted to jet p_T bins using observed mean $p_{T,jet}$ values in $p_{T,\text{trigger}}$ bins. Dihadron results are for $0.2 < x_{||} < 0.4$

This is also seen in the RMS values shown in the right hand side of Fig. 56, where the change in wide component RMS is about 10% when going from $R = 0.4$ to $R = 0.3$ or $R = 0.5$. With the narrow component values the situation is less clear. At low jet p_T larger R parameter leads to larger RMS values, but at high $p_{T,jet}$ the situation is reversed; increasing the R parameter decreases RMS values.

Additionally the leading track is an imperfect estimate of the jet/original parton. Because the leading track in general is at an angle compared to the jet axis, the resulting j_T values are different. In practice the jet axis found by the jet finding algorithm tends to minimize the average j_T of jet constituents. Thus the yield at high j_T is limited and the RMS values are smaller.

A PYTHIA study was performed where j_T was calculated with respect to the leading track momentum, instead of the jet axis. The results are shown in Fig. 57. The resulting j_T distributions are significantly wider than j_T distributions from the typical method. The effect seems to be larger than the effect seen in comparing different R values.

Lastly the results from the dihadron analysis are done in $p_{T,\text{trigger}}$ bins. This favours hard jets, i.e. jets where the leading hadron carries a large momentum fraction and the jet multiplicity is small. In $p_{T,jet}$ bins jets are more likely to be soft, i.e. small leading momentum fraction and high multiplicity jets.

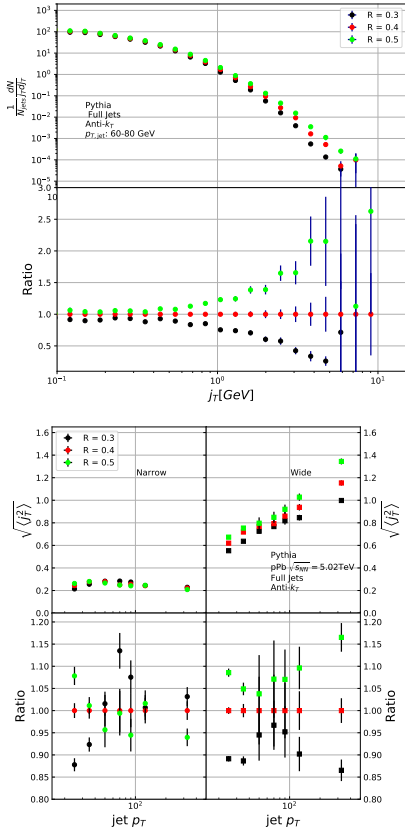


Figure 56: Effect of changing R parameter in jet finding on j_T distributions

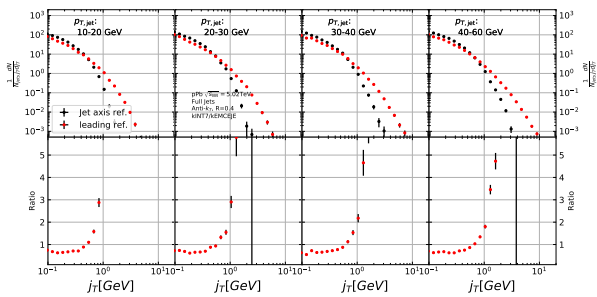


Figure 57: Results of calculating j_T with respect to the jet axis or the leading hadron. The assumption is that because the leading hadron is an imperfect estimate of the jet axis, low j_T tracks should on average be shifted to higher j_T

1741 11 Summary

1742 In this work two distinct j_T components were extracted for narrow and wide contri-
1743 butions using jet reconstruction. RMS values for both components were obtained.
1744 The width of the wide component is found to increase for increasing $p_{T\text{jet}}$. This
1745 is in part explained by the changing kinematical limits when going to higher $p_{T\text{jet}}$
1746 which allows higher $p_{T\text{track}}$. Additionally the larger phase space allows stronger
1747 parton splitting. The results are qualitatively compatible with previous studies
1748 that studied j_T using two-particle correlations.

¹⁷⁴⁹ References

- ¹⁷⁵⁰ [1] ALICE, J. Adam *et al.*, Phys. Rev. **C91**, 064905 (2015), 1412.6828.
- ¹⁷⁵¹ [2] <https://alice-publications.web.cern.ch/node/3655>, 2018.
- ¹⁷⁵² [3] PHENIX Collaboration, K. Adcox *et al.*, Nucl.Phys. **A757**, 184 (2005), nucl-ex/0410003.
- ¹⁷⁵⁴ [4] STAR Collaboration, J. Adams *et al.*, Nucl.Phys. **A757**, 102 (2005), nucl-ex/0501009.
- ¹⁷⁵⁵
- ¹⁷⁵⁶ [5] J.-Y. Ollitrault, Phys. Rev. D **46**, 229 (1992).
- ¹⁷⁵⁷ [6] U. Heinz and P. Kolb, Nucl. Phys. **A702**, 269 (2002).
- ¹⁷⁵⁸ [7] E. Shuryak, Prog. Part. Nucl. Phys. **62**, 48 (2009).
- ¹⁷⁵⁹ [8] ATLAS Collaboration, J. Jia, Nucl.Phys.A904-905 **2013**, 421c (2013), 1209.4232.
- ¹⁷⁶⁰
- ¹⁷⁶¹ [9] R. A. Lacey *et al.*, (2012), 1207.1886.
- ¹⁷⁶² [10] R. Bjorklund, W. Crandall, B. J. Moyer, and H. York, Phys. Review **77**, 213 (1950).
- ¹⁷⁶³
- ¹⁷⁶⁴ [11] W. Heisenberg, Zeitschrift für Physik **77**, 1 (1932).
- ¹⁷⁶⁵ [12] M. Gell-Mann, Phys. Rev. **125**, 1067 (1962).
- ¹⁷⁶⁶ [13] M. Gell-Mann, Phys. Lett. **8**, 214 (1964).
- ¹⁷⁶⁷ [14] O. Greenberg, Phys. Rev. Lett. **13**, 598 (1964).
- ¹⁷⁶⁸ [15] Crystal Ball Collaboration, D. Williams *et al.*, Phys.Rev. **D38**, 1365 (1988).
- ¹⁷⁶⁹ [16] W. Krolikowski, Nuovo Cim. **A27**, 194 (1975).
- ¹⁷⁷⁰ [17] D. J. Gross and F. Wilczek, Physical Review Letters **30**, 1343 (1973).
- ¹⁷⁷¹ [18] H. D. Politzer, Physical Review Letters **30**, 1346 (1973).
- ¹⁷⁷² [19] D. J. Gross and F. Wilczek, Physical Review D **8**, 3633 (1973).
- ¹⁷⁷³ [20] D. J. Gross and F. Wilczek, Physical Review D **9**, 980 (1974).
- ¹⁷⁷⁴ [21] H. Georgi and H. D. Politzer, Physical Review D **9**, 416 (1974).

- ₁₇₇₅ [22] H. Fritzsch, M. Gell-Mann, and H. Leutwyler, Physics Letters B **47**, 365
₁₇₇₆ (1973).
- ₁₇₇₇ [23] I. Flegel and P. Söding, CERN courier (2004).
- ₁₇₇₈ [24] R. Brandelik *et al.*, Physics Letters B **86**, 243 (1979).
- ₁₇₇₉ [25] J. K. L. MacDonald, Phys. Rev. **43**, 830 (1933).
- ₁₇₈₀ [26] C. Berger *et al.*, Physics Letters B **86**, 418 (1979).
- ₁₇₈₁ [27] J. Collins and M. Perry, Phys. rev. Lett. **34**, 1353 (1975).
- ₁₇₈₂ [28] E. Shuryak, Phys. Reps. **61**, 71 (1980).
- ₁₇₈₃ [29] K. Rajagopal, SLAC Beam Line **31-2**, 9 (2001).
- ₁₇₈₄ [30] P. Kovtun, D. Son, and A. Starinets, Phys.Rev.Lett. **94**, 111601 (2005),
₁₇₈₅ hep-th/0405231.
- ₁₇₈₆ [31] R. A. Lacey *et al.*, Phys. Rev. Lett. **98**, 092301 (2007).
- ₁₇₈₇ [32] E. Lofgren, *ACCELERATOR DIVISION ANNUAL REPORTS, 1 JULY*
₁₇₈₈ *1972 12/31/1974* (, 1975).
- ₁₇₈₉ [33] D. S. Barton, Heavy ion program at bnl: Ags, rhic, in *Proc. 1987 Particle*
₁₇₉₀ *Accelerator Conference, Washington, D.C., March, 1987*, 1987.
- ₁₇₉₁ [34] I. Vitev and M. Gyulassy, Phys.Rev.Lett. **89**, 252301 (2002), hep-
₁₇₉₂ ph/0209161.
- ₁₇₉₃ [35] S. Choi and K. S. Lee, Phys. Rev. C **84**, 064905 (2011).
- ₁₇₉₄ [36] A. Kovalenko *et al.*, Status of the nuclotron, in *Proceedings of EPAC Vol. 94*,
₁₇₉₅ pp. 161–164, 1994.
- ₁₇₉₆ [37] NA61/SHINE, K. Grebieszkow, PoS **CPOD2013**, 004 (2013).
- ₁₇₉₇ [38] BRAHMS Collaboration, I. Arsene *et al.*, Nucl.Phys. **A757**, 1 (2005), nucl-
₁₇₉₈ ex/0410020.
- ₁₇₉₉ [39] B. Back *et al.*, Nucl.Phys. **A757**, 28 (2005), nucl-ex/0410022.
- ₁₈₀₀ [40] S. A. Voloshin, A. M. Poskanzer, and R. Snellings, (2008), 0809.2949.
- ₁₈₀₁ [41] S. A. Voloshin, A. M. Poskanzer, A. Tang, and G. Wang, Phys.Lett. **B659**,
₁₈₀₂ 537 (2008), 0708.0800.

- ₁₈₀₃ [42] H. Holopainen, H. Niemi, and K. J. Eskola, Phys.Rev. **C83**, 034901 (2011), 1007.0368.
- ₁₈₀₄
- ₁₈₀₅ [43] ALICE Collaboration, Phys. Rev. C **88**, 044909 (2013).
- ₁₈₀₆ [44] M. L. Miller, K. Reygers, S. J. Sanders, and P. Steinberg, Ann.Rev.Nucl.Part.Sci. **57**, 205 (2007), nucl-ex/0701025.
- ₁₈₀₇
- ₁₈₀₈ [45] R. Glauber, Lectures in theoretical physics, 1959.
- ₁₈₀₉ [46] W. Czyż and L. Maximon, Annals of Physics **52**, 59 (1969).
- ₁₈₁₀ [47] A. Białas, M. Bleszyński, and W. Czyż, Nuclear Physics B **111**, 461 (1976).
- ₁₈₁₁ [48] PHENIX Collaboration, S. Afanasiev *et al.*, Phys.Rev. **C80**, 054907 (2009), 0903.4886.
- ₁₈₁₂
- ₁₈₁₃ [49] J.-Y. Ollitrault, Eur.J.Phys. **29**, 275 (2008), 0708.2433.
- ₁₈₁₄ [50] P. Romatschke, Int.J.Mod.Phys. **E19**, 1 (2010), 0902.3663.
- ₁₈₁₅ [51] L. LD, Izv. Akad. Nauk Ser. Fiz. **17**, 51 (1953).
- ₁₈₁₆ [52] H. Song, S. Bass, and U. W. Heinz, (2013), 1311.0157.
- ₁₈₁₇ [53] H. Niemi, G. Denicol, P. Huovinen, E. Molnar, and D. Rischke, Phys.Rev. **C86**, 014909 (2012), 1203.2452.
- ₁₈₁₈
- ₁₈₁₉ [54] K. A. *et al.* [ALICE Collaboration], Phys. Rev. Lett **106** (2011), 032301.
- ₁₈₂₀ [55] J.-Y. Ollitrault, Phys.Rev. D **48**, 1132 (1993), hep-ph/9303247.
- ₁₈₂₁ [56] P. Danielewicz and G. Odyniec, Physics Letters B **157**, 146 (1985).
- ₁₈₂₂ [57] P. Danielewicz and M. Gyulassy, Physics Letters B **129**, 283 (1983).
- ₁₈₂₃ [58] T. Abbott *et al.*, Phys. Rev. Lett. **70**, 1393 (1993).
- ₁₈₂₄ [59] S. Voloshin and Y. Zhang, Z.Phys. **C70**, 665 (1996), hep-ph/9407282.
- ₁₈₂₅ [60] E877 Collaboration, J. Barrette *et al.*, Phys.Rev.Lett. **73**, 2532 (1994), hep-ex/9405003.
- ₁₈₂₆
- ₁₈₂₇ [61] CMS Collaboration, S. Chatrchyan *et al.*, Phys.Rev.Lett. **109**, 022301 (2012), 1204.1850.
- ₁₈₂₈

- ₁₈₂₉ [62] Y. I. Azimov, Y. L. Dokshitzer, V. A. Khoze, and S. I. Trovan, Zeitschrift
₁₈₃₀ für Physik C Particles and Fields **27**, 65 (1985).
- ₁₈₃₁ [63] B. Andersson, G. Gustafson, G. Ingelman, and T. Sjöstrand, Physics Reports
₁₈₃₂ **97**, 31 (1983).
- ₁₈₃₃ [64] A. Buckley *et al.*, Phys. Rept. **504**, 145 (2011), 1101.2599.
- ₁₈₃₄ [65] M. Bahr *et al.*, Eur. Phys. J. **C58**, 639 (2008), 0803.0883.
- ₁₈₃₅ [66] A. Kurkela and U. A. Wiedemann, Phys. Lett. **B740**, 172 (2015), 1407.0293.
- ₁₈₃₆ [67] R. Baier, Y. L. Dokshitzer, A. H. Mueller, S. Peigne, and D. Schiff, Nucl.
₁₈₃₇ Phys. **B484**, 265 (1997), hep-ph/9608322.
- ₁₈₃₈ [68] W. H. H. Bethe and, Proc.Roy.Soc.Lond. **A146** (1934).
- ₁₈₃₉ [69] L. D. Landau and I. Pomeranchuk, Dokl. Akad. Nauk Ser. Fiz. **92**, 535
₁₈₄₀ (1953).
- ₁₈₄₁ [70] A. B. Migdal, Phys. Rev. **103**, 1811 (1956).
- ₁₈₄₂ [71] P. Bosted *et al.*, Quantum-mechanical suppression of bremsstrahlung*, 1993.
- ₁₈₄₃ [72] A. Majumder and M. Van Leeuwen, Prog.Part.Nucl.Phys. **A66**, 41 (2011),
₁₈₄₄ 1002.2206.
- ₁₈₄₅ [73] F. Dominguez, C. Marquet, A. Mueller, B. Wu, and B.-W. Xiao, Nucl.Phys.
₁₈₄₆ **A811**, 197 (2008), 0803.3234.
- ₁₈₄₇ [74] M. Gyulassy, P. Levai, and I. Vitev, Nucl.Phys. **B571**, 197 (2000), hep-
₁₈₄₈ ph/9907461.
- ₁₈₄₉ [75] U. A. Wiedemann, Nucl.Phys. **B588**, 303 (2000), hep-ph/0005129.
- ₁₈₅₀ [76] P. B. Arnold, G. D. Moore, and L. G. Yaffe, JHEP **0112**, 009 (2001), hep-
₁₈₅₁ ph/0111107.
- ₁₈₅₂ [77] X.-N. Wang and X.-f. Guo, Nucl.Phys. **A696**, 788 (2001), hep-ph/0102230.
- ₁₈₅₃ [78] T. Sjostrand, S. Mrenna, and P. Z. Skands, Comput.Phys.Commun. **178**,
₁₈₅₄ 852 (2008), 0710.3820.
- ₁₈₅₅ [79] I. Lokhtin and A. Snigirev, Eur.Phys.J. **C45**, 211 (2006), hep-ph/0506189.
- ₁₈₅₆ [80] N. Armesto, L. Cunqueiro, and C. A. Salgado, Nucl.Phys. **A830**, 271C
₁₈₅₇ (2009), 0907.4706.

- 1858 [81] K. Zapp, G. Ingelman, J. Rathsman, J. Stachel, and U. A. Wiedemann,
1859 Eur.Phys.J. **C60**, 617 (2009), 0804.3568.
- 1860 [82] T. Renk, Phys.Rev. **C79**, 054906 (2009), 0901.2818.
- 1861 [83] ALICE Collaboration, K. Aamodt *et al.*, Phys.Lett. **B696**, 30 (2011),
1862 1012.1004.
- 1863 [84] WA98 Collaboration, M. Aggarwal *et al.*, Eur.Phys.J. **C23**, 225 (2002),
1864 nucl-ex/0108006.
- 1865 [85] D. G. d'Enterria, Phys.Lett. **B596**, 32 (2004), nucl-ex/0403055.
- 1866 [86] PHENIX Collaboration, A. Adare *et al.*, Phys.Rev.Lett. **101**, 232301 (2008),
1867 0801.4020.
- 1868 [87] STAR Collaboration, J. Adams *et al.*, Phys.Rev.Lett. **91**, 172302 (2003),
1869 nucl-ex/0305015.
- 1870 [88] A. Dainese, C. Loizides, and G. Paic, Eur.Phys.J. **C38**, 461 (2005), hep-
1871 ph/0406201.
- 1872 [89] I. Vitev, J.Phys. **G30**, S791 (2004), hep-ph/0403089.
- 1873 [90] C. A. Salgado and U. A. Wiedemann, Phys.Rev. **D68**, 014008 (2003), hep-
1874 ph/0302184.
- 1875 [91] N. Armesto, A. Dainese, C. A. Salgado, and U. A. Wiedemann, Phys.Rev.
1876 **D71**, 054027 (2005), hep-ph/0501225.
- 1877 [92] T. Renk, H. Holopainen, R. Paatelainen, and K. J. Eskola, Phys.Rev. **C84**,
1878 014906 (2011), 1103.5308.
- 1879 [93] CMS Collaboration, S. Chatrchyan *et al.*, Eur.Phys.J. **C72**, 1945 (2012),
1880 1202.2554.
- 1881 [94] PHENIX Collaboration, S. Afanasiev *et al.*, Phys. Rev. C **80**, 054907 (2009).
- 1882 [95] ALICE Collaboration, K. Aamodt *et al.*, Phys.Rev.Lett. **108**, 092301 (2012),
1883 1110.0121.
- 1884 [96] J. L. Nagle and W. A. Zajc, Ann. Rev. Nucl. Part. Sci. **68**, 211 (2018),
1885 1801.03477.
- 1886 [97] E735, T. Alexopoulos *et al.*, Phys. Rev. **D48**, 984 (1993).

- ₁₈₈₇ [98] MiniMax, T. C. Brooks *et al.*, Phys. Rev. **D61**, 032003 (2000), hep-ex/9906026.
- ₁₈₈₉ [99] C. Shen, Z. Qiu, and U. Heinz, Phys. Rev. **C92**, 014901 (2015), 1502.04636.
- ₁₈₉₀ [100] PHENIX, A. Adare *et al.*, Phys. Rev. **C94**, 064901 (2016), 1509.07758.
- ₁₈₉₁ [101] C. A. Salgado and J. P. Wessels, Ann. Rev. Nucl. Part. Sci. **66**, 449 (2016).
- ₁₈₉₂ [102] M. Gyulassy, I. Vitev, X.-N. Wang, and B.-W. Zhang, p. 123 (2003), nucl-th/0302077.
- ₁₈₉₄ [103] E. Norbeck, K. Šafařík, and P. A. Steinberg, Annual Review of Nuclear and Particle Science **64**, 383 (2014), <https://doi.org/10.1146/annurev-nucl-102912-144532>.
- ₁₈₉₇ [104] A. Accardi, F. Arleo, W. K. Brooks, D. D'Enterria, and V. Muccifora, Riv. Nuovo Cim. **32**, 439 (2010), 0907.3534.
- ₁₈₉₉ [105] ALICE, K. Aamodt *et al.*, JINST **3**, S08002 (2008).
- ₁₉₀₀ [106] ALICE, B. B. Abelev *et al.*, Int. J. Mod. Phys. **A29**, 1430044 (2014), 1402.4476.
- ₁₉₀₂ [107] ALICE, K. Aamodt *et al.*, JINST **5**, P03003 (2010), 1001.0502.
- ₁₉₀₃ [108] J. Alme *et al.*, Nucl. Instrum. Meth. **A622**, 316 (2010), 1001.1950.
- ₁₉₀₄ [109] ALICE, B. Abelev *et al.*, JHEP **03**, 053 (2012), 1201.2423.
- ₁₉₀₅ [110] ALICE, P. Cortese *et al.*, (2008).
- ₁₉₀₆ [111] J. Allen *et al.*, Report No. CERN-LHCC-2010-011. ALICE-TDR-14-add-1, 2010 (unpublished).
- ₁₉₀₈ [112] ALICE, G. Dellacasa *et al.*, (1999).
- ₁₉₀₉ [113] ALICE Collaboration, *Technical Design Report on Forward Detectors: FMD, T0 and V0*, 2004.
- ₁₉₁₁ [114] ALICE, B. Abelev *et al.*, Phys. Lett. **B719**, 29 (2013), 1212.2001.
- ₁₉₁₂ [115] 2019.
- ₁₉₁₃ [116] T. ALICE Collaboration *et al.*, Journal of Instrumentation **3**, S08002 (2008).

- ₁₉₁₄ [117] for the ALICE, C. Zampolli, Particle Identification with the ALICE detector at the LHC, in *Proceedings, PLHC2012: Physics at the LHC 2012 (PLHC2012): Vancouver, BC, Canada, June 4-9, 2012*, 2012, 1209.5637.
- ₁₉₁₇ [118] M. Cacciari, G. P. Salam, and G. Soyez, Eur. Phys. J. **C72**, 1896 (2012), 1111.6097.
- ₁₉₁₉ [119] M. Cacciari, G. P. Salam, and G. Soyez, JHEP **04**, 063 (2008), 0802.1189.
- ₁₉₂₀ [120] T. Sjöstrand, S. Mrenna, and P. Z. Skands, Comput. Phys. Commun. **178**, 852 (2008), 0710.3820.
- ₁₉₂₂ [121] Roounfold: Root unfolding framework, <http://hepunx.rl.ac.uk/~adye/software/unfold/RooUnfold.html>, 2013.
- ₁₉₂₃